Well-defined metal nanostructures as platform for chemical characterization and catalytic applications

by

Marimuthu Andiappan

A dissertation submitted in partial fulfillment
of the requirements for the degree of
Doctor of Philosophy
(Chemical Engineering)
in the University of Michigan
2013

Doctoral Committee:

Associate Professor Suljo Linic, Chair
Associate Professor Jinsang Kim
Professor Phillip E. Savage
Professor Johannes W. Schwank

DEDICATION

This dissertation is dedicated to my parents Lakshmi and Andiappan, my brother Balamurugan, my friends and family members for their boundless love and support.

ACKNOWLEDGEMENTS

Many people have contributed to this dissertation in various ways. I would like to thank my advisor Prof. Suljo Linic for his guidance and support throughout my PhD. Prof. Linic`s dedication to do novel research was a great motivation for me. I would like to thank him especially for the opportunity he gave me to solve some challenging problems to understand the mechanism in the field of surface plasmon mediated photochemistry. I am very grateful to other members of my doctoral committee, Prof. Jinsang Kim, Prof. Phillip Savage and Prof. Johannes Schwank for their insights and suggestions during my committee meetings. I would also like to thank them for their valuable comments during the revision of this dissertation.

I would like to thank all of the members of Linic Research Group- Siris Laursen, Hongliang Xin, Neil Schweitzer, David Ingram, Phillip Christopher, Adam Holewinski, Katrina Ramsdell, Mathew Morabito, Michelle Przybylek, Thomas Yeh, Jianwen Zhang, Tim Van Cleve, Paul Hernley, Brittany Lancaster, Anh Ta, Thomas Noel, Robert Campana and Calvin Boerigter for their support during my PhD. I have worked directly with Jianwen Zhang, Hongliang Xin, David Ingram and Phillip Christopher during my PhD. I am grateful for their support and many interesting discussions. I would like to thank my undergraduate students Eric and Eunah for

their help with synthesis and preparation of the catalysts. I also acknowledge the financial support from NSF and DOE for this work.

I would like to thank all of my friends and family members for their boundless love and support during my PhD. My mom Lakshmi and my brother Bala have always been very supportive. I would like to thank my friends- Mani, Gnanam, Arun (Varanasi), Rajesh, Murali, Arun (Padakandla), Indranil, Mahesh, Karthik, Changi, Nasim, Priyanka (Pande), Lilian, Sameer, Priyanka (Desai), Desh, Khamir, Mohammad, Hao, Aravind, Raghu, Shashi, Debasis and Mrinal for their support during my PhD.

TABLE OF CONTENTS

LIST OF FIGURES

ABSTRACT

Metal nanostructures with controlled sizes and shapes possess interesting optical, electronic and catalytic properties, making them suitable for a wide range of applications. The objectives of this dissertation were to 1) exploit the optical properties of the metal nanostructures to achieve selective molecular sensing using surface enhanced Raman spectroscopy (SERS) and high selectivity towards the desired product in heterogeneous catalysis, and 2) improve the stability of the metal nanostructures of controlled shape under catalytic reaction conditions.

The optical properties of silver (Ag) nanostructures can be controlled by changing their shape. We have demonstrated that this effect can be employed to control the degree to which the Ag nanostructures enhance different vibrational bands of a molecule in SERS. We have shown that Ag nanocube and Ag nanosphere substrates with surface plasmon resonance peaks near 600 and 560 nm could be used to selectively detect species with 2100-2200 cm^{-1} and 900–1000 cm^{-1} Raman vibrational bands, respectively. This approach gives new insights in the design of plasmonic substrates for the selective molecular species detection.

We have also demonstrated that the optical properties of copper (Cu) nanoparticles can be exploited under propylene oxidation conditions to favor the

formation of the desired product, propylene oxide. We find that Cu nanocatalysts exhibit a sharp increase in selectivity to propylene oxide from ~20% to ~50% when illuminated with visible light. This increase in the selectivity is accompanied by light-induced change in the oxidation state of the surface Cu atoms from Cu-oxide (light off) to Cu metal (light on). This design principle gives new insights to control the reaction rate and product selectivity in heterogeneous catalysis.

Finally, we have demonstrated a pretreatment method to improve the stability of metal nanostructures of controlled shape under catalytic reaction conditions. Ag nanocube catalysts pretreated at high temperature (400 °C) in oxygen atmosphere to remove the polymeric capping agent (polyvinylpyrrolidone) exhibit ~20% loss in activity under ethylene oxidation at 230 °C during the reaction time of 20 hours. However, we demonstrate that Ag nanocube catalysts pretreated with polysulfide solution at room temperature can exhibit stable activity for similar reaction conditions.

CHAPTER 1

Introduction

1.1. Summary

This chapter presents a brief introduction to metal nanostructures of controlled sizes and shapes, and their unique optical properties. This introduction describes surface plasmon (SP) phenomena, and SP mediated effects in plasmonic metal nanostructures that can be exploited for chemical characterization and catalytic applications are detailed. The unique electronic and catalytic properties of metal nanostructures of controlled shapes are also discussed. Detailed descriptions of the important spectroscopic and theoretical techniques utilized in this work are also provided. The scope of this thesis and the general structure of the remainder of the thesis are detailed.

1.2. Well-defined metal nanostructures[1–11]

Metal nanoparticles often exhibit unique electronic and optical properties that are strikingly different from those of their bulk material counterparts. For example, chemically inert bulk gold (Au) becomes a catalytic active material when deposited on supports at nanometer size;[12] optically opaque bulk copper (Cu) becomes transparent at nanoscale.[2] Interest in nanoparticles has greatly increased mainly

because of recent advances in synthetic chemistry to control the size and shape of nanoparticles. These well-defined metal nanostructures, i.e., metal nanoparticles with controlled sizes and shapes possess very interesting optical and electronic properties compared to bulk materials, making them suitable for a wide range of applications in the fields of spectroscopy (sensors), medicine (targeted drug delivery), nanoelectronics, energy storage and catalysis. In this thesis, the focus is on exploiting the optical and electronic properties of metal nanostructures for molecular sensing and catalytic applications.

1.2.1. Optical properties of metal nanostructures and surface plasmon (SP) [1–11]

When an electromagnetic radiation interacts with the metal nanoparticle, it can cause the collective (coherent) oscillations of the conduction electrons in the nanoparticle; these are commonly known as surface plasmons (SP). Figure 1.1 shows classical schematic representation of surface plasmon for the interaction between light and free electrons of spherical nanoparticles. In a classical description, the electric field of an incoming light wave induces a polarization of the (free) conduction electrons in the metal nanoparticle and causes the oscillation of the electrons against the restoring force of the background field of positively charged nuclei. When the frequency of the electrons oscillating against the restoring force of the nuclei matches with frequency of the incident radiation, the interference is constructive with the strongest interaction between metal nanoparticle and the electromagnetic radiation and this system is said to be in resonance. The frequency corresponds to resonance condition is known as surface plasmon resonance (SPR)

frequency. The surface plasmon resonance frequency depends on the dielectric constant of the metal, size and shape of the metal nanoparticle, and the medium surrounding it (see Figures 1.2.a and 1.2.b.). Among metals, the free electron densities of the noble metals (copper, silver and gold) are in the range such that their plasmon resonance frequencies are in the visible light range (see Figure 1.3.a).

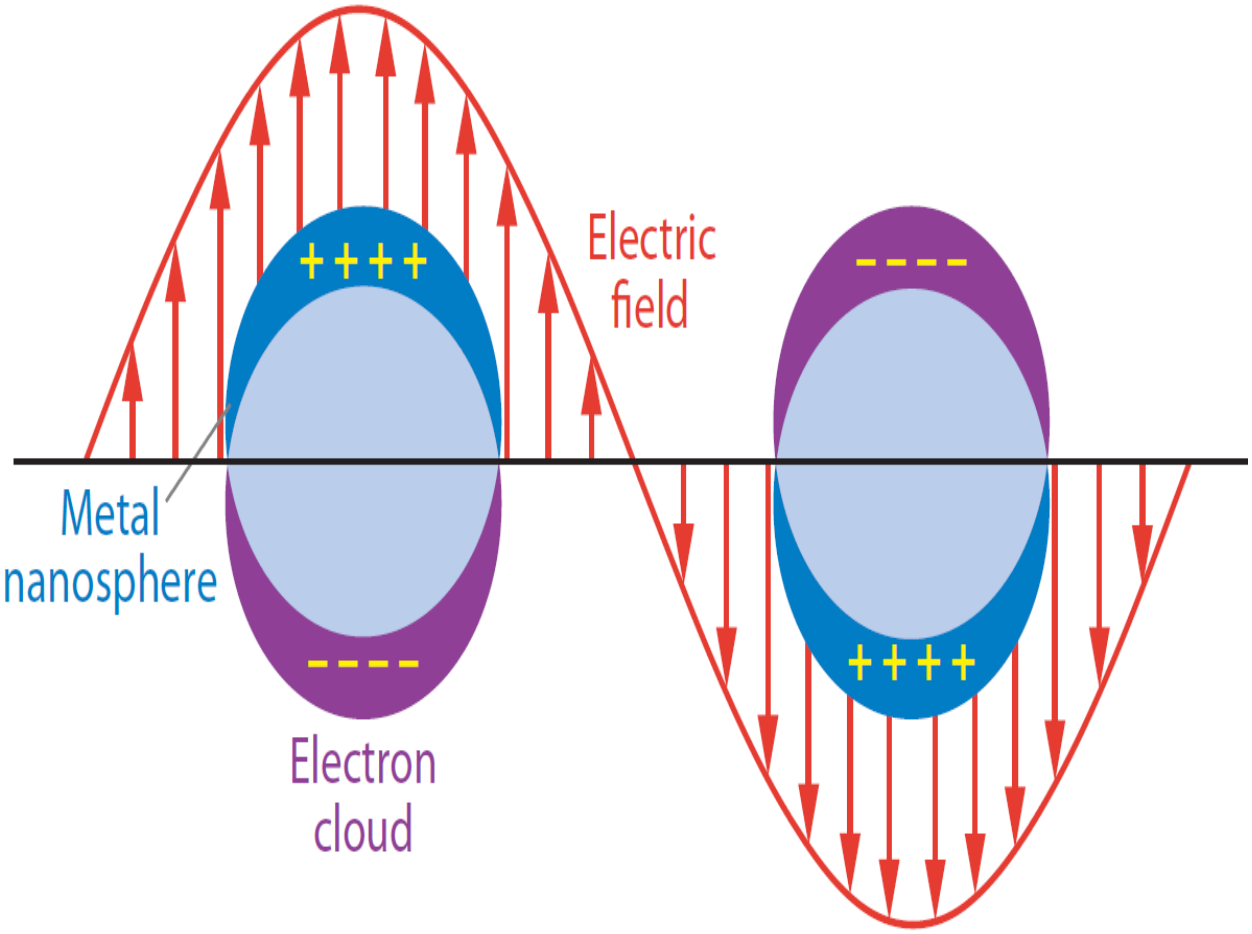

Figure 1.1. Schematic illustrating the classical representation of surface plasmon in spherical nanoparticles. Taken from Lu et al.[10]

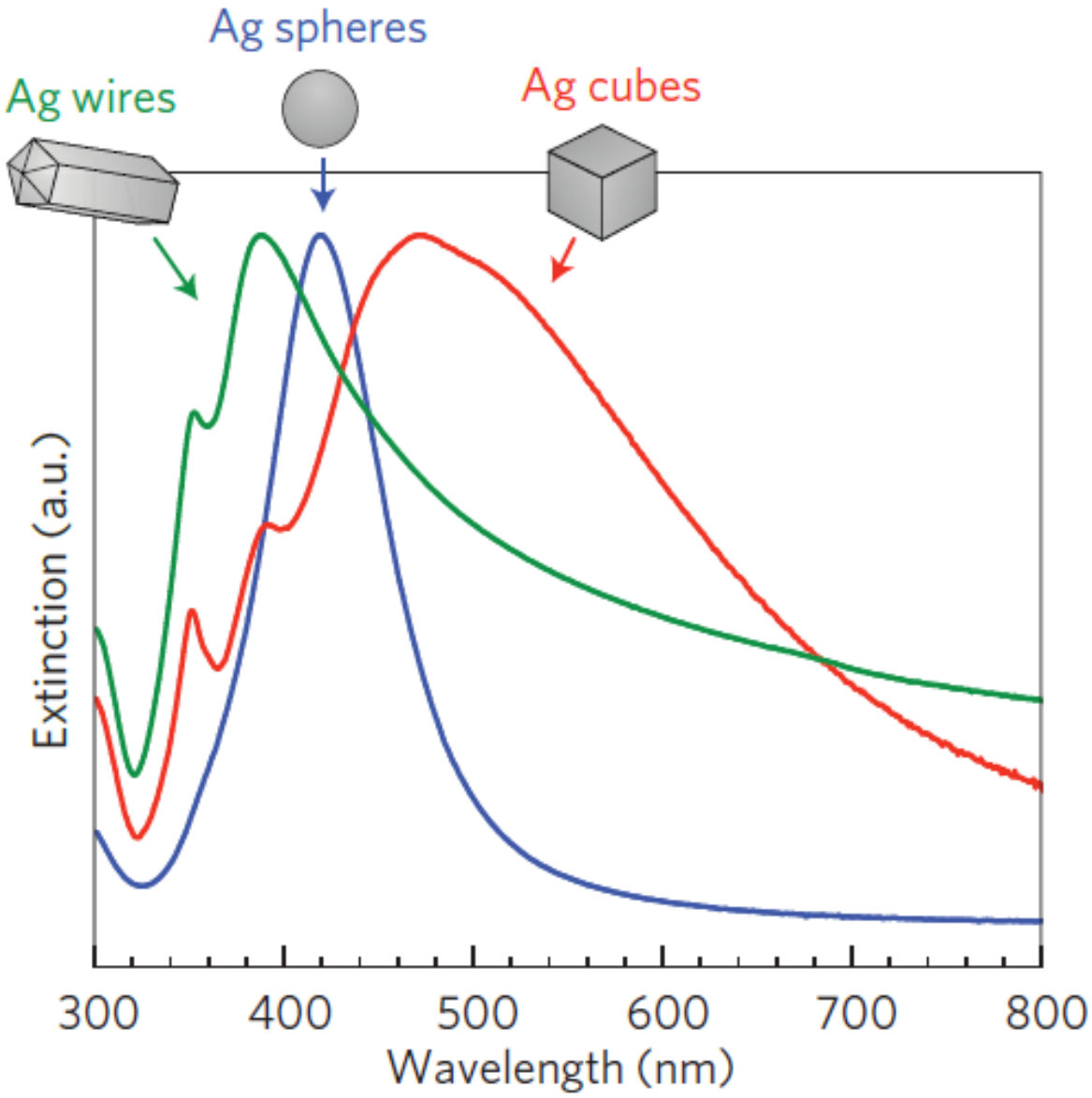

Figure 1.2.a. UV-vis extinction spectra for solutions of Ag cubes (79±12 nm edge length), Ag spheres (38±12 nm diameter) and Ag wires (90±12 nm diameter and >30 aspect ratio). Taken from Linic et al.[11]

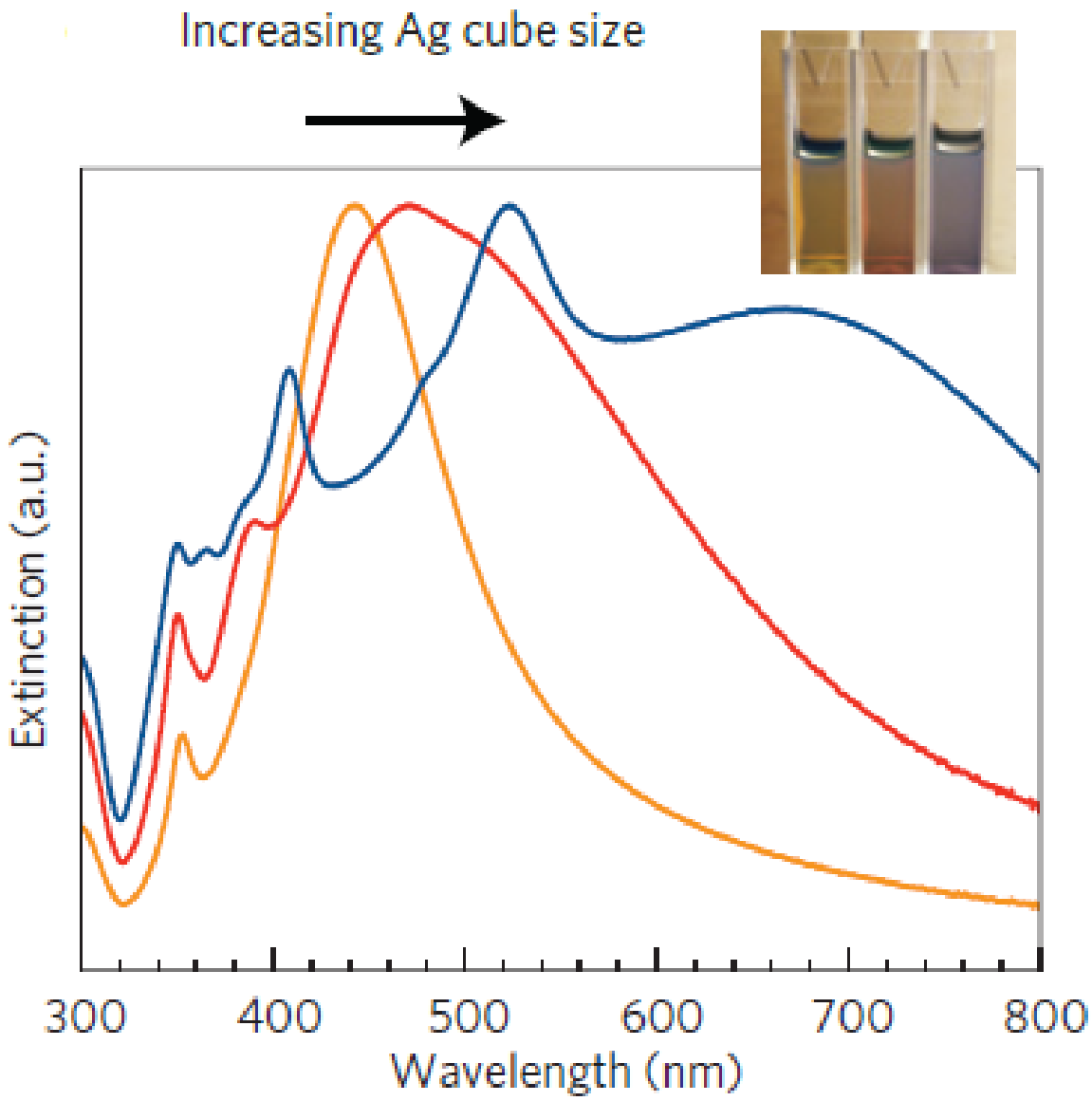

Figure 1.2.b. UV-vis extinction spectra of Ag nanocubes dispersed in ethanol as a function of size (56±8 nm, 79±13 nm and 129±7 nm edge lengths). Taken from Linic et al.[11]

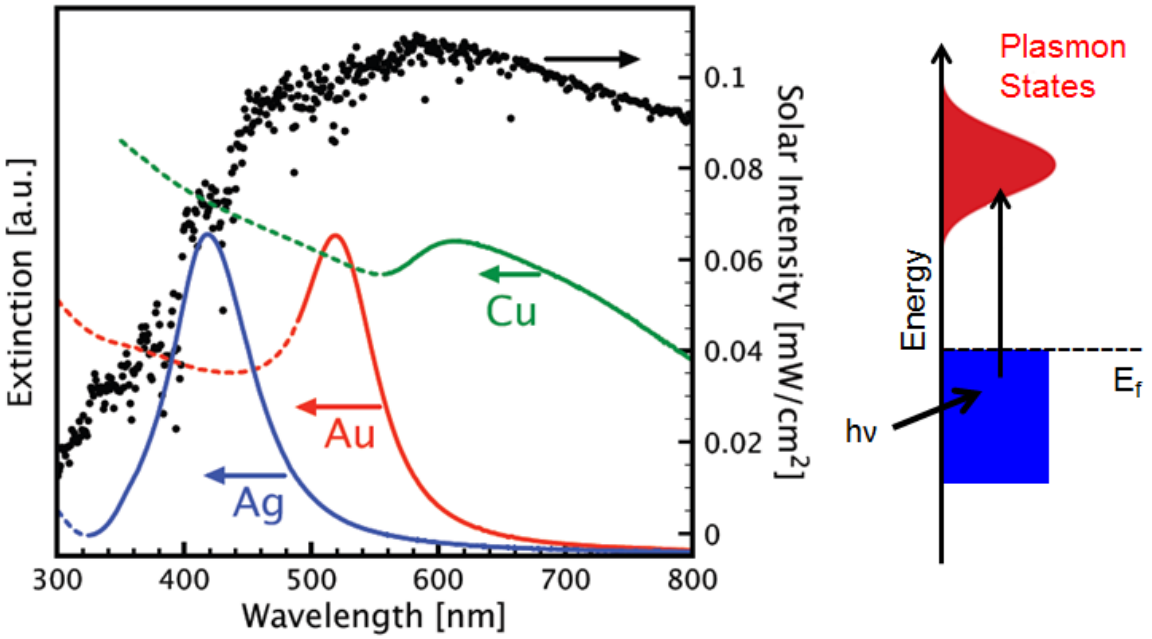

1.3.a 1.3.b

Figure 1.3.a. UV-vis extinction spectra of silver (38±12 nm), gold (25±5 nm) and copper (133±23 nm) spherical nanoparticles. 1.3.b. Schematic depicting the quantum mechanical representation of surface plasmon excitation. Taken from Linic et al.[11]

Quantum mechanically, surface plasmon can be defined as a quasi-particle, which is the collection of excited electrons that results from the coherent excitation of conduction electrons of metal nanoparticle as shown schematically in Figure 1.3.b. The experimental details about the interaction of light with metal nanoparticles can be measured using ultraviolet-visible (UV-vis) spectrophotometry. In UV-vis spectrophotometer, the extinction spectra, extinction of the light by the metal nanoparticles as a function of wavelength, can be measured. The resonance wavelength at which the maximum interaction happens between metal nanoparticle and incident light can be identified from the peak appear in the extinction spectra. In the measurement of the extinction spectrum of metal

nanoparticles using UV-vis spectrophotometer, we actually measure the fraction of light that is extinguished from a beam of light by the sample. This fraction of light is the optical energy that interacts with the sample, and it excites the surface plasmon in the metal nanoparticles of the sample.

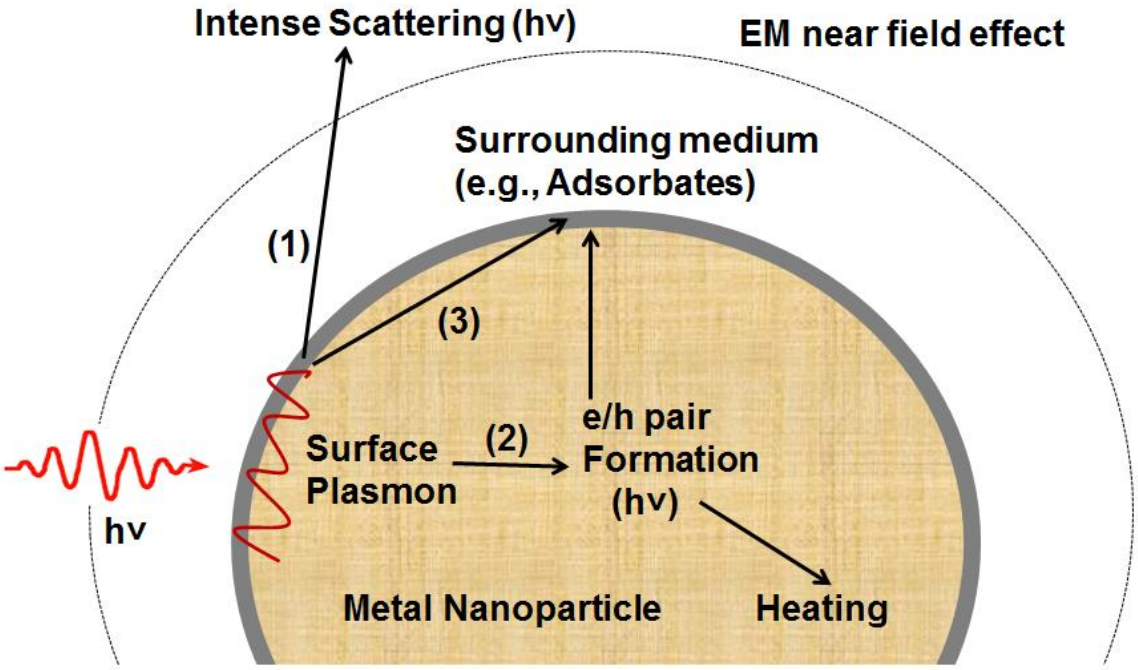

Figure 1.4. Schematic representation of surface plasmon (SP) decay mechanisms and SP mediated effects in metal nanoparticle. Paths (1), (2) and (3) represent relaxation mechanisms of surface plasmon through scattering, Landau damping and chemical interface damping, respectively. Adapted from Watanabe et al.[9]

Surface plasmon excited in metal nanoparticle can relax through different mechanisms as shown schematically in Figure 1.4. In an inert environment, surface plasmon excited in a metal nanoparticle can relax through radiative re-emission of electromagnetic energy (scattering of photons) at the same frequency as the

incident frequency (path 1 in Figure 1.4) or it can can dacay via Landau damping into energetic electron-hole (e^-/h^+) pair (path 2 in Figure 1.4), which eventually results in non-radiative absorption (example, heating) within the particle. Absorption is the major contribution to the extinction of small nanoparticles with diameter less than 10 nm. For larger nanoparticles, the extinction is dominated by scattering.

The intense scattering of the photons (path 1 in Figure 1.4) by the plasmonic nanoparticle mainly contributes to the concentration of the incoming light flux into small volume near the surface of the nanoparticle that result in highly confined optical fields near the surface. This surface plasmon mediated electromagnetic (EM) near field effect is described in more detail in section 1.2.1.1. Generally, in the presence of reactive chemical surrounding (e.g., adsorbates), the energetic electrons formed in the metal nanoparticle through Landau damping can interact with the surrounding. Additionally, the surface plasmon of a metal nanoparticle can decay directly into the surrounding (e.g., adsorbates) through the mechanism known as chemical interface damping (CID, path 3 in Figure 1.4).[9] It has been shown that surface plasmon mediated transient electron transfer from plasmonic metal nanoparticle to the surface adsorbate either directly via CID or indirectly through Landau damping can result in energetic electron-driven catalytic chemistry on the surface of plasmonic metal nanoparticles.[13,14] This process of surface plasmon electron mediated photochemistry is described in greater detail in section 1.2.1.2.

1.2.1.1. SP mediated electromagnetic near field effect

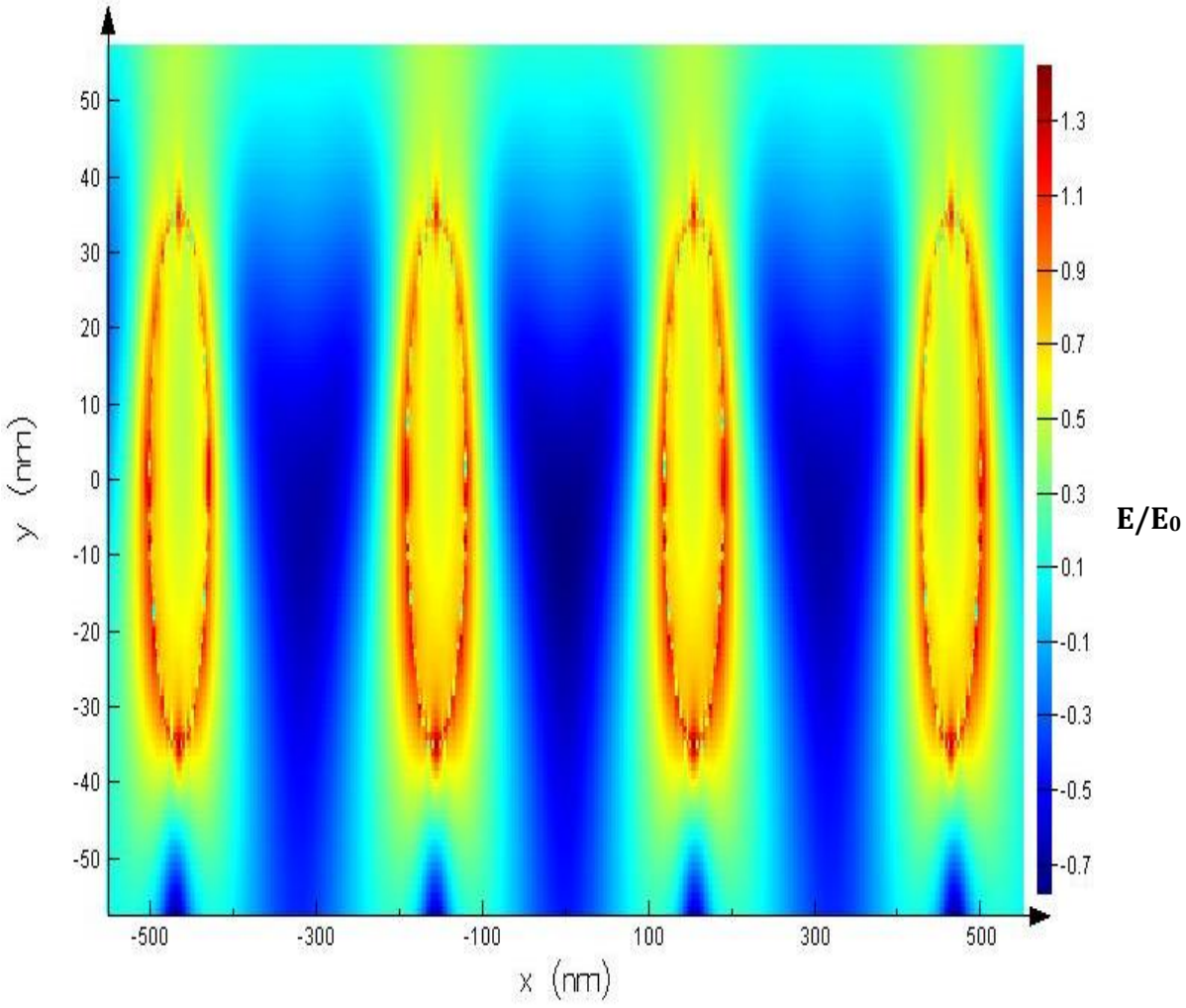

Figure 1.5.a. Spatial distribution of enhancement of electric field (E/E_0) in xy-plane for four isolated Ag particles (70 nm diameter) at SPR wavelength. The results are obtained from 2D FDTD simulation. E/E_0 values are in logarithmic scale.

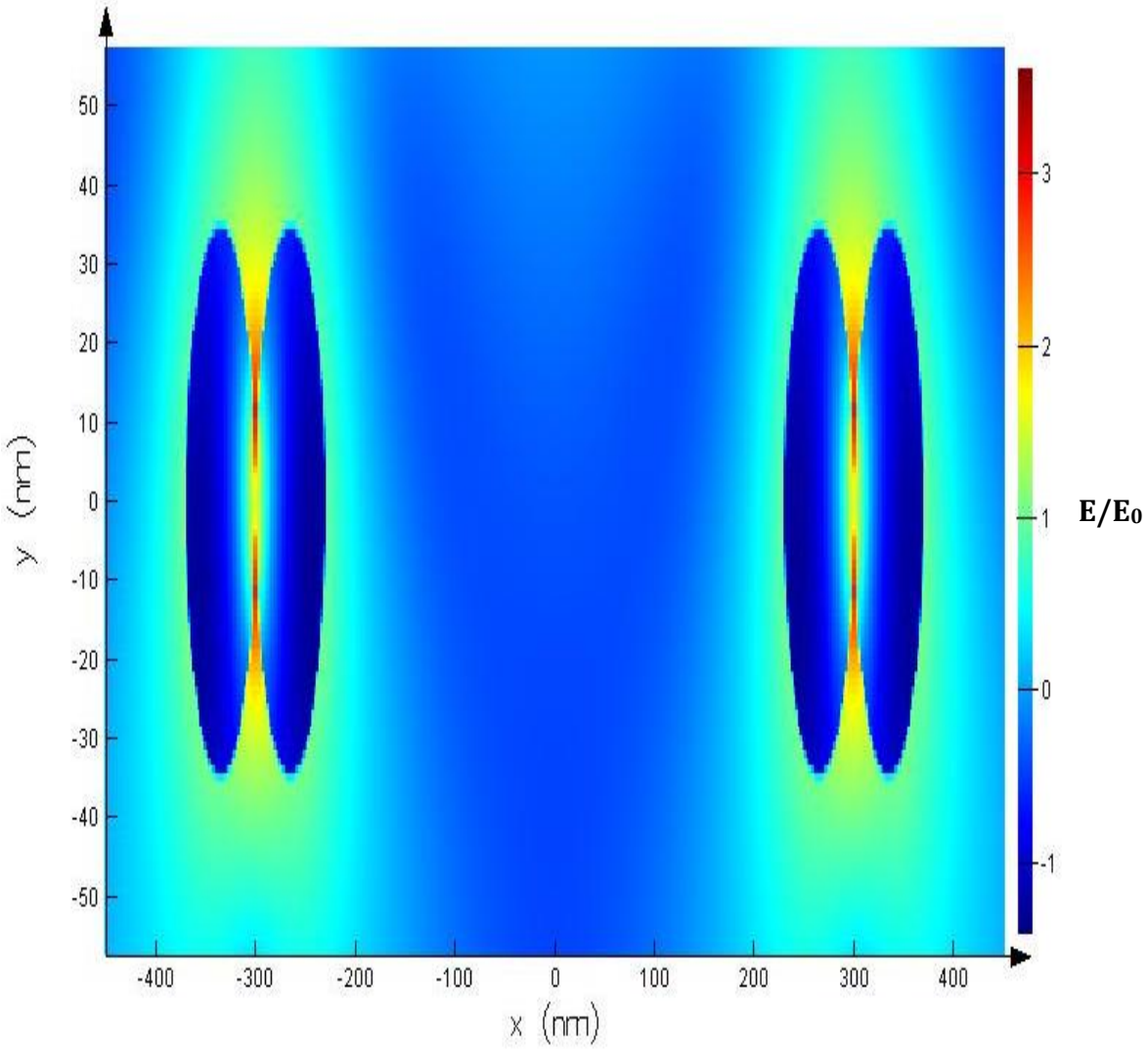

Figure 1.5.b. Spatial distribution of enhancement of electric field (E/E_0) in xy-plane for dimers of Ag particles (70 nm diameter) at SPR wavelength. The results are obtained from 2D FDTD simulation. E/E_0 values are in logarithmic scale.

The surface plasmon in plasmonic nanoparticle creates a concentration of charges near the surface as shown schematically in Figure 1.1, which in turn generates intense local electromagnetic fields. Thus, surface plasmons provide a powerful means of confining light, i.e., amplifying the light signal near the surface of plasmonic metal nanoparticle. For example, Figures 1.5.a and 1.5.b show the spatial

distribution of SP mediated enhancement of electric field for the electric field of the incident light (E/E_0) near the isolated Ag particles and closely spaced Ag particles (70 nm diameter), respectively. Since the intensity of the light is proportional to the square of the electric field (E^2), Figures 1.5.a and 1.5.b basically show that the enhancements for the intensity of the incident light are anywhere from $10^{2.6}$ at the surface of isolated Ag particles to more than 10^6 for closely spaced Ag particles.

The extraordinary ability of metallic nanostructure to produce highly confined optical fields near its surface (i.e., electromagnetic near field effect) can be used to increase the efficiency of the photovoltaics system, and to enhance the rate of photocatalysis through enhanced absorptions of photons within the system.[11] Similarly, it can be used to improve the sensitivity of a spectroscopic technique such as Raman spectroscopy.[15] The technique that uses the optical properties of plasmonic nanoparticles- the unique ability to confine optical fields, to enhance Raman signal is known as surface enhanced Raman spectroscopy (SERS), which is one of the most powerful tools, used to detect molecules in chemical sensors.[15] In chapter 3, the focus is to demonstrate how this electromagnetic near field effect of the plasmonic metal nanostructures can be exploited for selective molecular sensing applications using surface enhanced Raman spectroscopic technique.

1.2.1.2. SP electron mediated photochemistry

The extinction coefficients of the noble metal nanoparticles are several orders of magnitude larger compared to common organic dye molecules.[8] Therefore, the noble metal nanoparticles (Cu, Ag and Au) can harvest a large fraction of the

incident light and convert it into SP mediated energetic electrons available near their surfaces. The transient transfer of these SP mediated electrons from plasmonic metal nanoparticle to the surrounding (e.g., adsorbate) can result in energetic electron-driven chemistry in heterogeneous catalysis.[11]

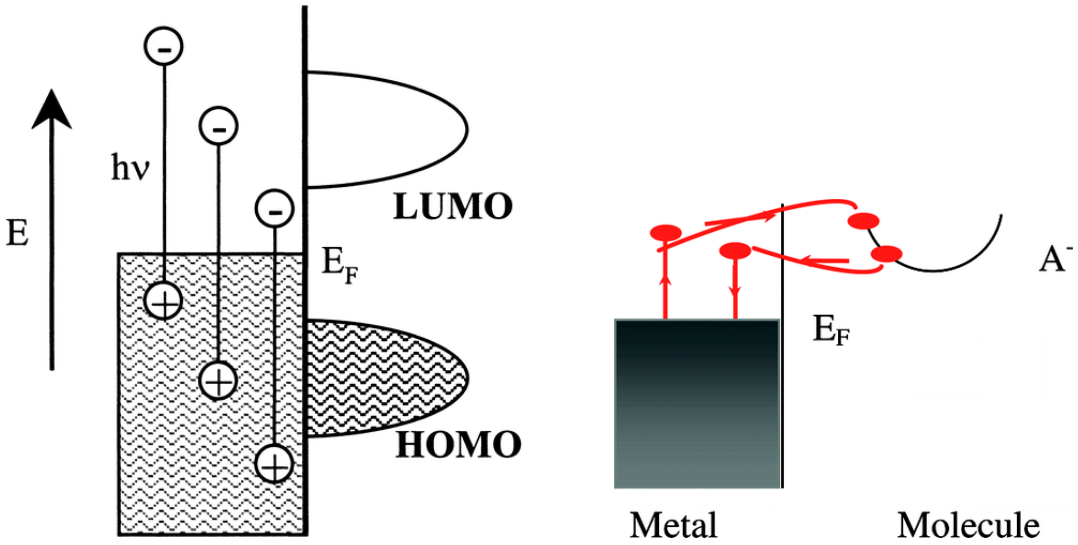

(a) (b)

Figure 1.6. (a). Schematic illustration of relative energies of excited electron–hole pairs generated in metal nanoparticle with respect to the HOMO and LUMO of the adsorbed molecule. Taken from Michaels et al.[16] (b). Schematic diagram of transient electron transfer from metal nanoparticle to adsorbed molecule. Taken from Brus.[17]

Heterogeneous catalysis involves series of steps including adsorption of reactant molecules on the surface of catalyst, reaction at an active site to form adsorbed product, and desorption of the product.[18,19,12] These elementary steps can be possibly controlled and enhanced by SP mediated electrons at metal nanoparticle/adsorbate interface.[11,16,17,20–24] For example, as described schematically in Figures 1.6.a-b, the excited (hot) electrons created in the metal nanoparticle by the decay of SP through Landau damping can play an important role

in heterogeneous catalysis by inducing charge and energy transfer from the metal nanoparticle to local environment (e.g., adsorbate). Similarly, the charge and energy transfer from metal nanoparticle to the surrounding is also possible through direct decay of surface plasmon into the surrounding through chemical interface damping.

1.2.2. Electronic and catalytic properties of metal nanostructures of controlled shapes

Metal nanoparticles synthesized using conventional synthesis techniques such as wet impregnation synthesis method are almost always quasi-spherical nanoparticles mainly terminated by low energy close-packed surface facets, such as (111) surface for fcc crystals and (0001) surface for hcp crystals.[12,25,26] The catalytic properties of these conventional quasi-spherical metal nanoparticles are limited by their intrinsic electronic structure of close-packed surface facets.[12,25,26] Recent advances made in the synthetic chemistry have shown that these limitations can be overcome by the synthesis of metal nanostructures of controlled shapes exposed with different surface facets (see Figures 1.7 and 1.8).[5,26,28,29] It has also been shown that the metal nanostructures of controlled shapes terminated by different surface facets can show inherently different electronic and catalytic properties (reaction rate and product selectivity) due to variation in the metal-metal interactions on the surface.[30,31] For example, the quasi-spherical silver particles dominated by Ag (111) facets exhibit ethylene selectivity to ethylene oxide (EO) of ~45% for commercially important ethylene epoxidation reaction.[30,31] Recently, it has been shown that well-defined silver nanostructures (Ag nanocubes and Ag nanowires) terminated by Ag

(100) surface facets show up to 80% of ethylene oxide selectivity (see Figure 1.9).[30] In chapter 5 of this thesis, the focus is on improving the performance of the catalysts containing silver nanocubes for the ethylene epoxidation reaction.

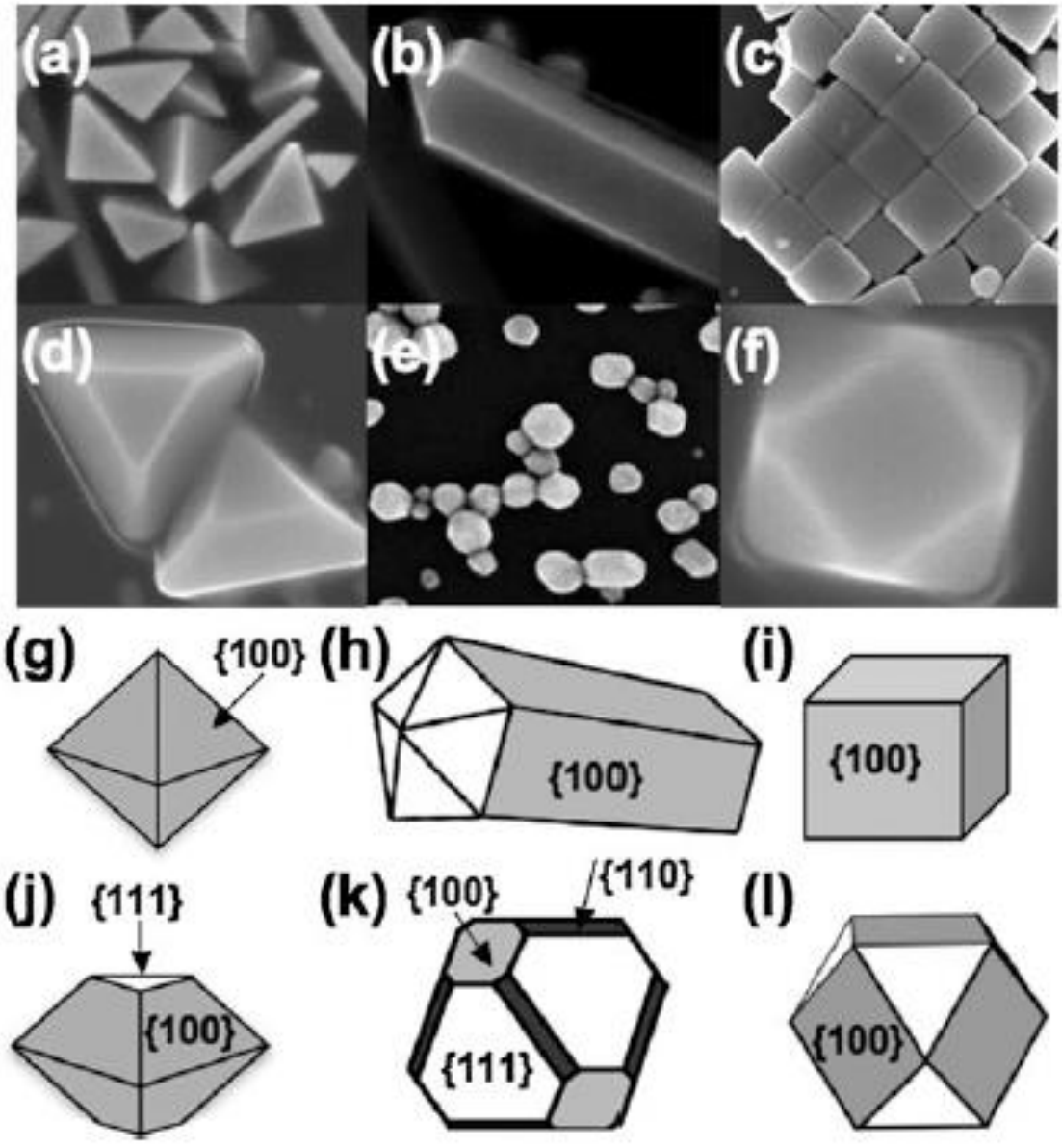

Figure 1.7. SEM images and structural models of different shapes of silver nanostructures: a, g) right bipyramids; b, h) pentagonal nanowires; c, i) nanocubes; d, j) truncated right bipyramids; e, k) quasi-spherical; f, l) truncated cubes. Taken from Linic and Christopher.[26]

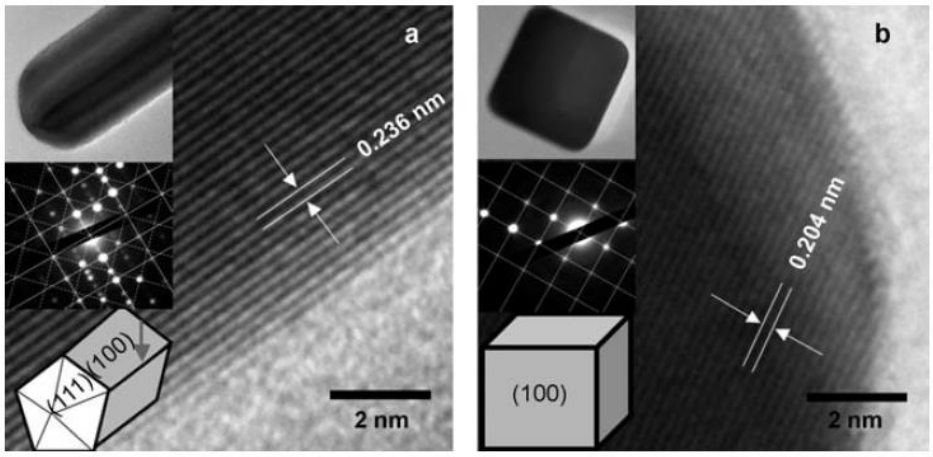

Figure 1.8. (a) HRTEM image of Ag nanowire. (b) HRTEM image of Ag nanocube. Insets show zoomed out TEM images of the nanostructures, electron diffraction patterns, and model structures. Taken from Christopher and Linic.[30]

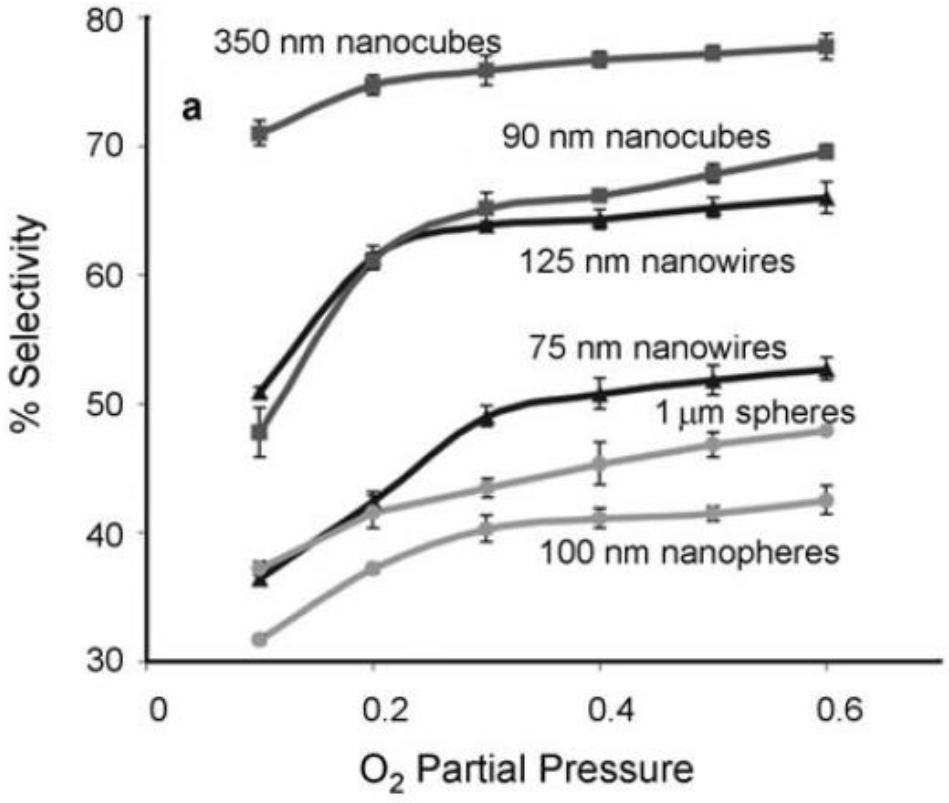

Figure 1.9. Ethylene selectivity to ethylene oxide (EO) observed for Ag nanocubes, Ag nanowires and Ag nanospheres of different sizes, as a function of oxygen partial pressure, during ethylene oxidation at T=510 K. Taken from Christopher and Linic.[30]

1.3. Spectroscopic techniques

1.3.1. Raman Spectroscopy[15]

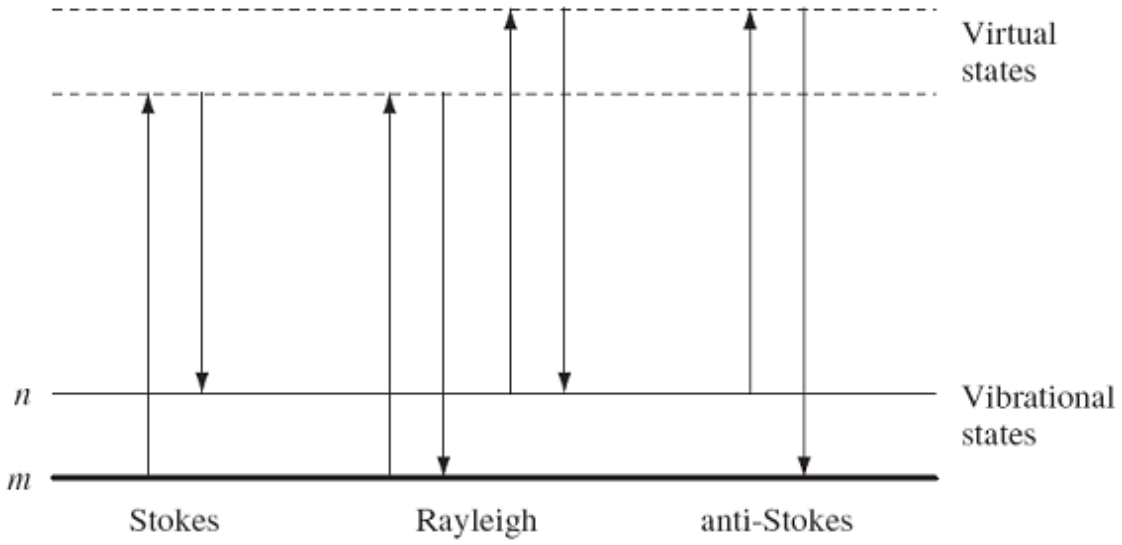

Figure 1.10. Schematic representation of the different possibilities of light scattering by a molecule. Taken from Smith and Dent.[15]

In chapter 3 of this thesis, the focus is on developing a sensitive and selective chemical characterization technique based on Raman spectroscopy. The working principle of Raman spectroscopy is based on scattering principles as shown in Figure 1.10.

When a molecule is excited by monochromatic laser light, the incident light can interact with the molecule and polarize the electron cloud of the molecule to form a short-lived state called a virtual state. If only electron cloud distortion is involved in scattering, the photon will be scattered with same frequency. This elastic scattering called Raleigh scattering is the most intense signal, since most of the photons scatter in this way. If nuclear motion is involved during scattering process, energy will be

transferred either from incident photon to the molecule or from the molecule to the scattered photon. This inelastic scattering is called Raman scattering and it is widely used to provide molecular vibrational information. The Raman scattering from ground vibrational state (m) to excited vibrational state (n) through absorption of energy by the molecule is called Stokes Raman scattering. The scattering from excited vibrational state (n) to the ground state (m) is called anti-Stokes Raman scattering. At room temperature, anti-Stokes scattering is weak compared to Stokes scattering due to decreased population of the excited vibrational states. Because of this reason, only Stokes-Raman scattering is generally measured in Raman Spectroscopy. The main drawback in Raman spectroscopy is that the signal is very weak because only one in 10^6-10^8 scattered photons is Raman scattered. Due to this lower Raman cross section, it suffers from the limitation of poor sensitivity.

1.3.2. Surface enhanced Raman spectroscopy (SERS)[32]

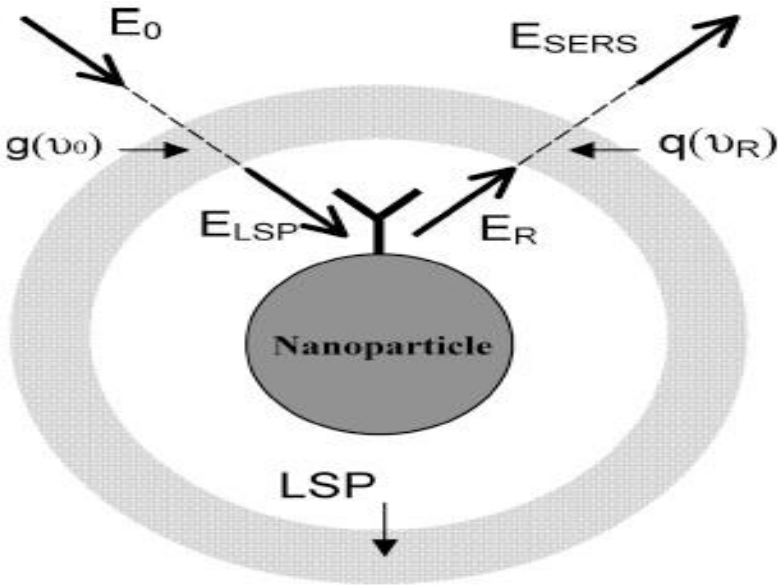

Figure 1.11. Schematic representation of electromagnetic enhancement mechanism in surface enhanced Raman spectroscopy. Taken from Mahmoud et al.[33]

The improvement in the sensitivity of a spectroscopic technique can be achieved by enhancing the light-matter (analyte) interaction for the given incident signal. The electromagnetic near field effect of the metal nanoparticles can be used to control, manipulate and enhance light-matter interactions. The technique that uses plasmonic metal nanoparticles, to enhance Raman signal is known as surface enhanced Raman spectroscopy (SERS).[32] In this technique, Raman spectrum is measured for the analyte adsorbed on the surface of plasmonic nanoparticles. There are two accepted mechanisms that responsible for enhancements of Raman scattering observed from molecules near plasmonic metal nanostructures, the charge transfer (CT) and electromagnetic (EM) mechanisms. The CT mechanism involves the excitation of an electron from the metal surface to unpopulated orbitals in the molecule. In general, it is thought that the CT mechanism contributes a smaller magnitude of the surface enhancements.[32] Figure 1.11 shows schematic representation of electromagnetic enhancement mechanism responsible for enhancement in Raman signal.

In Figure 1.11, molecules are assumed to be adsorbed on the surface of nanoparticle. The electric field, created by the localized surface plasmon (LSP) near the surface of metal nanoparticle schematically shown in Figure 1.11, can enhance electric fields of the incident and scattered photons during Raman scattering by a molecule adsorbed on plasmonic nanoparticle. As shown in Figure 1.11, the electric field of incident photon interacts with LSP and it is enhanced by a factor, $g(\nu_0)$. Thus, the actual magnitude of the electric field (E_{LSP}) of the photon that excites molecule to a virtual state is $g(\nu_0)E_0$. In the absence of plasmonic nanoparticle, this magnitude

would be E_0. Thus, the electric field of the incident signal is amplified by the factor, $g(\nu_0)$. The photon with electric field, $E_{LSP} = g(\nu_0)E_0$, is then scattered by the molecule, and the magnitude of the electric field of scattered photon (E_R) is proportional to incident electric field (E_{LSP}) and polarizability of the molecule (α_R). The electric field of scattered photon (E_R) again interacts with the field created by the LSP, and it is enhanced by the magnitude, $q(\nu_R)$. Finally, the light signal with electric field, $E_{SERS}=q(\nu_R)E_R$, is detected in SERS. Thus, the electric field of photon measured in SERS is enhanced both at incident (ν_0) and scattered frequencies (ν_R) by LSP compared to Raman signal in the absence of metal nanoparticle. The intensity for Raman signal, I_{RS}, can be expressed as[33]

$$I_{RS} \propto (\alpha_R)^2 (\nu_0)^4 I_0$$

where, α_R - Raman polarizability of the vibrational band, ν_0, and I_0 are the frequency and intensity of the incident laser light, respectively. The electric field of Raman signal is enhanced by $g(\nu_0)$ at incident frequency and $q(\nu_R)$ at scattered frequency in SERS due to LSP of nanoparticle. Since the intensity is proportional to the square of the electric field, the SERS intensity (I_{SERS}) can be expressed as[33]

$$I_{SERS} \propto g^2(\nu_0) q^2(\nu_R) (\alpha_R)^2 (\nu_0)^4 I_0$$

The magnitude of the enhancement in the electric fields- $g(\nu_0)$ and $q(\nu_R)$ can differ depending on the strengths of LSP fields at the incident (ν_0) and scattered (ν_R) frequencies. The strongest enhancement in the electric field of the interacting light with LSP happens at the surface plasmon resonance (SPR) frequency. This SPR

frequency can be identified by the peak in the extinction spectra of the metal nanoparticles.

Alternatively, the Raman scattering can also be thought of absorption of photons at the incident frequency followed by instantaneous emission of photons from the molecules at the scattered frequency.[32,34] The EM mechanism in SERS can then be explained in terms of the concentration of photons near the surface of plasmonic metal nanoparticles due to surface plasmon, thereby creating an enhanced interaction between the incident photons and the adsorbed molecules through plasmon-enhanced absorption of photons by molecule, followed by the plasmon-enhanced (stimulated) emission of Raman shifted photons from the molecule.[32,34] Since the enhancement of each vibrational mode of a molecule is dependent on both the strength of LSP at the incoming laser wavelength and the LSP strength at the Raman shifted wavelength, it is possible to have different enhancements for different vibrational modes in the same molecule. In chapter 3, we focus to demonstrate the design of plasmonic substrates that selectively enhance specific Raman vibrational modes to achieve selective molecular sensing.

1.4. Theoretical techniques

1.4.1. Finite-difference Time-domain simulation

Finite-difference time-domain (FDTD) is a computational electrodynamics-modeling tool, which solves discretized Maxwell equations in space and time.[35] FDTD optical simulations were performed using Lumerical FDTD package to simulate the spatial distribution of electric field enhancements (E/E_0) from isolated

and closely spaced silver nanoparticles shown in Figure 1.5.a and 1.5.b, respectively, and to simulate the extinction cross section of copper nanoparticle as a function of wavelength of incident light in chapter 4. The Drude-Lorentz model was used to represent the optical properties of silver and copper metal nanoparticles.[35] The empirical optical constants of silver and copper metals were taken from Palik.[36] For all simulations, the periodic boundary conditions were used in x- and y-directions, while the perfectly matched layer (PML) boundary condition was used in the z-direction. The extinction cross sections as a function of wavelength were calculated using the total-field/scattered-field (TFSF) formalism.[35] The incident light sources used for the simulations were 300-1000 nm and 400-1000 nm Gaussian sources for the simulations with silver and copper nanoparticles, respectively.

1.5. Scope of the thesis

The objective of this thesis was to 1) exploit the SP mediated electromagnetic near field effect of plasmonic metal nanostructures of controlled shapes for selective molecular sensing applications, 2) exploit the SP mediated electrons in plasmonic metal nanoparticles to achieve selective catalytic transformation, and 3) improve the performance of metal nanostructures of controlled shapes for catalytic applications. This thesis is organized into 6 chapters. In this chapter 1, a brief introduction to well-defined metal nanostructures, and their unique optical and catalytic properties, and detailed descriptions of the important spectroscopic and theoretical techniques utilized in this work are provided.

In chapter 2, we present a quantum mechanical model to simulate the optical

properties of plasmonic metal nanoparticles. Using this quantum model we describe the quantum mechanical nature of surface plasmon, and the condition that needs to be met to achieve surface plasmon resonance in metal nanoparticles. We also provide the details about how the optical properties vary with size of the metal nanoparticles. The different possible decay mechanisms of surface plasmons in metal nanoparticles and their applications in molecular sensing and catalysis are also discussed.

In chapter 3, we demonstrate the design of plasmonic substrates that selectively enhance targeted Raman vibrational bands in a molecule. We show that by changing the shape of plasmonic Ag nanostructures in Ag aggregates we can selectively control their optical properties and the degree to which they enhance different vibrational bands. We demonstrate that the selective vibrational band enhancements observed in this study are due to the electromagnetic near field effect of plasmonic metal nanostructures. We also shed light on critical design parameters for the synthesis of plasmonic nanosubstrates for selective detection of a molecule in a mixture of compounds.

In chapter 4, we demonstrate an approach to manipulate the oxidation state of plasmonic copper (Cu) nanoparticle catalysts under operating propylene epoxidation conditions and thereby change the selectivity of the catalyst to favor the formation of propylene oxide. The approach takes advantage of the strong interactions of Cu nanoparticles with visible light manifested in the photo-excitation of the surface plasmon resonance. We show that heterogeneous catalysts containing

Cu nanoparticles exhibit an increase in the steady state selectivity to propylene oxide when illuminated with visible light. This increase in the selectivity is accompanied by light-induced change in the oxidation state of the surface Cu atoms from Cu-oxide (light off) to Cu metal (light on).

In chapter 5, we show that the catalysts containing sulfurized silver (Ag) nanocubes treated with polysulfide (Na_2S_x) solution exhibit better performance in terms of catalytic activity and selectivity towards the desired product compared to Ag nanocube catalysts during the ethylene oxidation reaction. We demonstrate that the removal of polymeric capping agent (polyvinylpyrrolidone, PVP) from the surface of Ag nanocubes is critical and the PVP removal by the polysulfide solution is mainly responsible for the improved performance observed with the sulfurized Ag nanocubes.

Finally, chapter 6 will present major conclusions drawn in this thesis and suggestions for future work.

1.6. References

(1) Schuller, J. A.; Barnard, E. S.; Cai, W.; Jun, Y. C.; White, J. S.; Brongersma, M. L. Plasmonics for extreme light concentration and manipulation. Nat Mater 2010, 9, 193–204.

(2) Jain, P. K.; Huang, X.; El-Sayed, I. H.; El-Sayed, M. A. Review of Some Interesting Surface Plasmon Resonance-enhanced Properties of Noble Metal Nanoparticles and Their Applications to Biosystems. Plasmonics 2007, 2, 107–118.

(3) McDonagh, C.; Burke, C. S.; MacCraith, B. D. Optical Chemical Sensors. Chem. Rev. 2008, 108, 400–422.

(4) El-Sayed, M. A. Some Interesting Properties of Metals Confined in Time and Nanometer Space of Different Shapes. Acc. Chem. Res. 2001, 34, 257–264.

(5) Xia, Y.; Halas, N. J. Shape-Controlled Synthesis and Surface Plasmonic Properties

of Metallic Nanostructures. MRS Bulletin 2005, 30, 338–348.

(6) Xia, Y.; Campbell, D. J. Plasmons: Why Should We Care? J. Chem. Educ. 2007, 84, 91.

(7) Ghosh, S. K.; Pal, T. Interparticle Coupling Effect on the Surface Plasmon Resonance of Gold Nanoparticles: From Theory to Applications. Chem. Rev. 2007, 107, 4797–4862.

(8) Link, S.; El-Sayed, M. A. Optical properties and ultrafast dynamics of metallic nanocrystals. Annu Rev Phys Chem 2003, 54, 331–366.

(9) Watanabe, K.; Menzel, D.; Nilius, N.; Freund, H.-J. Photochemistry on Metal Nanoparticles. Chem. Rev. 2006, 106, 4301–4320.

(10) Lu, X.; Rycenga, M.; Skrabalak, S. E.; Wiley, B.; Xia, Y. Chemical Synthesis of Novel Plasmonic Nanoparticles. Annual Review of Physical Chemistry 2009, 60, 167–192.

(11) Linic, S.; Christopher, P.; Ingram, D. B. Plasmonic-metal nanostructures for efficient conversion of solar to chemical energy. Nat. Mater. 2011, 10, 911–921.

(12) Bell, A. T. The Impact of Nanoscience on Heterogeneous Catalysis. Science 2003, 299, 1688–1691.

(13) Christopher, P.; Xin, H.; Marimuthu, A.; Linic, S. Singular characteristics and unique chemical bond activation mechanisms of photocatalytic reactions on plasmonic nanostructures. Nature Materials 2012.

(14) Christopher, P.; Xin, H.; Linic, S. Visible-light-enhanced catalytic oxidation reactions on plasmonic silver nanostructures. Nat. Chem. 2011, 3, 467–472.

(15) Smith, E.; Dent, G. Modern Raman Spectroscopy - A Practical Approach; 2005.

(16) Michaels, A. M.; Jiang; Brus, L. Ag Nanocrystal Junctions as the Site for Surface-Enhanced Raman Scattering of Single Rhodamine 6G Molecules. J. Phys. Chem. B 2000, 104, 11965–11971.

(17) Brus, L. Noble Metal Nanocrystals: Plasmon Electron Transfer Photochemistry and Single-Molecule Raman Spectroscopy. Acc. Chem. Res. 2008, 41, 1742–1749.

(18) Ertl, G.; Knözinger, H.; Weitkamp, J. Handbook of heterogeneous catalysis; VCH, 1997.

(19) Horváth, I. T. Encyclopedia of catalysis; Wiley-Interscience, 2003.

(20) Lindstrom, C. D.; Zhu, X.-Y. Photoinduced electron transfer at molecule-metal interfaces. Chem. Rev. 2006, 106, 4281–4300.

(21) Zimmermann, F. M.; Ho, W. State resolved studies of photochemical dynamics

at surfaces. Surface Science Reports 1995, 22, 127–247.

(22) Petek, H.; Ogawa, S. Femtosecond time-resolved two-photon photoemission studies of electron dynamics in metals. Progress in Surface Science 1997, 56, 239–310.

(23) Al-Shamery, K. Photochemistry at nanoparticulate surfaces. Journal of Physics Condensed Matter 2006, 18, 1581.

(24) Zhou, X.-L.; Zhu, X.-Y.; White, J. M. Photochemistry at adsorbate/metal interfaces. Surface Science Reports 1991, 13, 73–220.

(25) Linic, S.; Christopher, P. Overcoming Limitation in the Design of Selective Solid Catalysts by Manipulating Shape and Size of Catalytic Particles: Epoxidation Reactions on Silver. ChemCatChem 2010, 2, 1061–1063.

(26) Nørskov, J. K.; Bligaard, T.; Rossmeisl, J.; Christensen, C. H. Towards the computational design of solid catalysts. Nat Chem 2009, 1, 37–46.

(27) Sun, Y.; Xia, Y. Shape-Controlled Synthesis of Gold and Silver Nanoparticles. Science 2002, 298, 2176–2179.

(28) Xia, Y.; Xiong, Y.; Lim, B.; Skrabalak, S. E. Shape-Controlled Synthesis of Metal Nanocrystals: Simple Chemistry Meets Complex Physics? Angewandte Chemie International Edition 2009, 48, 60–103.

(29) Christopher, P.; Linic, S. Shape- and Size-Specific Chemistry of Ag Nanostructures in Catalytic Ethylene Epoxidation. ChemCatChem 2010, 2, 78–83.

(30) Christopher, P.; Linic, S. Engineering Selectivity in Heterogeneous Catalysis: Ag Nanowires as Selective Ethylene Epoxidation Catalysts. J. Am. Chem. Soc. 2008, 130, 11264–11265.

(31) Ru, E. L.; Etchegoin, P. Principles of Surface-Enhanced Raman Spectroscopy: and related plasmonic effects; 1st ed.; Elsevier Science, 2008.

(32) Mahmoud, M. A.; Tabor, C. E.; El-Sayed, M. A. Surface-Enhanced Raman Scattering Enhancement by Aggregated Silver Nanocube Monolayers Assembled by the Langmuir–Blodgett Technique at Different Surface Pressures. J. Phys. Chem. C 2009, 113, 5493–5501.

(33) Gray, S. K. Surface Plasmon-Enhanced Spectroscopy and Photochemistry. Plasmonics 2007, 2, 143–146.

(34) Zhao, J.; Pinchuk, A. O.; McMahon, J. M.; Li, S.; Ausman, L. K.; Atkinson, A. L.; Schatz, G. C. Methods for describing the electromagnetic properties of silver and gold nanoparticles. Acc. Chem. Res. 2008, 41, 1710–1720.

(35) Palik, E. D. Handbook of Optical Constants of Solids, Five-Volume Set: Handbook of Optical Constants of Solids: Volume 1; Academic Press, 1985.

CHAPTER 2

Quantum mechanical model of surface plasmon

2.1. Summary

This chapter presents a quantum mechanical model to simulate the optical properties of plasmonic metal nanoparticles. The model describes the quantum mechanical nature of surface plasmon, and the condition that needs to be met to achieve surface plasmon resonance in metal nanoparticles. Based on the results obtained from the simulations, the details about how the optical properties vary with size of the metal nanoparticles are also provided. The different possible decay mechanisms of surface plasmons in metal nanoparticles and their applications in molecular sensing and catalysis are also discussed.

2.2. Quantum model of electrons in a box[1]

To understand the quantum mechanical nature of surface plasmon in metal nanoparticles, the optical properties of spherical silver nanoparticles were simulated using quantum model of electrons in a box reported in the literature.[1,2] In this model, the conduction electrons of metal nanoparticle are considered as free electrons in a cubic potential well with infinite sizes.[1,2] The one electron wave functions of this model can be expressed as

$$\psi_{hkl} = \frac{8}{L^3}\sin\left(\frac{h\pi x}{L}\right)\sin\left(\frac{k\pi y}{L}\right)\sin(\frac{l\pi z}{L}) \quad (1)$$

where h, k and l are positive integers, and L is the length of the edge of the potential well. The energy levels corresponding to the wave functions shown in equation (1) are

$$E_{hkl} = E_0(h^2+k^2+l^2) \quad (2)$$

where

$$E_0 = \frac{\pi^2\hbar^2}{2L^2m} \quad (3)$$

E_0 can also be expressed in terms of Fermi energy (E_F) as

$$E_0 = \frac{E_F}{l_f^2} \quad (4)$$

where l_f is the point of intersection of the l-axis with the Fermi surface as shown in Figure 2.1.

2.3. Optical properties of metal nanoparticles[1,2]

The optical properties of metal nanoparticles can be simulated in terms of dielectric function (ε) using the expression shown below in equation (5)

$$\varepsilon(\omega) = \varepsilon_\infty(\omega) + \frac{\omega_p^2}{N}\sum_{i,f}^{f}\frac{S_{if}(F_i-F_f)}{\omega_{if}^2-\omega^2+i\omega\vartheta_{i,f}} \quad (5)$$

The first part in the right side of equation (5), $\varepsilon_\infty(\omega)$, represents contribution from the inter-band transition to the dielectric function. In noble metal nanoparticles, this

inter-band transition is due to the excitation of electrons from d-band to unfilled s-band states. The second part represents the intra-band excitation of electrons due to surface plasmon excitation from half-filled s-band below Fermi level to unfilled s-band states above the Fermi level in noble metal nanoparticles (Cu, Ag and Au). In equation (5), ω_p is the bulk plasma frequency; F_i and F_f represent the Fermi-Dirac distribution function of intial and final states; S_{if}, ω_{if} and ν_{if} are oscillator strength, transition frequency and damping of (surface plasmon) dipole transition from initial state 'i' to final state 'f', respectively; N is the total number of electrons in the box ($N = l_f \times l_f \times l_f$).

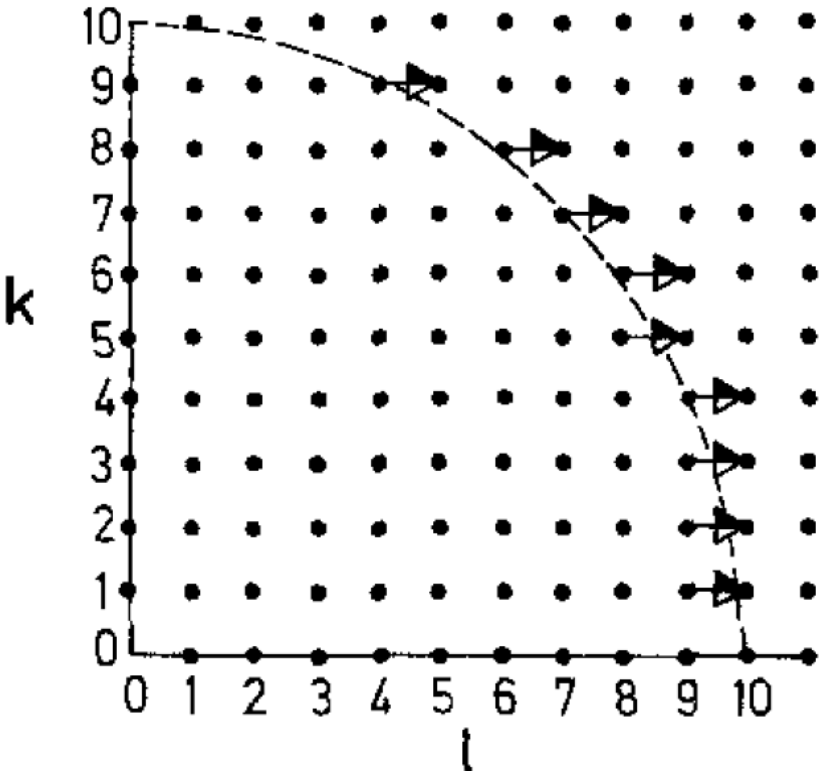

Figure 2.1. Schematic illustration of allowed dipole transitions for 1000 electrons in a box. The quadratic circle shows the Fermi surface. The dipole transition corresponding to Δl=1 in the 'kl' plane are shown by the arrows. Taken from Genzel et al.[1]

By using the cubic symmetry, the dipole transition in equation (5) can be reduced in terms of only horizontal transitions. The contribution of the dipole transition to the dielectric function then depends on initial and final values of only 'l' as shown in Figure 2.1. Figure 2.1 shows an example of allowed dipole transitions in 'kl' plane of 'khl' space for 1000 electrons in a box. Using this approximation, the summation in equation (5) can be reduced to summation over 'l' and 'Δl' with appropriate degeneracy factors, and the real and imaginary components of the dielectric function can be written as equations shown below

$$\varepsilon_1(\omega) = \varepsilon_\infty(\omega) + \omega_p^2 \sum_{\Delta l}^{1,3..} \sum_{l}^{l_f} \frac{S_{l,\Delta l}(\omega_{l,\Delta l}^2 - \omega^2)}{(\omega_{l,\Delta l}^2 - \omega^2)^2 + \omega^2 \vartheta_{l,\Delta l}^2} \qquad (6)$$

and

$$\varepsilon_2(\omega) = \omega_p^2 \sum_{\Delta l}^{1,3..} \sum_{l}^{l_f} \frac{S_{l,\Delta l}\, \omega\, \vartheta_{l,\Delta l}}{(\omega_{l,\Delta l}^2 - \omega^2)^2 + \omega^2 \vartheta_{l,\Delta l}^2} \qquad (7)$$

where

$$S_{l,\Delta l} = \frac{8}{\pi l_f^3} \frac{l^2}{\Delta l^2} \qquad (8)$$

and

$$\omega_{l,\Delta l} = \Delta l\, (2l + \Delta l) \frac{E_0}{h} \qquad (9)$$

The value used for $\nu_{l,\Delta l}$ in the simulation of dielectric functions of silver nanoparticle was 0.016 eV, which corresponds to the reciprocal life time of electrons in bulk silver.[1] A constant value of 4 was used for the ε_∞.[1]

By using quasi-static approximation (i.e., particle size is much smaller than wavelength of the incident light), the real and imaginary components of the

dielectric constant calculated from equations (6) and (7) can be used to calculate the extinction coefficient as shown in equation (10) below.[1,2]

$$K_{ext}(\omega) = \frac{9f\epsilon_m^{3/2}}{c} \frac{\omega\, \varepsilon_2(\omega)}{(\varepsilon_1(\omega)+2\varepsilon_m)^2+\varepsilon_2(\omega)^2} \qquad (10)$$

Extinction cross section can be expressed as volume of the particle times the $K_{ext}(\omega)$,

$$\sigma_{ext}(\omega) = \frac{9f\epsilon_m^{3/2}}{c} V_0 \frac{\omega\, \varepsilon_2(\omega)}{(\varepsilon_1(\omega)+2\varepsilon_m)^2+\varepsilon_2(\omega)^2} \qquad (11)$$

where ε_m is the dielectric constant of the medium. The value of dielectric constant of the medium (glass) used in the simulation was 2.25.[1]

The real and imaginary components of dielectric function calculated using equations (6) and (7), and the extinction efficiency (ratio of extinction cross section to geometric cross section) of silver nanoparticle of 4 nm size (16x16x16 electrons in a box) calculated using the equation (11) are shown in Figures 2.2.a-2.2.c, respectively. Figure 2.2.a shows three distinct regions for the values of imaginary components of dielectric function as function of excitation energy. These regions correspond to dipole transitions with Δl=1, Δl=3 and Δl=5, respectively, as labeled in the figure.[1] It can also be seen from Figure 2.2.a that the values of imaginary component of dielectric function for Δl=1 dipole transition are ~ 2 and 3 orders of magnitude higher compared to Δl=2 and Δl=3 dipole transitions, respectively. These results indicate that the dipole transitions (excitations) of low energy excited electrons (Δl=1) are stronger compared to high energy electrons (Δl>1) for 4 nm silver particle. Figure 2.2.c shows fine structure (discrete peaks) for the surface plasmon resonance in the extinction spectrum (near 3 to 4 eV) for 4 nm sized small

silver nanoparticle, which indicates that the quantum size effect could play the role in the surface plasmon resonance of small metal nanoparticles.[1] Furthermore, the simulated extinction spectrum for large particle such as particle of 32 nm size (128x128x128 electrons in a box) in Figure 2.3.a show broad surface plasmon resonance with extinction peak near ~3.1 eV (400 nm), which is consistent with the expected surface plasmon resonance peak of silver nanoparticles.[1–4] These results confirm that this simple quantum model based on electrons in a box can be used to simulate the optical properties of plasmonic metal nanoparticles.

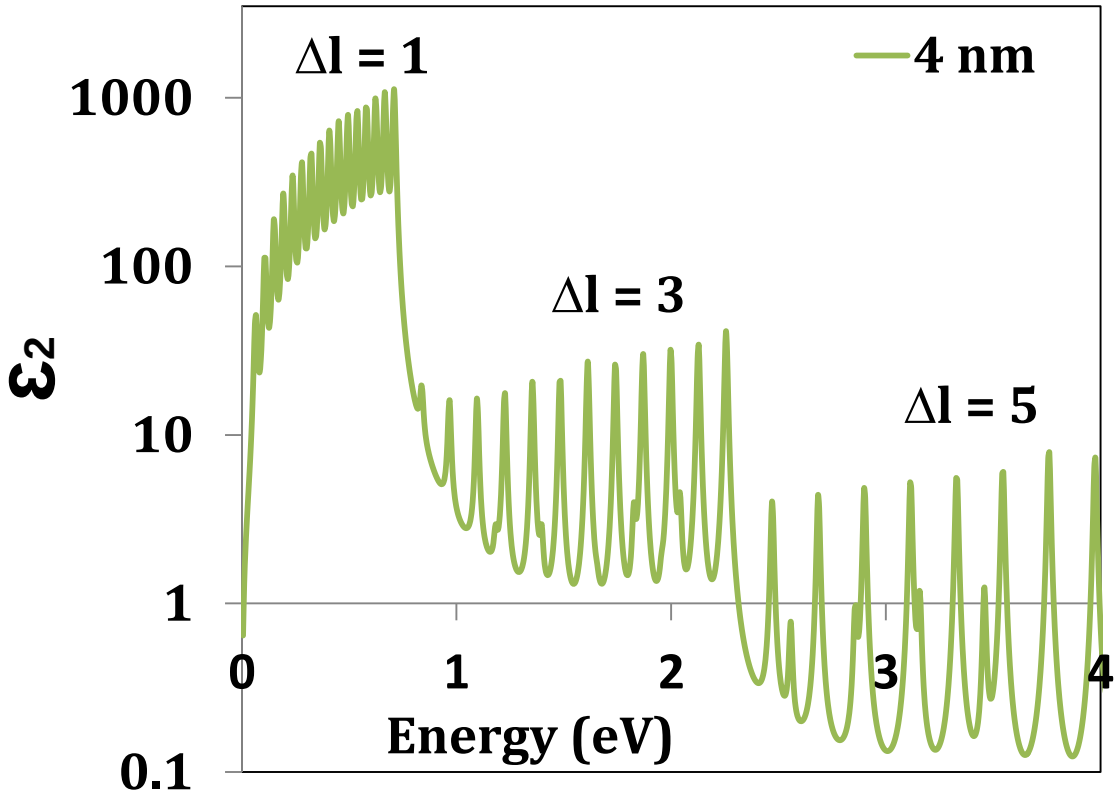

Figure 2.2.a. Imaginary component of dielectric function of silver nanoparticle of 4 nm size as function of excitation energy calculated using the quantum model. The region dominated by Δl=1, Δl=3 and Δl=5 dipole transitions are also shown.

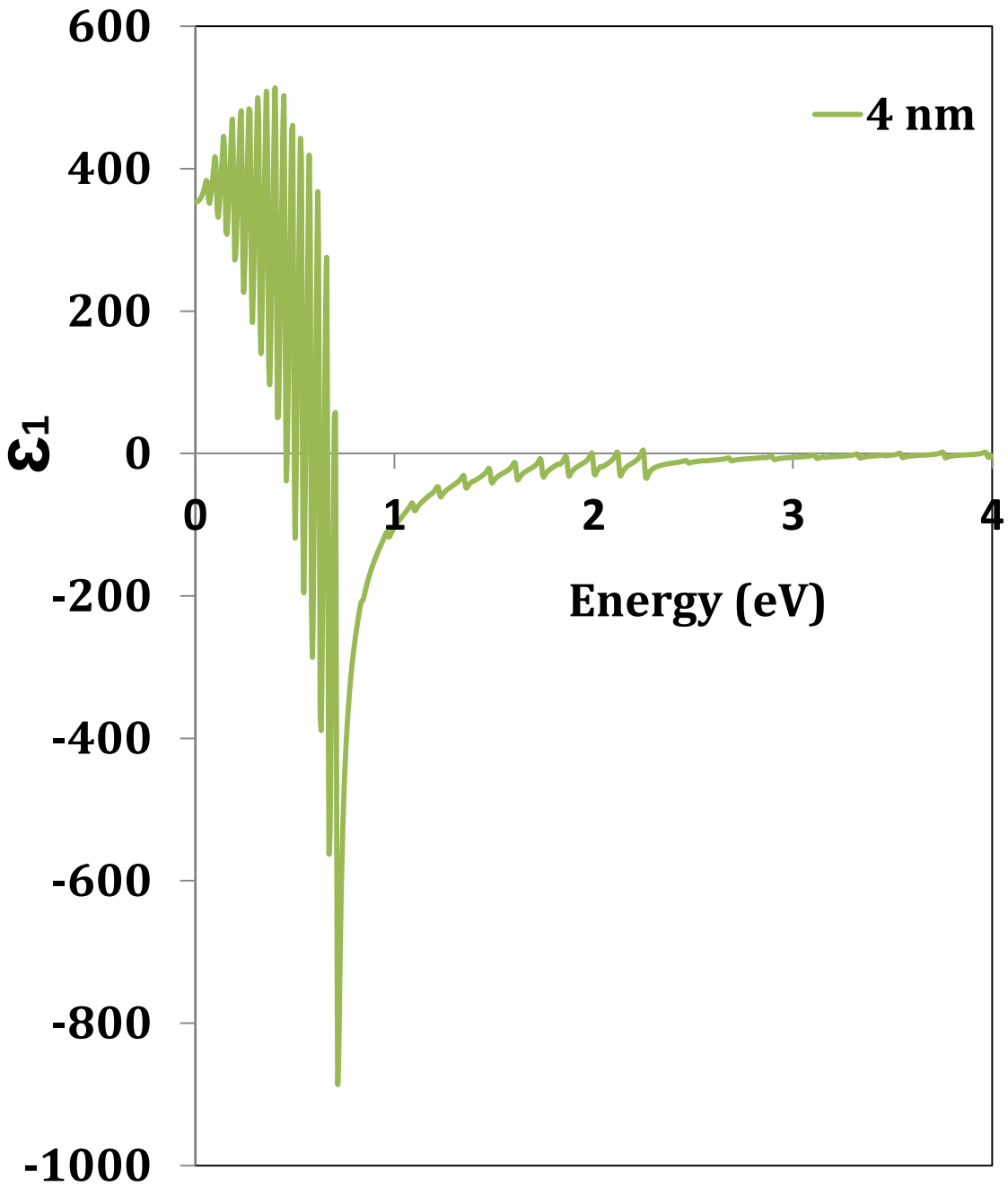

Figure 2.2.b. Real component of dielectric function of silver nanoparticle of 4 nm size as function of excitation energy calculated using the quantum model.

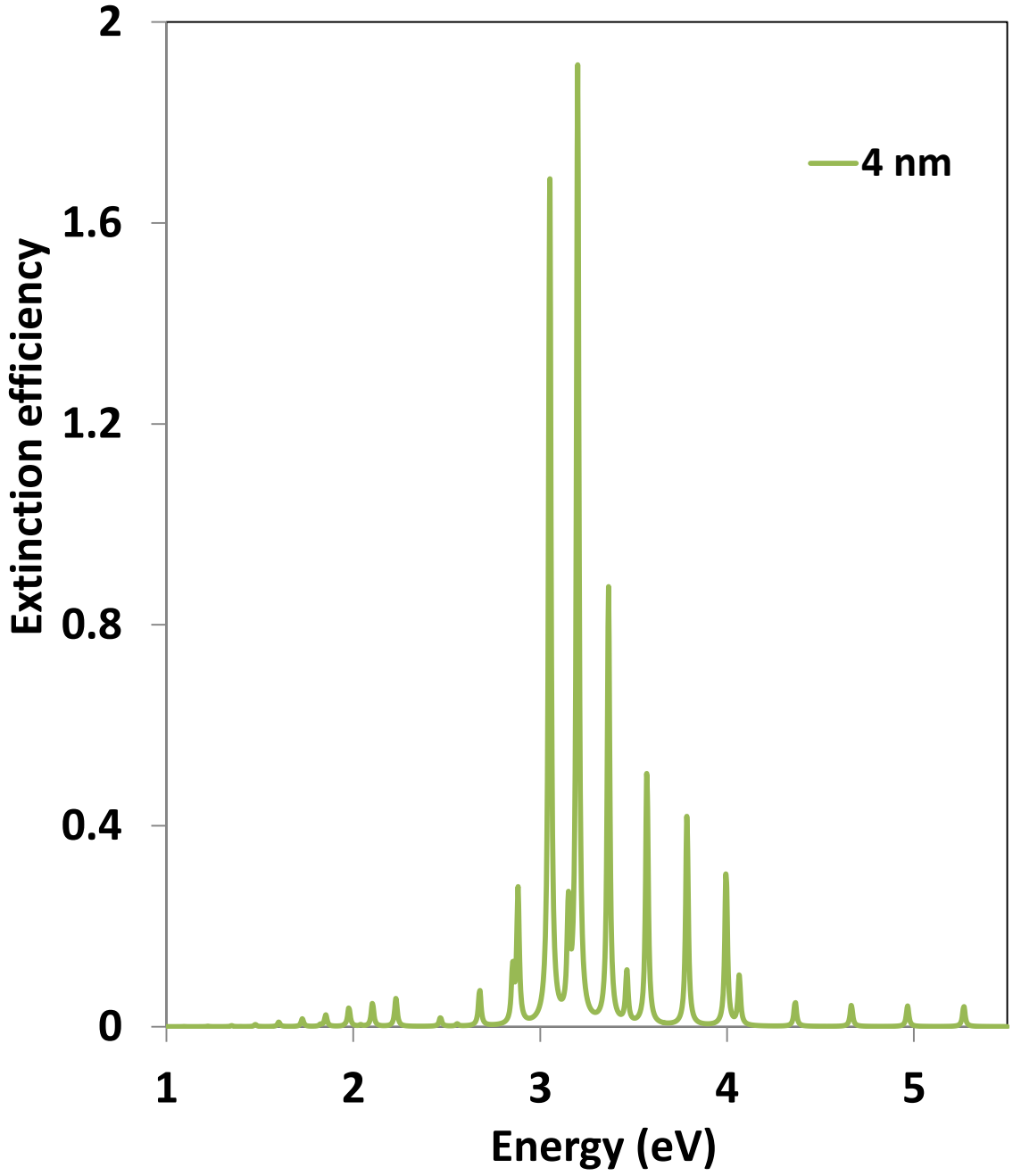

Figure 2.2.c. Extinction efficiency of silver nanoparticle of 4 nm as function of excitation energy calculated using the quantum model.

2.4. Surface plasmon resonance (SPR)

It can be predicted from equation (10) that the extinction peak i.e., the maximum value in the plot of extinction coefficient as function of excitation energy corresponding to surface plasmon resonance frequency will happen when the denominator in the equation is minimum.[2] The denominator in equation (10) has three factors- real and imaginary components of the dielectric function of the metal nanoparticle and the dielectric constant of the medium. To investigate the condition that determines the surface plasmon resonance frequency in plasmonic metal nanoparticles, we have done more analyses by comparing the values of real and imaginary components of the dielectric functions of the silver nanoparticle, dielectric constant of the medium (e.g., glass), and values of extinction coefficients of silver nanoparticle near surface plasmon resonance frequency. The simulated values of extinction coefficient, imaginary and real components of dielectric function as function of excitation energy, and real component of dielectric function near the surface plasmon resonance energy for 32 nm silver particle are shown in Figures 2.3.a-2.3.d, respectively. Figure 2.3.a. shows that the simulated value of surface plasmon resonance energy for 32 nm silver particle (128x128x128 electrons in a box) is ~3.1 eV. The values of imaginary components in Figure 2.3.b show the positive values for imaginary component of dielectric function at all excitation energies. It can also be seen from Figure 2.3.b that the value of imaginary component of dielectric function at surface plasmon resonance energy (3.1 eV) is very low (~0.1). However, the value of real component of the dielectric function is negative at surface plasmon resonance energy as can be seen from Figure 2.3.d. The

value of dielectric constant of the medium (multiplied by -2) is also plotted in Figure 2.3.d for comparison.

It can be clearly seen from Figure 2.3.d that at surface plasmon resonance energy (~3.1 eV), the real component of the dielectric function is equal to the value of dielectric constant of the medium multiplied by -2 (i.e., $\varepsilon_1=-2\varepsilon_m$). Thus, from Figures 2.3.a-2.3.d, it is clear that the value of real component of the dielectric function of the metal nanoparticle and dielectric constant of the medium mainly determine the surface plasmon resonance position. For noble metal nanoparticles (Cu, Ag and Au), this surface plasmon resonance condition, i.e., low and positive value of imaginary component of dielectric function and negative value of real component of dielectric function happens in the visible light range.[2]

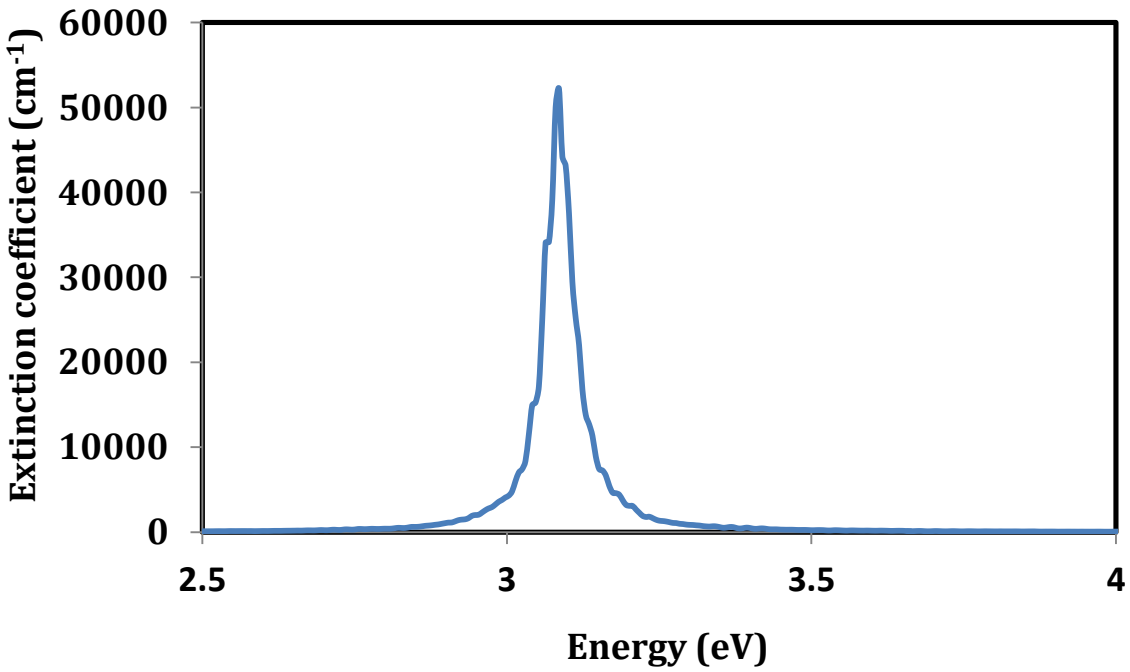

Figure 2.3.a. Extinction coefficient of silver nanoparticle of 32 nm size as function of excitation energy calculated using the quantum model.

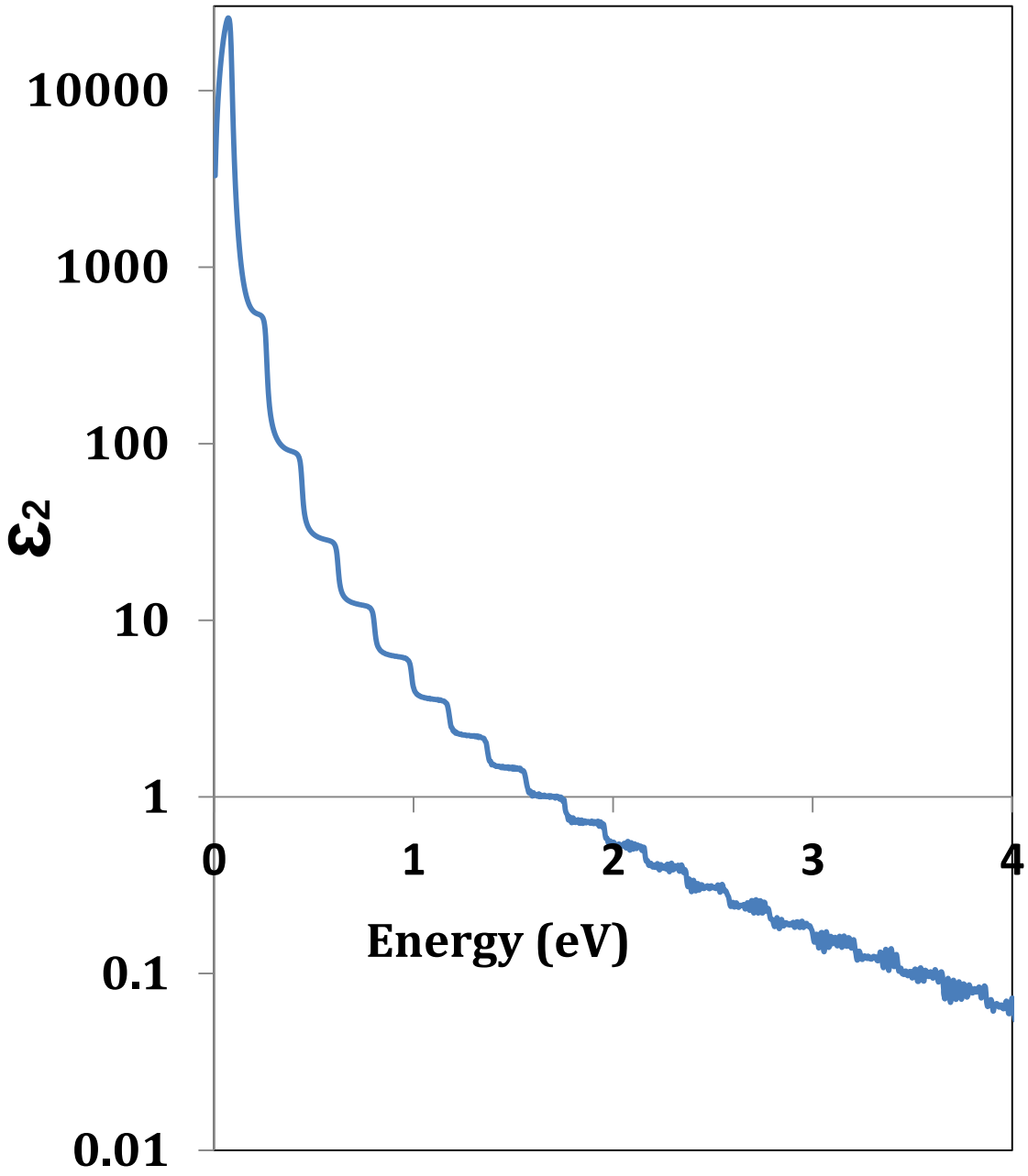

Figure 2.3.b. Imaginary component of dielectric function of silver nanoparticle of 32 nm size as function of excitation energy calculated using the quantum model.

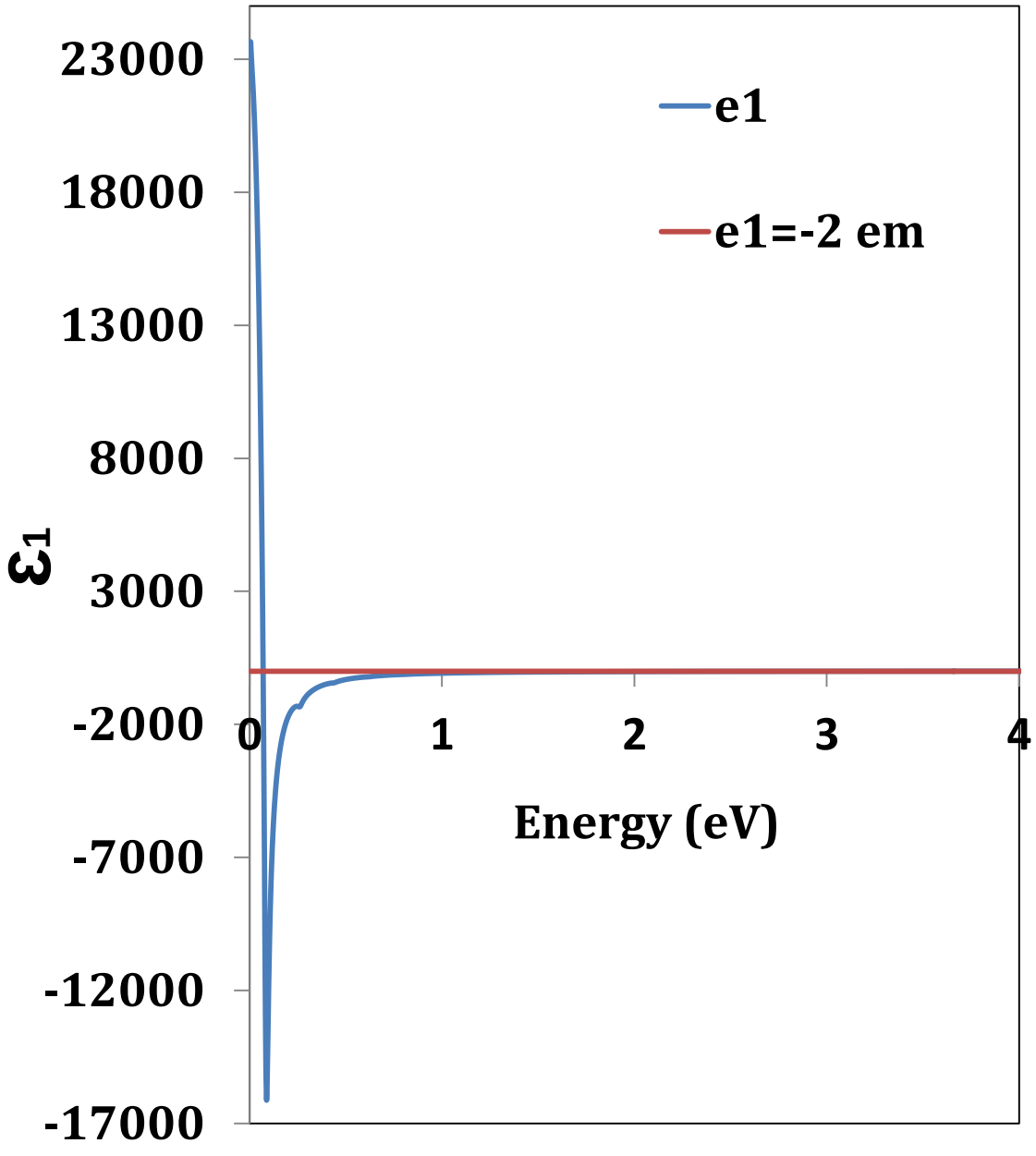

Figure 2.3.c. Real component of dielectric function of silver nanoparticle of 32 nm size as function of excitation energy calculated using the quantum model. The value of dielectric constant of the medium (glass) multiplied by -2 is also included in the figure.

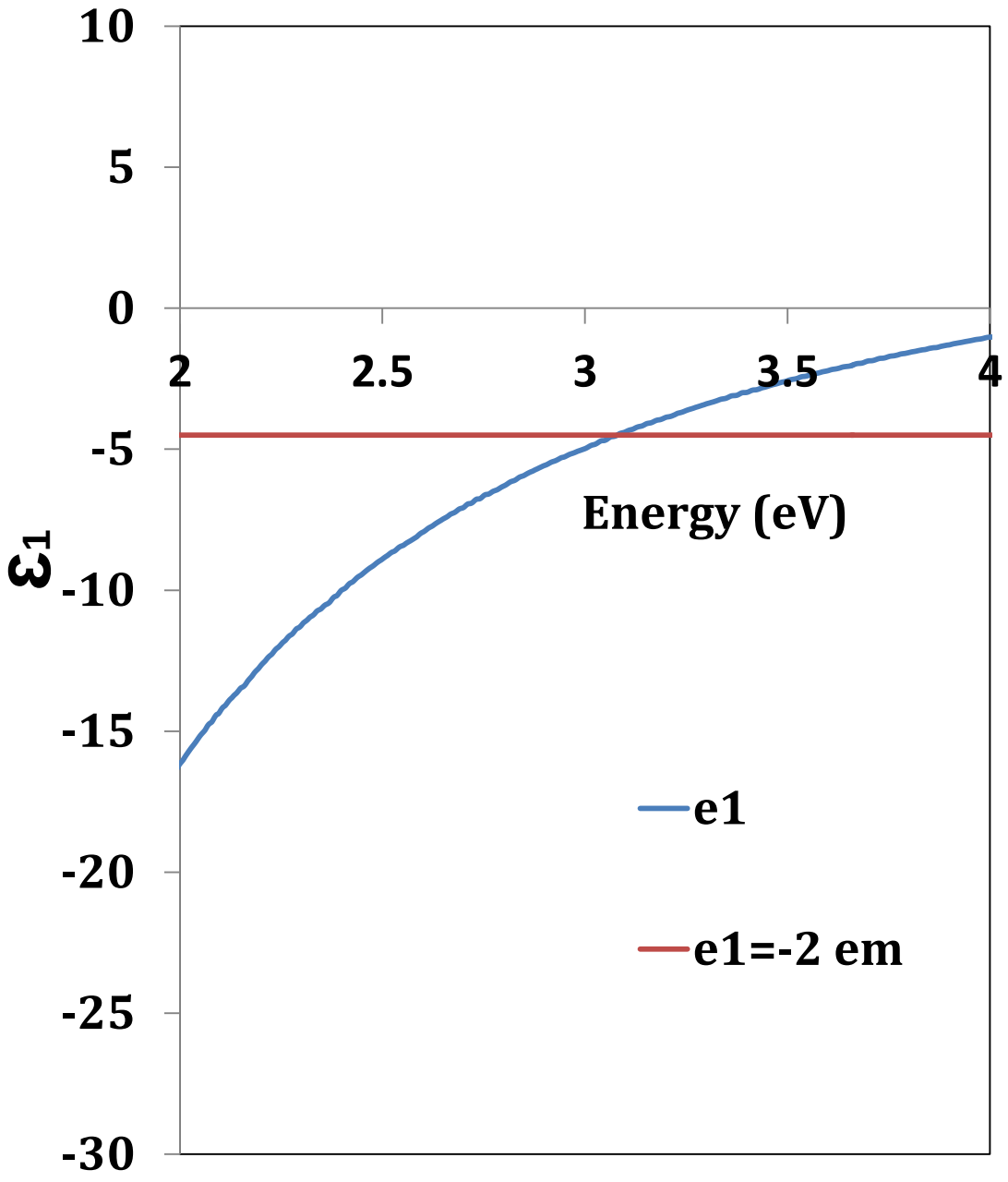

Figure 2.3.d. Real component of dielectric function of silver nanoparticle of 32 nm size near surface plasmon resonance as function of excitation energy calculated using the quantum model. The value of dielectric constant of the medium (glass) multiplied by -2 is also included in the figure.

2.5. SP: Collection of low energy electrons or high energy electron

To investigate the quantum mechanical nature of surface plasmon, the simulations were performed by including only the contributions of (i) low energy electrons, and (ii) high energy electrons, to the real and imaginary components of the dielectric function. The values of imaginary and real components of dielectric functions as function of excitation energy, and the real component of dielectric function near surface plasmon resonance energy calculated by including only the contributions of low energy electrons (<0.8 eV, only up to $\Delta l=9$ dipole transitions) for 32 nm silver particle are shown in Figures 2.4.a-2.4.c, respectively. Figures 2.4.a-2.4.c show that these values of imaginary and real components of dielectric function near surface plasmon resonance energy are similar to the values calculated from the simulations (see Figures 2.3.b-2.3.d) in which contributions of both low energy and high energy electrons are included. These results indicate that the contributions of high energy electrons are not significant to the values of real and imaginary components of the dielectric function. It can also be seen from Figures 2.4.a-2.4.c that the resonance condition (i.e., $\varepsilon_1=-2\varepsilon_m$) is still achieved near surface plasmon resonance energy when only contributions of the low energy excited electrons are included. However, it can be seen from Figures 2.5.a and 2.5.b that when only the contributions of high energy electrons (>0.8 eV, dipole transitions with $\Delta l>9$) are included, the values of real and imaginary components of the dielectric function do not meet the surface plasmon resonance condition, i.e., low and positive value of imaginary component of dielectric function and negative value of real component of dielectric function that matches the dielectric constant of the medium ($\varepsilon_1=-2\varepsilon_m$).

It is also worth noting that the denominator in equation (10) does not go through minimum when only the contributions of high energy electrons are included because both real and imaginary components of the dielectric function are positive values at all excitation energies (see Figures 2.5.a and 2.5.b), which indicates that surface plasmon resonance condition can not be achieved. From Figures 2.3-2.5, it can be concluded that the low energy excited electrons contribute mainly to the real and imaginary components of the dielectric functions, which determine the surface plasmon resonance in plasmonic metal nanoparticles. These results confirm that surface plasmon is a quasi-particle, which is the collection of low energy excited electrons around the Fermi level of the metal nanoparticle.

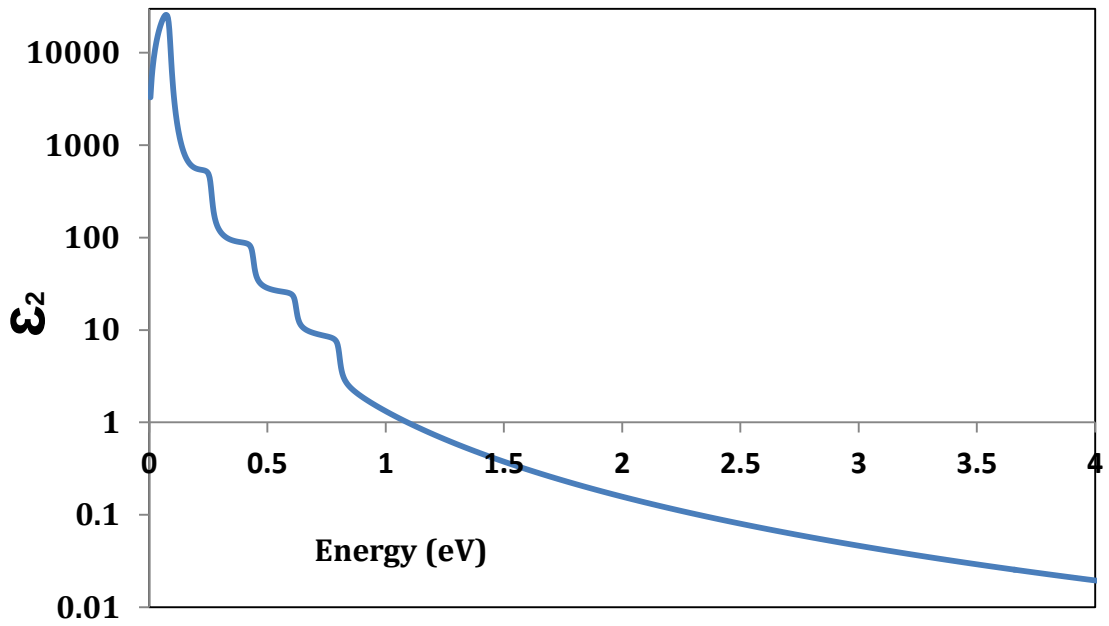

Figure 2.4.a. Imaginary component of dielectric function of silver nanoparticle of 32 nm size as function of excitation energy with only low energy excited electrons contribution included in the quantum model. Only the contributions from low energy excited electrons (<0.8 eV, only up to Δl=9 dipole transitions) are included in the simulation.

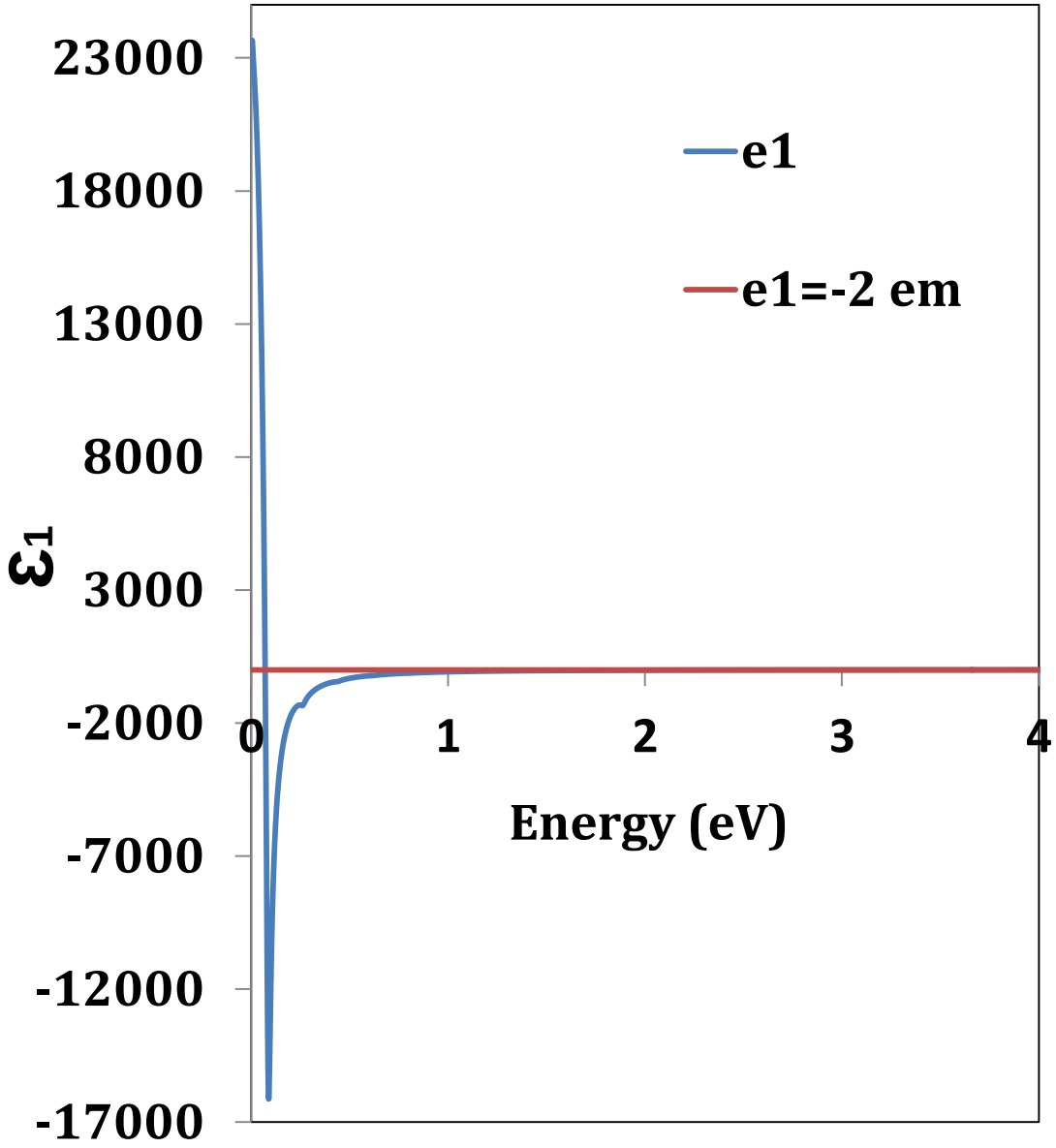

Figure 2.4.b. Real component of dielectric function of silver nanoparticle of 32 nm size as function of excitation energy with only low energy excited electrons contribution included in the quantum model. Only the contributions from low energy excited electrons (<0.8 eV, only up to Δl=9 dipole transitions) are included in the simulation.

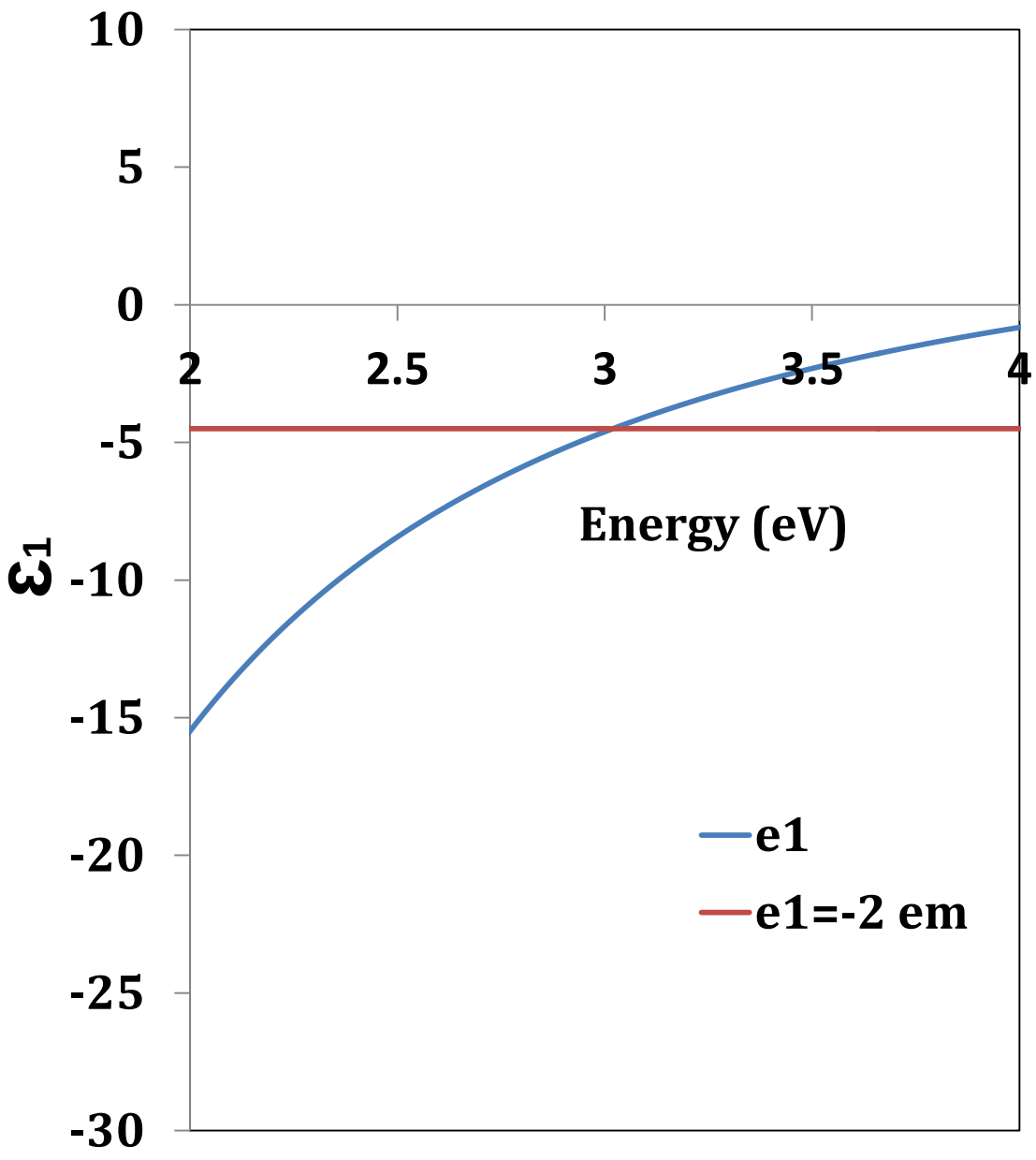

Figure 2.4.c. Real component of dielectric function of silver nanoparticle of 32 nm size near surface plasmon resonance as function of excitation energy with only low energy excited electrons contribution included in the quantum model. Only the contributions from low energy excited electrons (<0.8 eV, only up to Δl=9 dipole transitions) are included in the simulation.

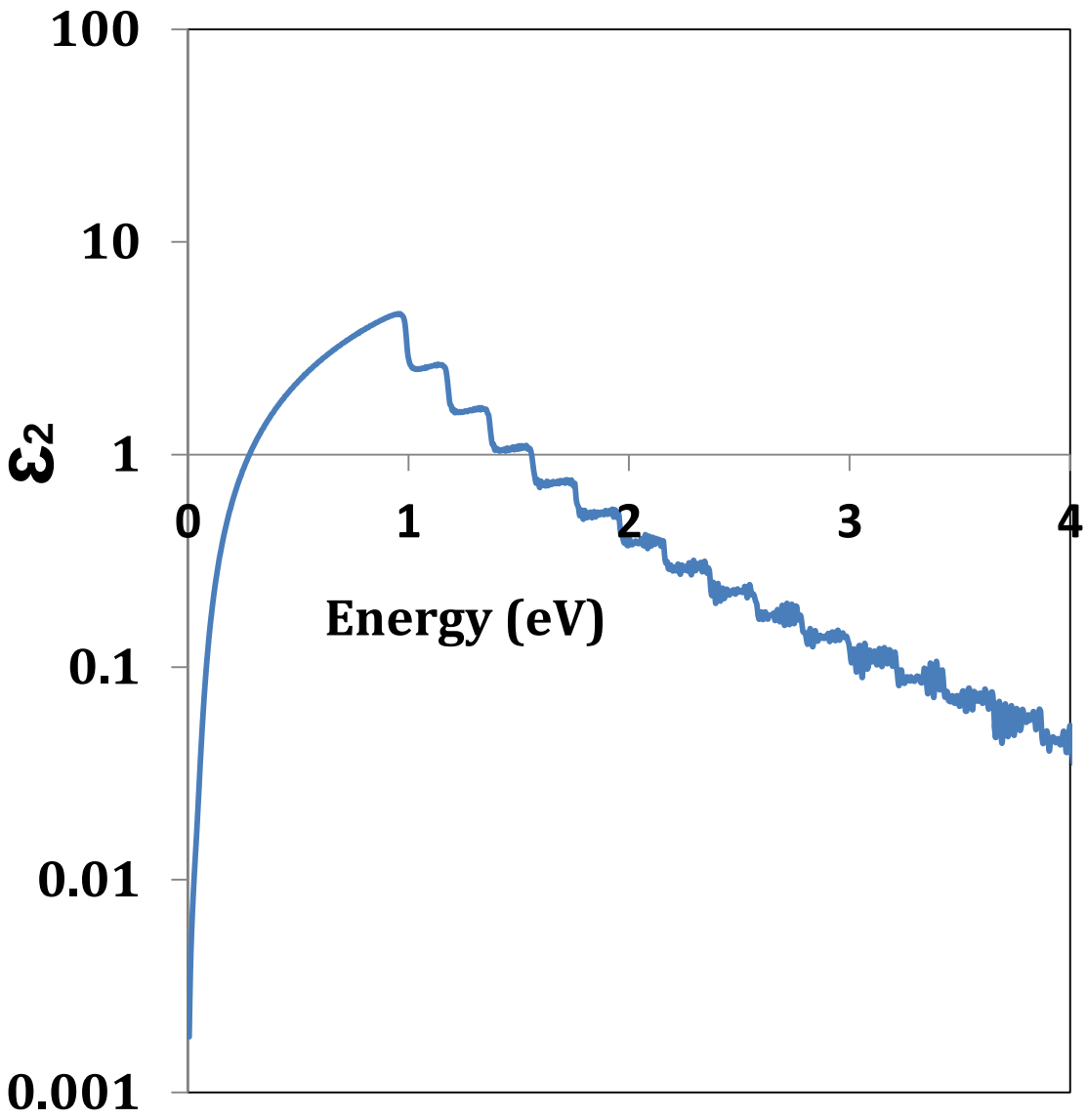

Figure 2.5.a. Imaginary component of dielectric function of silver nanoparticle of 32 nm size as function of excitation energy with only high energy excited electrons contribution included in the quantum model. Only the contributions from high energy excited electrons (>0.8 eV, dipole transitions with $\Delta l>9$) are included in the simulation.

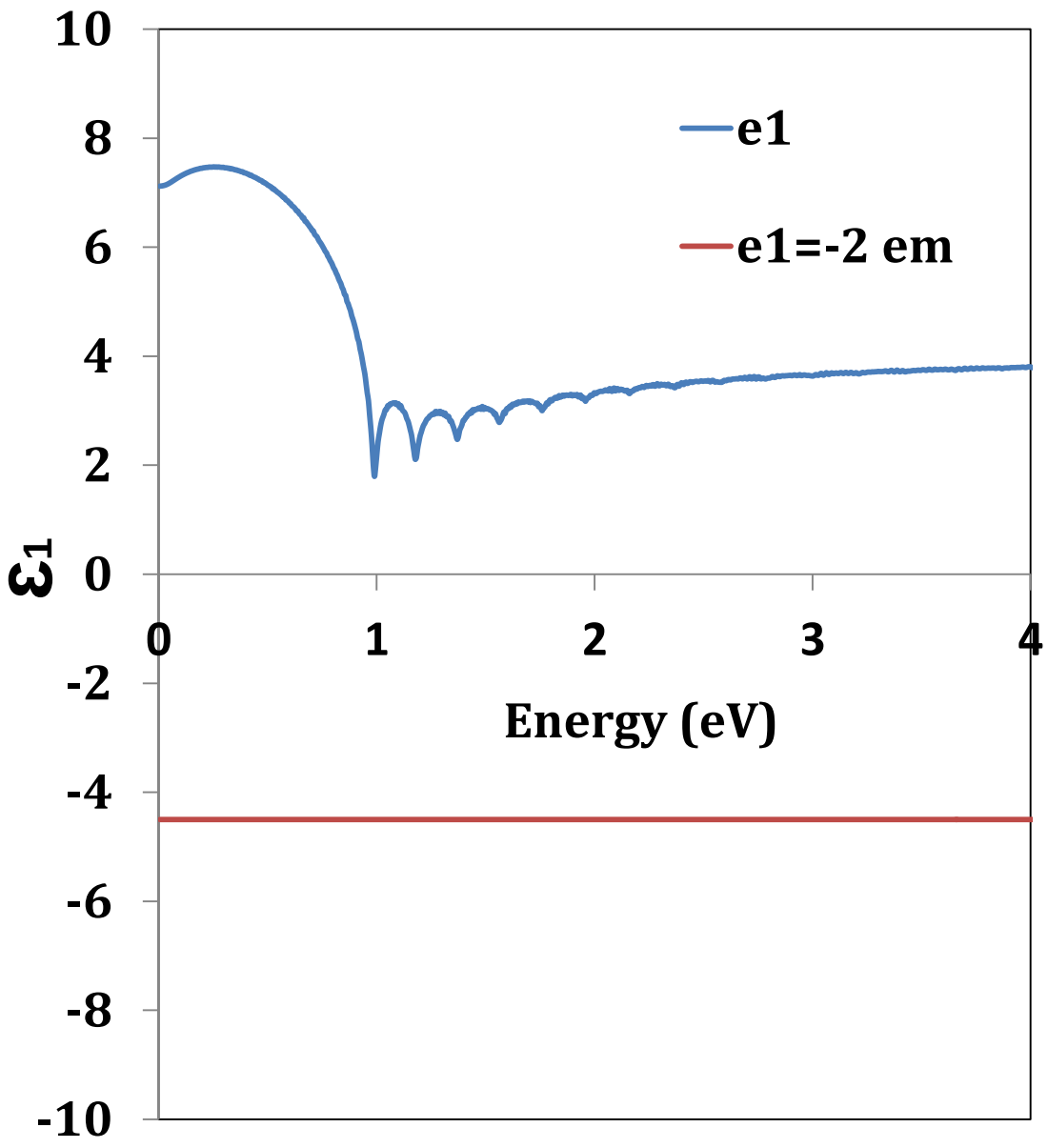

Figure 2.5.b. Real component of dielectric function of silver nanoparticle of 32 nm size as function of excitation energy with only high energy excited electrons contribution included in the quantum model. Only the contributions from high energy excited electrons (>0.8 eV, dipole transitions with $\Delta l>9$) are included in the simulation.

2.6. Size-dependent optical properties

To investigate how the optical properties of plasmonic metal nanoparticle vary with size, we performed simulations for different sizes (2 to 60 nm) of silver nanoparticles. The real and imaginary components of dielectric functions, and the extinction efficiency (ratio of extinction cross section to geometric cross section) of silver nanoparticles of different sizes calculated using the quantum mechanical model are shown in Figures 2.6-2.8, respectively. It is worth mentioning here that energy in the x-axis is scaled with respect to Fermi level of the silver (i.e., zero in x-axis correspond to E_F) in these figures. Figures 2.6 and 2.7 show that the low energy excited electrons mainly dominate the real and imaginary components of the dielectric function for all sizes of the silver nanoparticles. Figure 2.8 shows that the extinction efficiency increases with increasing particle size. This trend is expected because the extinction cross section is proportional to the volume of the particle (see equation 11) and thus number of conduction electrons in the particle.

It can be seen from Figures 2.6 and 2.7 that the peak in the plot of real and imaginary components of dielectric function as function of energy shifts towards low energy with increasing particle size. This trend indicates that the excitation energy (e.g., photon energy) used to excite surface plasmon is distributed among the excited electrons present in surface plasmon. Since the number of electrons increases with increasing particle size the energy gain by an electron becomes less for excited electrons present in the surface plasmon of larger particle compared to smaller particle. These results also indicate that the excited electrons present in the

surface plasmon of large particles can have only very low energy. For example the excited electrons present in surface plasmon of 60 nm silver particle can have only energy less than 0.1 eV as can be seen from Figures 2.6.b and 2.7.b. However, the hot electron created by the decay of surface plasmon through Landau damping can have the same energy as the surface plasmon energy (~3.1 eV) in silver nanoparticles.[4–10] Different possible decay mechanisms of surface plasmons and their dynamics are explained in greater detail in section 2.7.

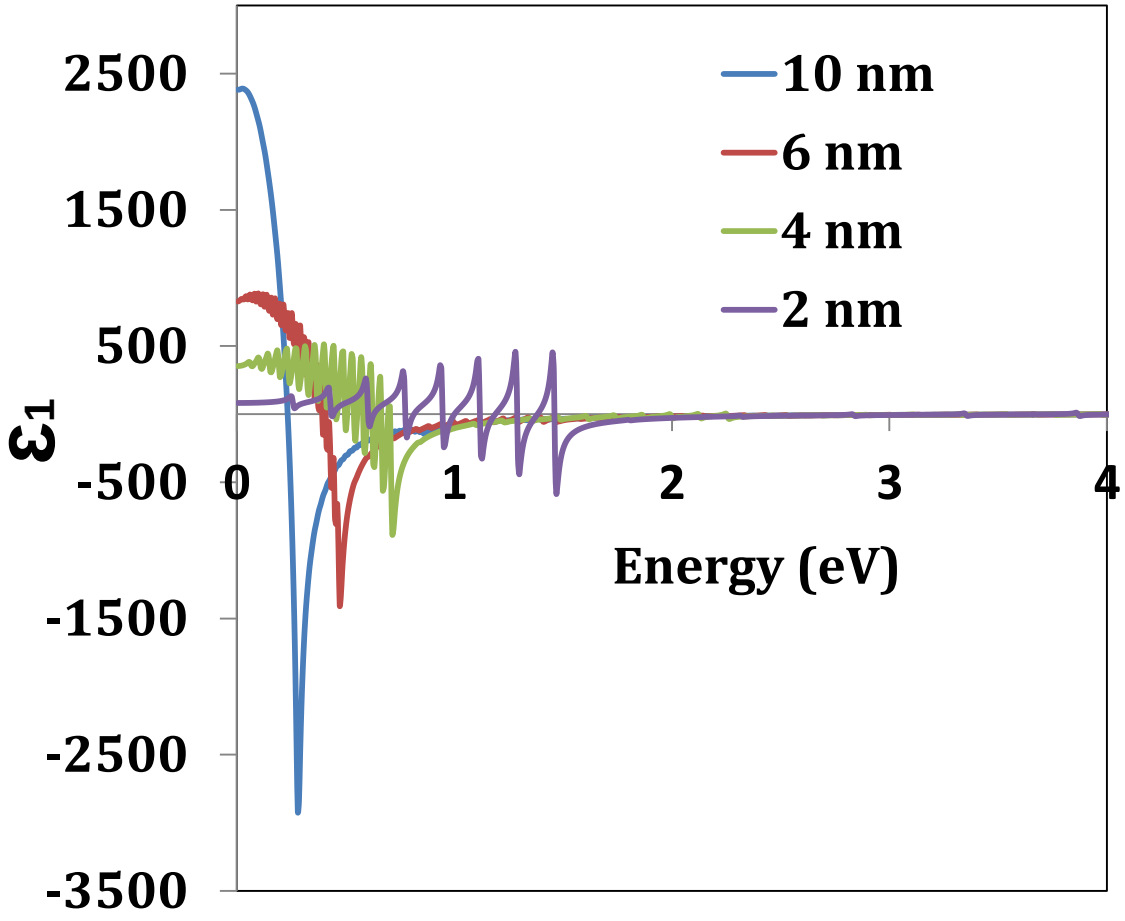

Figure 2.6.a. Real components of dielectric functions of silver nanoparticles of different sizes (2 to 10 nm) calculated using the quantum model. Figure legends show the diameters of the silver nanoparticles.

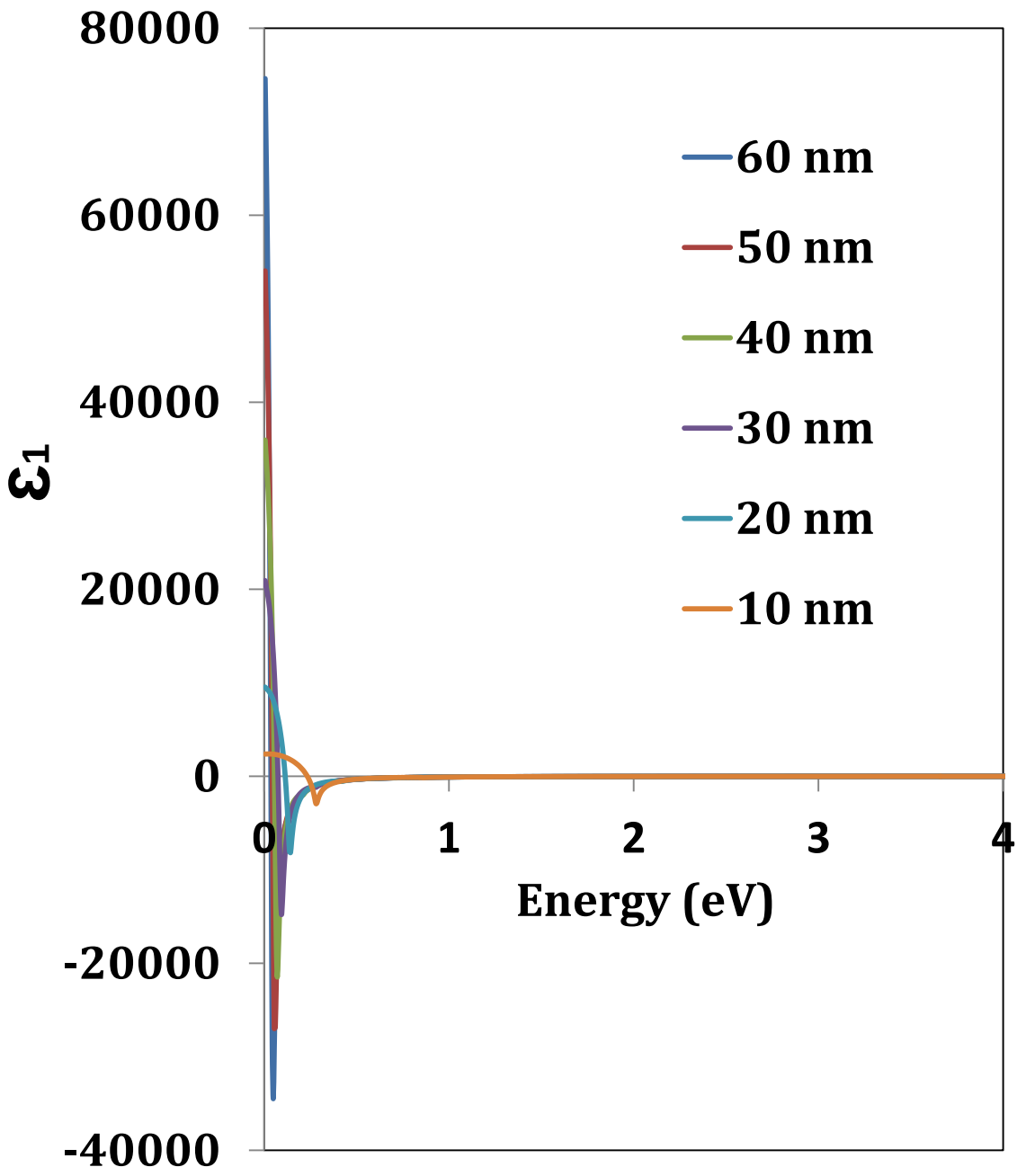

Figure 2.6.b. Real components of dielectric functions of silver nanoparticles of different sizes (10 to 60 nm) calculated using the quantum model. Figure legends show the diameters of the silver nanoparticles.

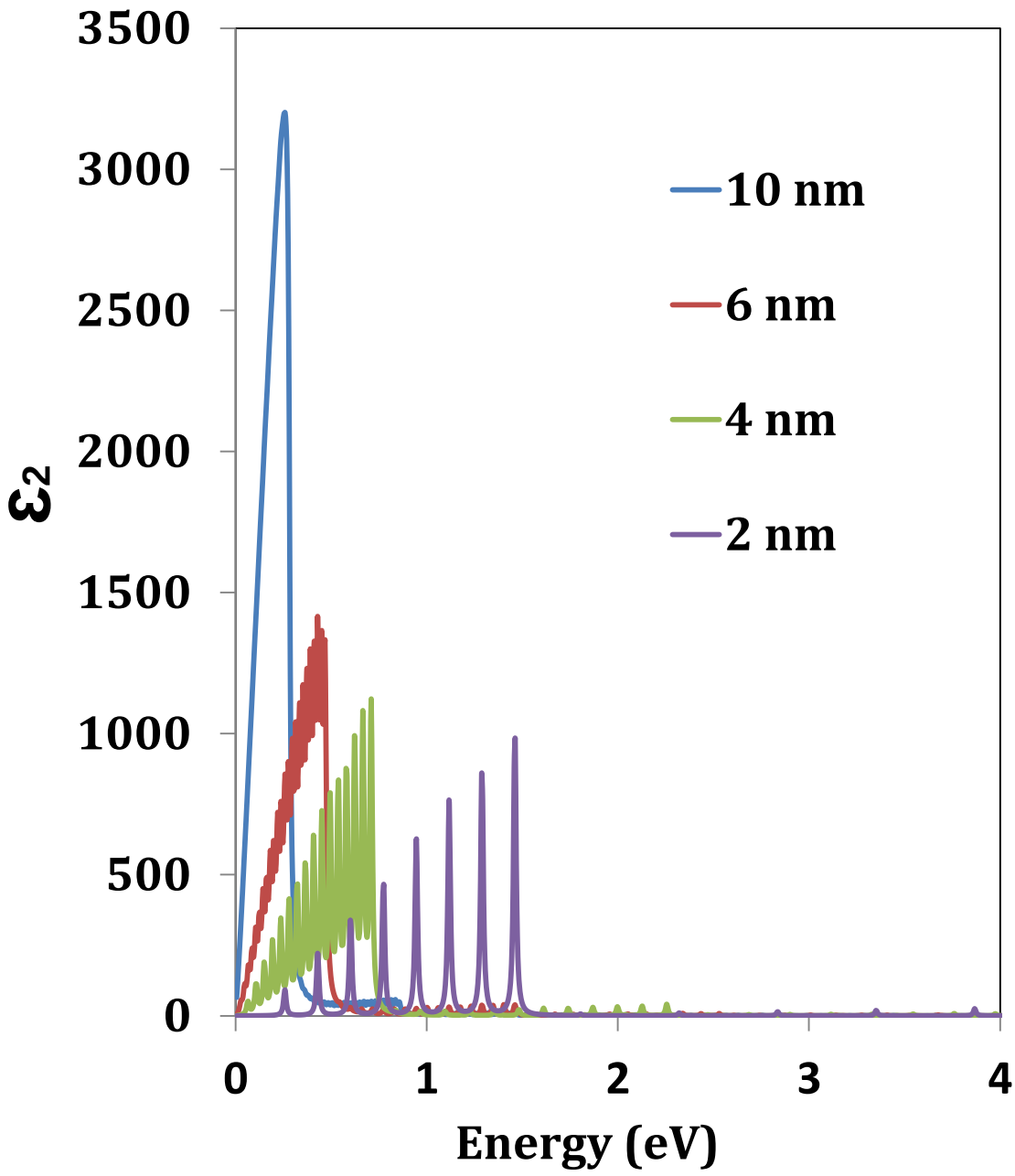

Figure 2.7.a. Imaginary components of dielectric functions of silver nanoparticles of different sizes (2 to 10 nm) calculated using the quantum model. Figure legends show the diameters of the silver nanoparticles.

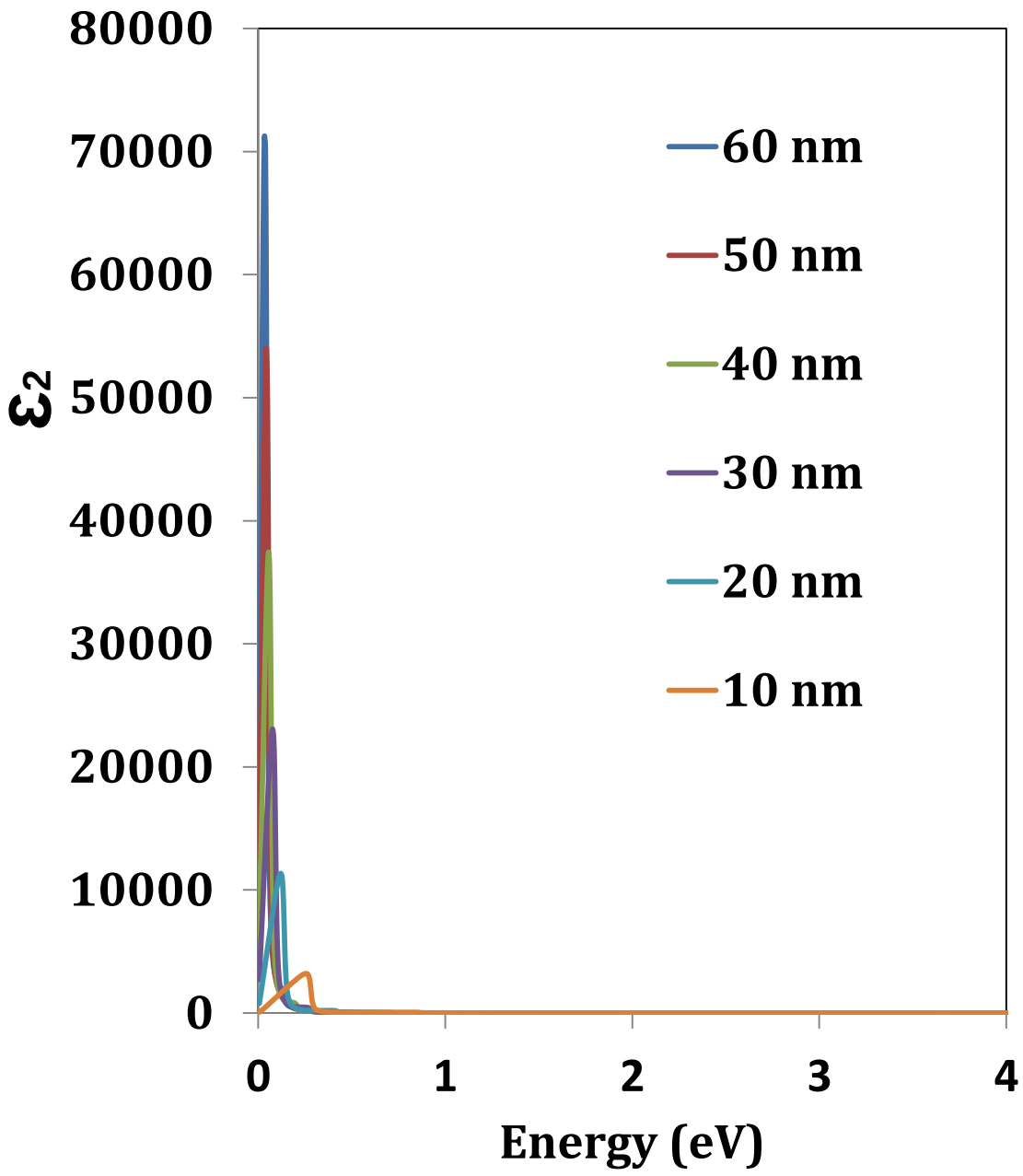

Figure 2.7.b. Imaginary components of dielectric functions of silver nanoparticles of different sizes (10 to 60 nm) calculated using the quantum model. Figure legends show the diameters of the silver nanoparticles.

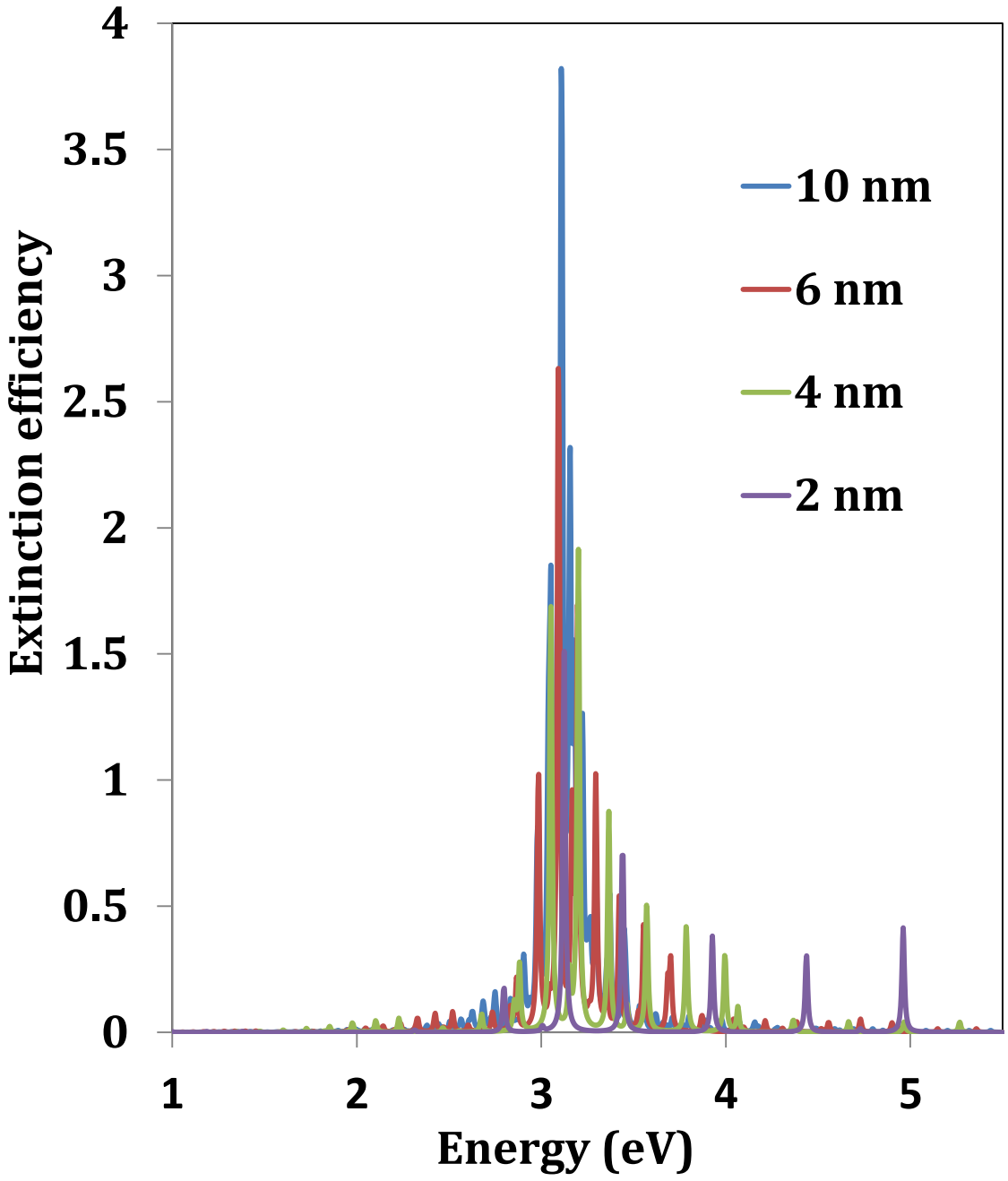

Figure 2.8.a. Extinction efficiency of silver nanoparticles of different sizes (2 to 10 nm) calculated using the quantum model. Figure legends show the diameters of the silver nanoparticles.

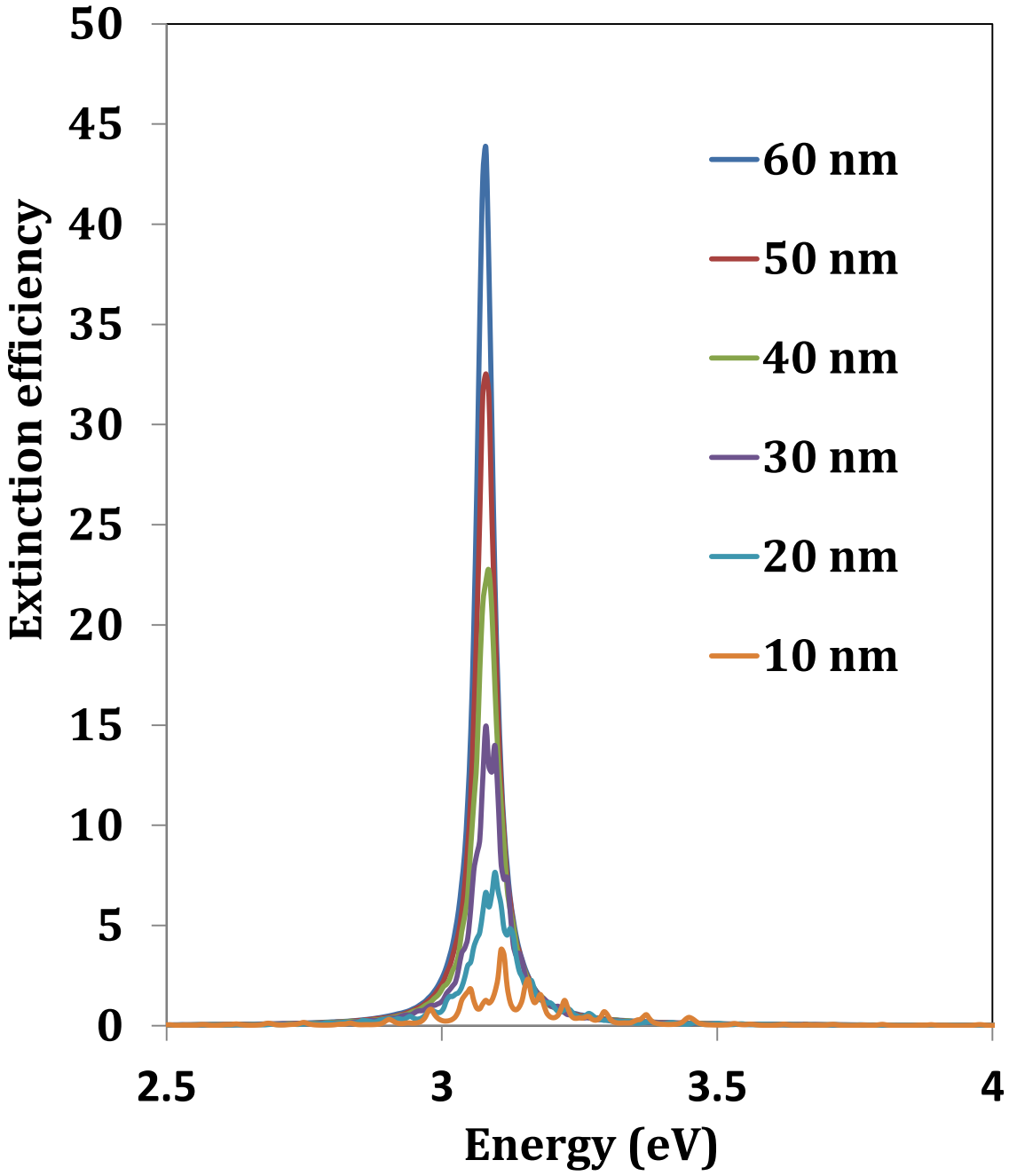

Figure 2.8.b. Extinction efficiency of silver nanoparticles of different sizes (10 to 60 nm) calculated using the quantum model. Figure legends show the diameters of the silver nanoparticles.

2.7. Relaxation of surface plasmon

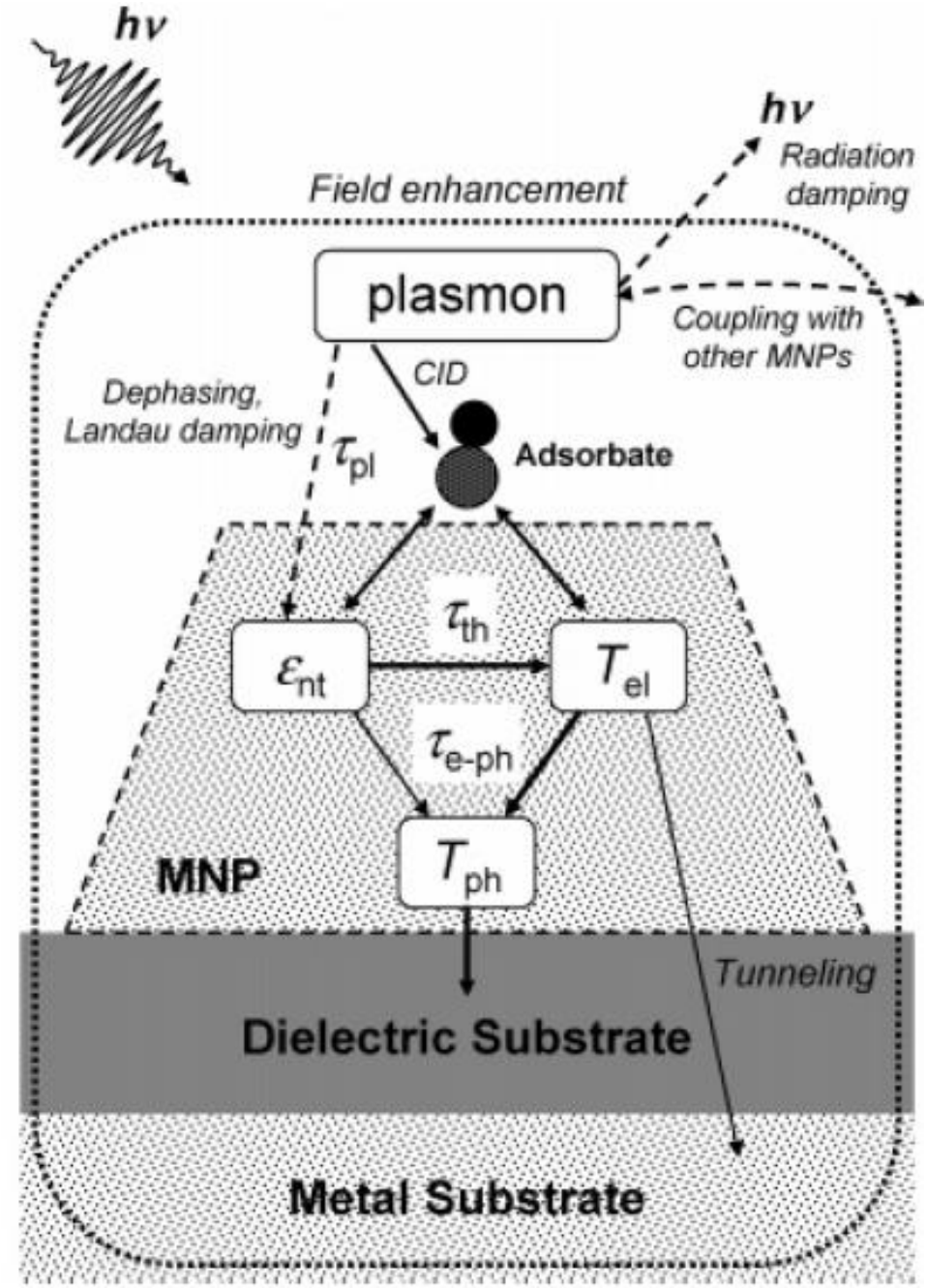

Figure 2.9. Schematic representation of ralxation of surface plasmon in metal nanoparticle (MNP). Taken from Watanabe et al.[4]

The surface plasmon excited in the metal nanoparticle can relax through different mechanisms after the short life time of ~10 femtoseconds (fs).[4,11–14] Different possible mechanisms of decay of surface plasmon are shown schematically in Figure 2.9. As mentioned above since the surface plasmon is the collection of low energy excited electrons, it can decay through relaxation of these low energy excited electrons into the ground state with the simultaneous emission of a photon (radiation damping or scattering) or creation of a hot electron through Landau damping.[2,4] The low energy excited electrons in the surface plasmon can also decay through chemical interface damping (CID), which involves the inelastic scattering of these clusters of low energy electrons in the surface plasmon with the surrounding medium such as adsorbate.[2]

The non-thermal hot electrons created through Landau damping of surface plasmon in the metal nanoparticle can undergo electron-electron scattering with time scale in the range of 10-100 fs to produce thermalized electrons.[4] The thermalized electrons with quasi-thermal distribution can couple to the lattice of the metal nanoparticle through electron-phonon interactions in the time scale of tens of hundreds of picoseconds (ps).[4] These electrons-phonons interactions mainly result in the local heating in the metal nanoparticle. If the primary hot electrons formed through Landau damping or the thermalized electrons formed after electron-electron scattering match the energy of adsorbate negative ion resonance, they can be transiently transferred to the adsorbate.[4]

The decay of surface plasmons into intense scattering of the photons mainly contributes to the highly confined electromagnetic fields near the surface of plasmonic metal nanoparticles. This unique ability of plasmonic metal nanoparticles to confine electromagnetic fields can be used in various types of sensors that are based on surface-enhanced Raman and fluorescence spectroscopies for medical and biological applications,[15,16] and in solar cells.[11,17–19] The capacity of plasmonic nanoparticles to convert incident light into surface plasmon mediated local heating has been used in light-induced selective tissue targeting[20–22] and light enhanced catalytic reactions.[23–25] The surface plasmon mediated transient transfer of clusters of low energy excited electrons (via CID) or non-thermalized or thermalized electrons (formed through Landau damping) to the adsorbate can result in electron-driven catalytic chemistry on the surface of plasmonic metal nanoparticles.[26–29]

2.8. Conclusions

We have demonstrated that the quantum model based on electrons in a box can be used to simulate the optical properties of plasmonic metal nanoparticles. The simulation results show that surface plasmon is a collection of low energy excited electrons with the energy around the Fermi level of the metal nanoparticle. The model shows that the surface plasmon resonance happens when the real component of the dielectric function is negative and equal to the value of dielectric constant of the medium multiplied by 2 (i.e., $\varepsilon_1=-2\varepsilon_m$). The model also shows that an excited electron present in the surface plasmon of large particle has low energy compared to the energy of an excited electron in small particle.

2.9. References

(1) Genzel, L.; Martin, T. P.; Kreibig, U. Dielectric function and plasma resonances of small metal particles. Zeitschrift Physik B Condensed Matter and Quanta 1975, 21, 339–346.

(2) Kreibig, U.; Vollmer, M. Optical properties of metal clusters; Springer: Berlin; New York, 1995.

(3) Lu, X.; Rycenga, M.; Skrabalak, S. E.; Wiley, B.; Xia, Y. Chemical Synthesis of Novel Plasmonic Nanoparticles. Annual Review of Physical Chemistry 2009, 60, 167–192.

(4) Watanabe, K.; Menzel, D.; Nilius, N.; Freund, H.-J. Photochemistry on Metal Nanoparticles. Chem. Rev. 2006, 106, 4301–4320.

(5) Michaels, A. M.; Jiang; Brus, L. Ag Nanocrystal Junctions as the Site for Surface-Enhanced Raman Scattering of Single Rhodamine 6G Molecules. J. Phys. Chem. B 2000, 104, 11965–11971.

(6) Brus, L. Noble Metal Nanocrystals: Plasmon Electron Transfer Photochemistry and Single-Molecule Raman Spectroscopy. Acc. Chem. Res. 2008, 41, 1742–1749.

(7) Al-Shamery, K. Photochemistry at nanoparticulate surfaces. Journal of Physics Condensed Matter 2006, 18, 1581.

(8) Zhou, X.-L.; Zhu, X.-Y.; White, J. M. Photochemistry at adsorbate/metal interfaces. Surface Science Reports 1991, 13, 73–220.

(9) Zimmermann, F. M.; Ho, W. State resolved studies of photochemical dynamics at surfaces. Surface Science Reports 1995, 22, 127–247.

(10) Dai, H.-L. Laser Spectroscopy and Photochemistry on Metal Surfaces, Part 1; Dai, H.-L.; Ho, W., Eds.; World Scientific Pub Co Inc, 1995.

(11) Schuller, J. A.; Barnard, E. S.; Cai, W.; Jun, Y. C.; White, J. S.; Brongersma, M. L. Plasmonics for extreme light concentration and manipulation. Nat Mater 2010, 9, 193–204.

(12) Jain, P. K.; Huang, X.; El-Sayed, I. H.; El-Sayed, M. A. Review of Some Interesting Surface Plasmon Resonance-enhanced Properties of Noble Metal Nanoparticles and Their Applications to Biosystems. Plasmonics 2007, 2, 107–118.

(13) El-Sayed, M. A. Some Interesting Properties of Metals Confined in Time and Nanometer Space of Different Shapes. Acc. Chem. Res. 2001, 34, 257–264.

(14) Link, S.; El-Sayed, M. A. Optical properties and ultrafast dynamics of metallic nanocrystals. Annu Rev Phys Chem 2003, 54, 331–366.

(15) McDonagh, C.; Burke, C. S.; MacCraith, B. D. Optical Chemical Sensors. Chem. Rev. 2008, 108, 400–422.

(16) Anker, J. N.; Hall, W. P.; Lyandres, O.; Shah, N. C.; Zhao, J.; Van Duyne, R. P. Biosensing with plasmonic nanosensors. Nat Mater 2008, 7, 442–453.

(17) Atwater, H. A.; Polman, A. Plasmonics for improved photovoltaic devices. Nat Mater 2010, 9, 205–213.

(18) Hou, W.; Pavaskar, P.; Liu, Z.; Theiss, J.; Aykol, M.; Cronin, S. B. Plasmon resonant enhancement of dye sensitized solar cells. Energy Environ. Sci. 2011, 4, 4650–4655.

(19) Pala, R. A.; White, J.; Barnard, E.; Liu, J.; Brongersma, M. L. Design of Plasmonic Thin-Film Solar Cells with Broadband Absorption Enhancements. Advanced Materials 2009, 21, 3504–3509.

(20) Dykman, L.; Khlebtsov, N. Gold nanoparticles in biomedical applications: recent advances and perspectives. Chem. Soc. Rev. 2012, 41, 2256–2282.

(21) Hirsch, L. R.; Stafford, R. J.; Bankson, J. A.; Sershen, S. R.; Rivera, B.; Price, R. E.; Hazle, J. D.; Halas, N. J.; West, J. L. Nanoshell-mediated near-infrared thermal therapy of tumors under magnetic resonance guidance. PNAS 2003, 100, 13549–13554.

(22) El-Sayed, I. H.; Huang, X.; El-Sayed, M. A. Selective laser photo-thermal therapy of epithelial carcinoma using anti-EGFR antibody conjugated gold nanoparticles. Cancer Letters 2006, 239, 129–135.

(23) Hung, W. H.; Aykol, M.; Valley, D.; Hou, W.; Cronin, S. B. Plasmon Resonant Enhancement of Carbon Monoxide Catalysis. Nano Lett. 2010, 10, 1314–1318.

(24) Adleman, J. R.; Boyd, D. A.; Goodwin, D. G.; Psaltis, D. Heterogenous Catalysis Mediated by Plasmon Heating. Nano Lett. 2009, 9, 4417–4423.

(25) Fasciani, C.; Alejo, C. J. B.; Grenier, M.; Netto-Ferreira, J. C.; Scaiano, J. C. High-Temperature Organic Reactions at Room Temperature Using Plasmon Excitation: Decomposition of Dicumyl Peroxide. Org. Lett. 2011, 13, 204–207.

(26) Christopher, P.; Xin, H.; Marimuthu, A.; Linic, S. Singular characteristics and unique chemical bond activation mechanisms of photocatalytic reactions on plasmonic nanostructures. Nat. Mater. 2012, 11, 1044-1050.

(27) Christopher, P.; Xin, H.; Linic, S. Visible-light-enhanced catalytic oxidation reactions on plasmonic silver nanostructures. Nat. Chem. 2011, 3, 467–472.

(28) Linic, S.; Christopher, P.; Ingram, D. B. Plasmonic-metal nanostructures for efficient conversion of solar to chemical energy. Nat. Mater. 2011, 10, 911–921.

(29) Mukherjee, S.; Libisch, F.; Large, N.; Neumann, O.; Brown, L. V.; Cheng, J.; Lassiter, J. B.; Carter, E. A.; Nordlander, P.; Halas, N. J. Hot Electrons Do the Impossible: Plasmon-Induced Dissociation of H_2 on Au. Nano Lett. 2013, 13, 240–247.

CHAPTER 3

Design of plasmonic platforms for selective molecular sensing based on surface enhanced Raman spectroscopy

3.1. Summary

While high sensitivity of plasmonic metal nanoparticles in Surface enhanced Raman spectroscopy (SERS) is well established, applications of SERS in the selective identification of trace quantities of targeted molecules in a mixture of species remains to be a challenge. In this chapter, we demonstrate the design of plasmonic substrates that selectively enhance specific Raman vibrational bands, thereby offering high molecular sensitivity. We show that by changing the density and shape of plasmonic Ag nanostructures in Ag aggregates we can selectively control their optical properties and the degree to which they enhance different vibrational bands. By correlating the optical extinction spectra of substrates and the enhancement factors for different Raman vibrational bands we demonstrate that the observed difference in the enhancement of vibrational modes is due to the difference in the surface plasmon resonance intensity at the Stokes Raman shifted wavelengths. We also shed light on critical design parameters for the synthesis of plasmonic nanosubstrates for selective detection of a molecule in a mixture of compounds.

3.2. Introduction

Selective detection of a specie in a mixture of compounds is important in a number of applications, including the detection of contaminants and harmful chemicals (like explosives and biological warfare agent) as well as elusive reaction intermediates in mechanistic studies of chemical reactions.[1,2] Viable detection techniques must provide a combination of high sensitivity and molecular selectivity. Surface-enhanced Raman spectroscopy (SERS) over optically excited plasmonic nanostructures is one of the most promising techniques for sensitive and selective molecular identification.[3,4] In SERS, the resonant creation of surface plasmons on metal nanoparticle surfaces results in enhanced Raman signals of many order of magnitude, in some cases even allowing single molecule detection.[5,6] In this chapter, our objective is to design plasmonic substrates that could be used in SERS for the selective identification of trace quantities of targeted species in a mixture of species.

We demonstrate the design of plasmonic nanostructures that can selectively enhance specific Raman vibrational bands in a molecule. In addition to offering high sensitivity, these sensor systems show promise for excellent molecular selectivity based on selective enhancements of specific Raman bands associated with the targeted analyte. Specifically, we show that aggregates of plasmonic Ag nanoparticles of different shapes exhibit different enhancement for different vibrational modes in diphenylacetylene (DPA). By correlating the extinction spectra of substrates and the SERS spectra of the analyte molecule, we propose that the observed difference in the enhancement of vibrational modes is due to the difference in the surface plasmon resonance (SPR) intensity at the Stokes Raman

shifted wavelengths. The current study gives new insights in the design of plasmonic nano-aggregate substrates for the selective molecular species detection.

3.3. Methods

3.3.1. Synthesis of Ag nanoparticles

To prepare tunable plasmonic nanoparticle substrates, three different shapes of silver nanostructures – nanospheres, nanocubes and nanowires with controlled sizes were synthesized using a modified polyol process.[7–13] Silver nitrate, $AgNO_3$ (99%, Sigma), ethylene glycol (E.G, 99%, J.T. Baker), PVP (55,000 MW, Sigma) and HCl (30mM) were used as a precursor, reducing agent and solvent, capping agent, and etching agent, respectively. For a typical synthesis in solution, 5ml of E.G in 20 ml glass vial, which was submerged in heating oil bath on a stirring hot plate, was heated to 140-145 ^{0}C for 1 hr. After 1 hr, 100 μL of 30 mM HCl solution was added, and was allowed for 10 mins for complete mixing. 3 ml each of 0.1M $AgNO_3$ and 0.15M of PVP were injected simultaneously into the reaction mixture using a two-channel syringe pump at a constant flow rate of 0.75 ml/min. Throughout the process, except in final growth step, the cap of the vial was loosely placed to allow air into the reaction mixture. To synthesize Ag nanowires, the reaction mixture was allowed for 4-6 hrs for the nucleation step, and the nucleation time of 14-16 hrs were allowed for nanocube synthesis. The reaction mixture was then allowed for 1-2 hrs for the final growth step. Similar process was used for the synthesis of silver spheres. 5 ml of E.G was heated to 155-160 ^{0}C. 3 ml each of 0.25M $AgNO_3$ and 0.375M of PVP were added to the solution and the vial gap was immediately closed.

The reaction was stopped after 1 hr. The synthesized nanoparticles were washed by centrifugation in acetone and water. The resulting nanoparticles were then sonicated and redispersed in ethanol. The synthesized nanostructures were characterized using scanning electron microscopy (SEM, FEI Nova Nanolab).

3.3.2. SERS and UV-vis extinction measurements

The SERS substrates with different density of silver nanoparticles were prepared by varying the volume (5-35 μL) of the silver nanoparticles (dispersed in ethanol) deposited on aluminum-coated glass substrates (1cm x 1cm). The probe molecules - DPA were then assembled on the surface of silver particles by immersion of the substrates in 1 mM solution of DPA in ethanol for 14 hrs, after that the substrate is allowed to dry. To measure SERS and UV-vis extinction spectra, Nikon L Plan 20x/0.35 objective was used. UV-vis extinction spectrum and SERS spectrum were measured from the same spot (domain) on the substrate by interchanging the UV-vis (deuterium-halogen) light source with UV-vis detector (AvaSpec-2048 spectrometer, Avantes Inc.) and 532 nm laser source with Raman detector (Dimension P1 Raman system, Lambda Solutions Inc.).

3.4. Results and discussion

To investigate the selective Raman scattering enhancement for the targeted vibrational bands, we have used diphenylacetylene (DPA) as it has a wide range of vibrational bands. Here we focus on two vibrational bands – the least shifted vibrational band (996 cm^{-1}) and the most shifted vibrational band (2220 cm^{-1}). It is worth noting that the 2220 cm^{-1} and 996 cm^{-1} Raman bands are of practical

relevance as they are similar to unique modes found in cyanide pollutants (2100 cm^{-1}) and nitrate explosives (1040 cm^{-1}), respectively.[14,15]

There are two accepted mechanisms that are responsible for enhancements of Raman scattering from molecules near plasmonic metal nanostructures; the charge transfer (CT) and electromagnetic (EM) mechanisms.[3–6,16–18] The CT mechanism invokes the excitation of electrons from the metal surface to unpopulated orbitals in the molecule. In general, it is thought that the CT mechanism contributes when the probability for electron scattering into accessible molecular orbitals is high (i.e., resonance cases). [3–6,16–18] The magnitude in the enhancement of Raman signal in these resonance cases is in general higher than the one observed in our system. Therefore we base our analysis on the assumption that the EM mechanism is the dominant one. The EM mechanism occurs due to intense oscillating electromagnetic fields in the near-surface region of optically excited plasmonic nanoparticles. These fields act to enhanced absorption of photons at the incident wavelength as well as the emission of Raman shifted photons at the scattered wavelength.[16,19,20] For the EM enhancement mechanism, the total enhancement factor for a vibrational band, $G(\nu_R)$, is the product of enhancements at the incident and scattered wavelengths,[19]

$$G_{\nu_R} = g(\omega_i) * g(\omega_R) = \left|\frac{E_{loc}(\omega_i)}{E_{inc}(\omega_i)}\right|^2 \left|\frac{E_{loc}(\omega_R)}{E_{inc}(\omega_R)}\right|^2 \qquad (1)$$

where, $g(\omega_i)=|E_{loc}(\omega_i)/E_{inc}(\omega_i)|^2$ and $g(\omega_R)=|E_{loc}(\omega_R)/E_{inc}(\omega_R)|^2$ are the enhancements at the incident laser wavelength (ω_i) and the scattered Raman-shifted wavelength (ω_R), respectively. $E_{loc}(\omega_i)$ and $E_{loc}(\omega_R)$ are the local electric fields at the incident and scattered wavelengths, respectively. The SERS enhancement by the plasmonic

substrates due to EM mechanism at the incident wavelength, $g(\omega_i)$, is identical for different vibrational modes and it cannot be used to selectively enhance a targeted vibrational mode. On the other hand, the EM enhancement at the scattered wavelength, $g(\omega_R)$, can differ for different vibrational bands. Thus, the relative enhancement for different vibrational bands can be expressed as

$$\frac{G_{\nu_{R1}}}{G_{\nu_{R2}}} \propto \frac{g(\omega_{R1})}{g(\omega_{R2})} \quad (2)$$

Equation 2 suggests that selective Raman signal enhancement for a targeted vibrational mode can be achieved by designing plasmonic substrates that selectively enhance the signal of Raman shifted photons at the scattered wavelength that corresponds to the targeted vibrational mode.

In the case study discussed herein, for the 532 nm laser excitation, the Raman scattered photons of the 2220 cm^{-1} and 996 cm^{-1} vibrational bands are at 603.2 nm and 561.8 nm, respectively. According to equation (2), to achieve selective SERS enhancement for the 2220 cm^{-1} and 996 cm^{-1} vibrational bands, the substrates with SPR peaks near 600 nm and 560 nm respectively are required. Below we discuss the design of SERS platforms with these targeted optical properties. Furthermore, we analyze the underlying enhancement mechanism, demonstrating that in this system the EM enhancement mechanisms play the dominant role and that the magnitude of far field extinction due to plasmonic nanoparticle platform is a reasonable predictor of the magnitude of the relative SERS enhancement.

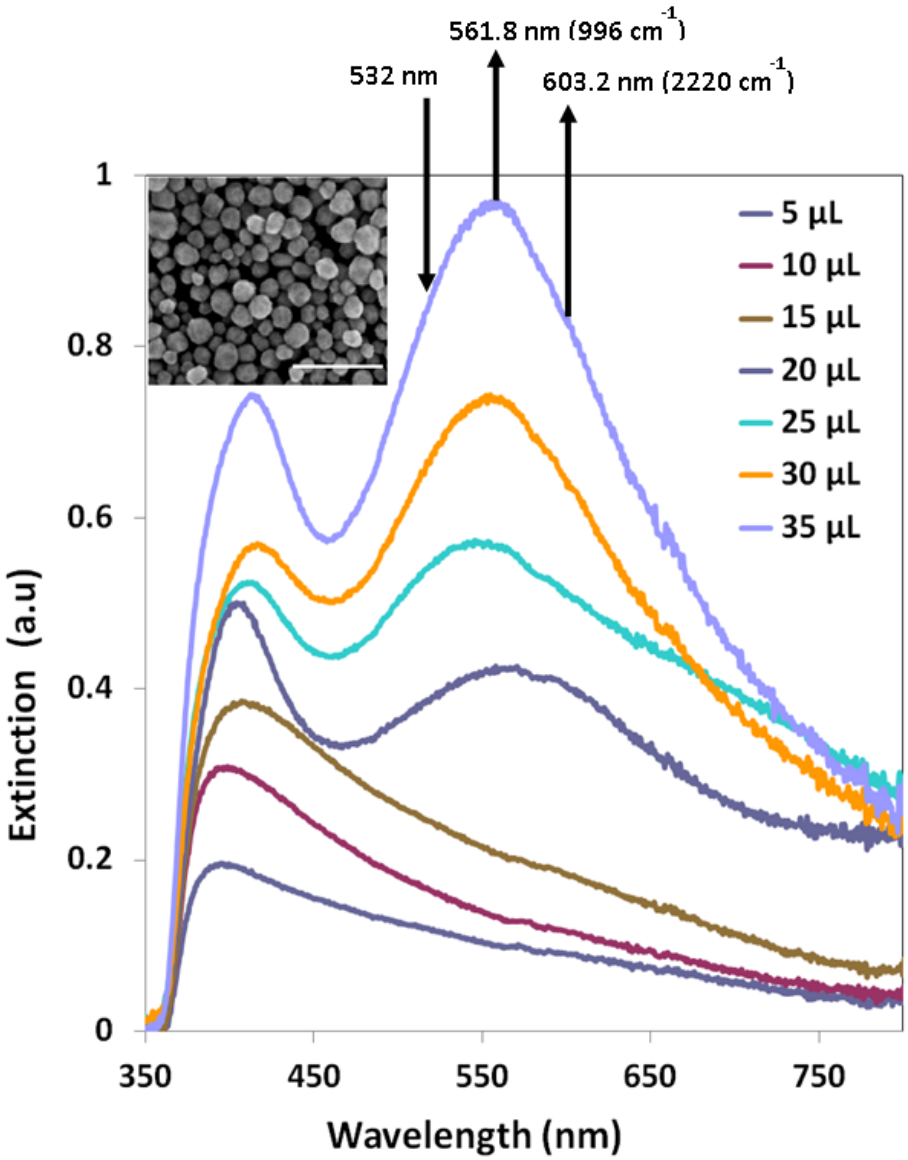

Figure 3.1.a. UV-vis extinction spectra of substrates containing Ag spheres as a function of density of Ag spheres. Figure legends show the amount (volume, µL) of Ag spheres (dispersed in ethanol, ~2 g/L) deposited on the substrates. Inset: Representative scanning electron micrograph of the Ag sphere substrates. Scale bar in SEM image is 400 nm. The wavelengths of the incident (532 nm) and scattered photons (561.8 nm and 603.2 nm) from 996 cm^{-1} and 2220 cm^{-1} vibrational modes of DPA, respectively, are schematically marked by the arrows.

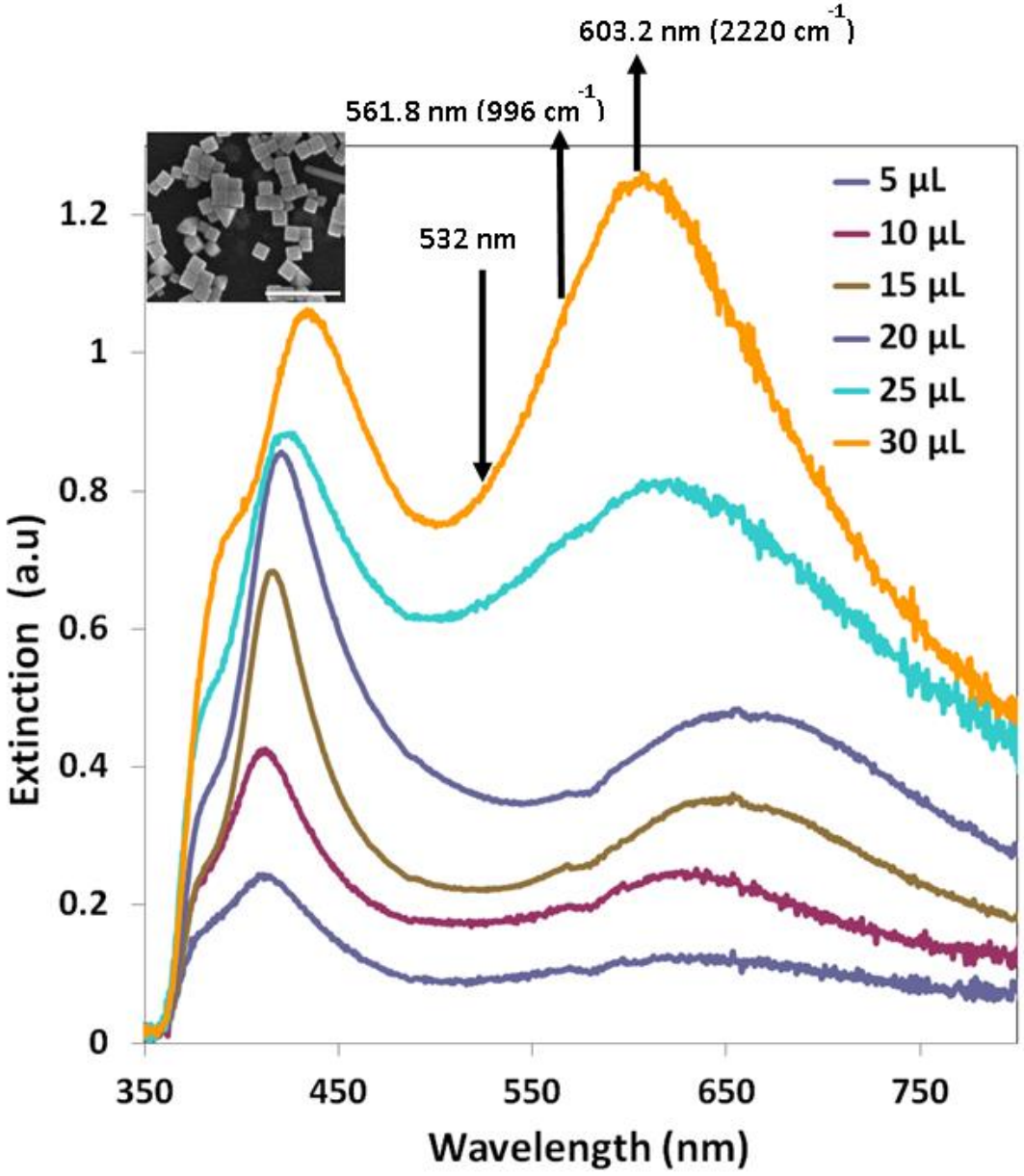

Figure 3.1.b. UV-vis extinction spectra of substrates containing Ag cubes as a function of density of Ag cubes. Figure legends show the amount (volume, µL) of Ag cubes (dispersed in ethanol, ~2 g/L) deposited on the substrates. Inset: Representative scanning electron micrograph of the Ag nanocubes substrates. Scale bar in SEM image is 500 nm. The wavelengths of the incident (532 nm) and scattered photons (561.8 nm and 603.2 nm) from 996 cm^{-1} and 2220 cm^{-1} vibrational modes of DPA respectively are schematically marked by the arrows.

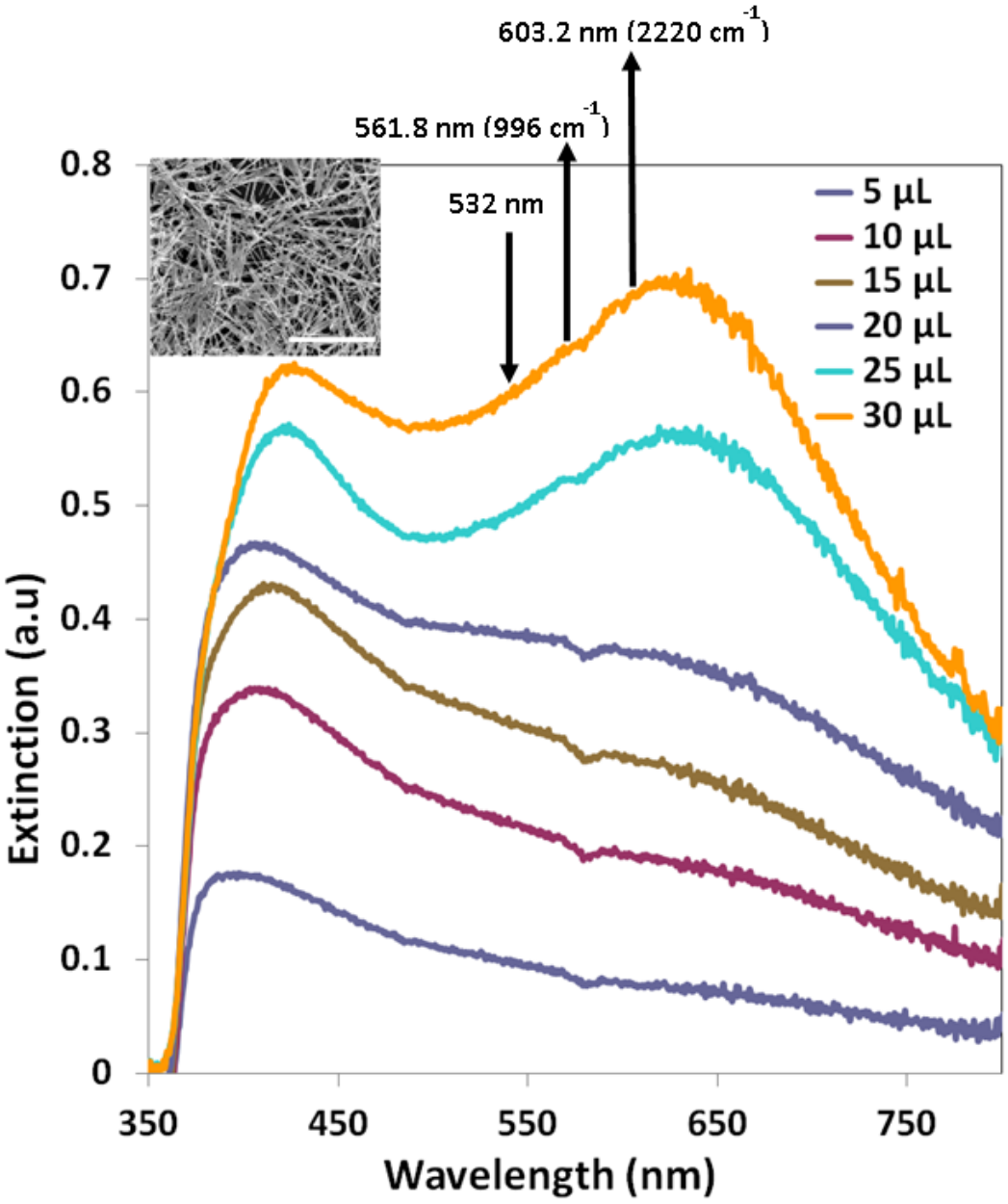

Figure 3.1.c. UV-vis extinction spectra of substrates containing Ag wires as a function of density of Ag wires. Figure legends show the amount (volume, µL) of Ag wires (dispersed in ethanol, ~2 g/L) deposited on the substrates. Inset: Representative scanning electron micrograph of the Ag wires substrates. Scale bar in SEM image is 4 µm. The wavelengths of the incident (532 nm) and scattered photons (561.8 nm and 603.2 nm) from 996 cm^{-1} and 2220 cm^{-1} vibrational modes of DPA respectively are schematically marked by the arrows.

In general, the intensity and resonance wavelength of SPR of metal nanostructures can be tuned by changing the size, shape or composition of the nanoparticle or by changing the local environment, i.e., proximity of nanoparticles or dielectric function of the surrounding medium.[21–34] Although the tuning of SPR spectra of substrates with isolated nanoparticles is possible, plasmonic substrates consisting of nanoparticle dimers and aggregates offer greater SERS enhancements compared to isolated particles.[35–46] This greater SERS enhancement is mainly due to the strong plasmonic coupling between closely spaced particles, which generates large plasmonic field at the hot spots in the aggregates.[47–52]

In Figures 3.1.a-3.1.c, we show the UV-vis extinction spectra of Ag nanoparticle substrates in air on aluminum-coated glass for different particle shapes, sizes, and densities. Representative SEM images of the nanostructures are shown in the insets. The measured extinction spectra of the substrates with low density of silver nanoparticles showed one major SPR peak near 400 nm. This SPR peak can be attributed to the dipole resonance of the discrete silver particles. Additional SPR peaks at lower energy (higher wavelength) were observed with increasing density of silver nanoparticles on the substrate. The SPR peak at the longer wavelength is due to the resonance associated with the particle aggregates, i.e., collection of closely spaced and/or touching particles.[47–52] The lower energy SPR peak (aggregate peak) becomes more dominant with the increase in the density of nanoparticles. The measured extinction spectra in Figures 3.1.a-3.1.c are consistent with simulation results[47–52] and previously reported extinction spectra of similar plasmonic nanoparticle substrates.[35,53] Figure 3.1 shows that the position of the

aggregate peak in the extinction spectrum depends on the shape of the nanoparticles in the aggregate and the aggregate conditions on the substrate. The plasmonic substrates with dominant aggregate peaks near 562 nm was associated with Ag nanospheres (90±16 nm, average diameter) (Figure 3.1.a), while the substrate with the dominant aggregate peak at 600 nm were associated Ag nanocubes (87±9 nm, average edge length) and Ag nanowires (87±16 nm, average diameter) as shown (Figures 3.1.b-3.1.c).

Figures 3.2.a-3.2.c show the intensity of the SERS signals of the targeted 2220 cm^{-1} and 996 cm^{-1} vibrational bands as a function of the density of Ag nanostructures on the substrates. The SPR extinction intensities for the corresponding substrates are shown in Figures 3.1.a-3.1.c. Figure 3.2 shows that to obtain similar magnitude of SERS signal, substrates with Ag nanospheres and nanowires required longer acquisition time (3 s) compared to the Ag nanocube substrates (acquisition time 1 s), i.e., Ag nanocubes show higher SERS activity than Ag nanospheres and nanowires. The likely explanation for the higher SERS activities of Ag nanocubes is that the higher local fields in the sharp edges and corners of the cubes result in higher average SERS signal.[54] Figure 3.2 also shows that all three samples exhibit non-linear increase in SERS signals with respect to particle density. We observe that at higher particle density the SERS signal increases more rapidly with increased density, which is not surprising considering that the concentration of "hot spots" will be higher at higher densities. Most importantly, Figure 3.2 shows that the change in the relative SERS signal ($I_{2220\ cm\text{-}1}/I_{996\ cm\text{-}1}$) as a function of particle density is different for different substrates, i.e., the substrates can be designed to

selectively enhance specific vibrational modes.

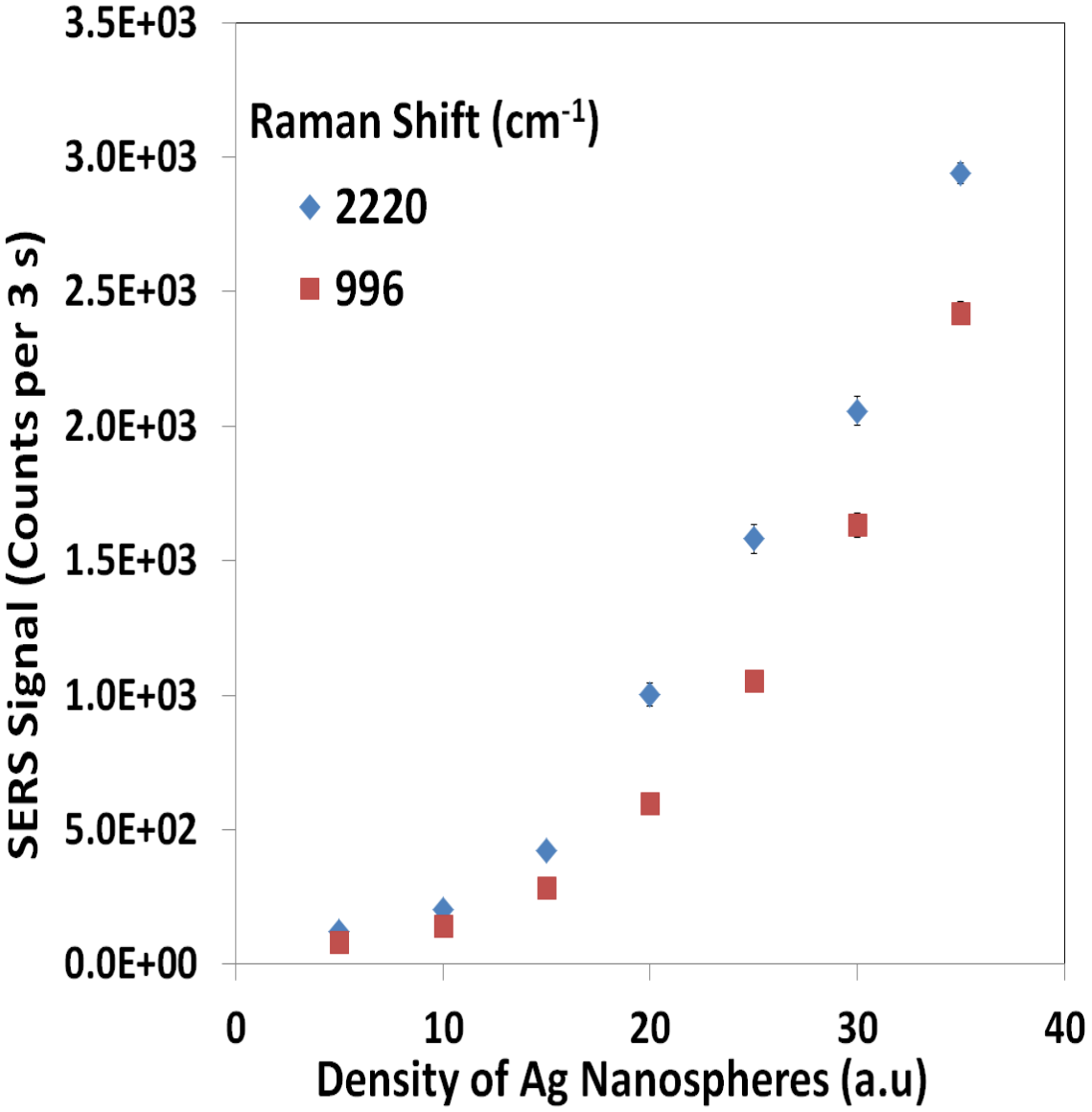

Figure 3.2.a. SERS signal (counts) observed for 2220 cm^{-1} and 996 cm^{-1} vibrational modes of diphenyl acetylene over substrates containing Ag nanospheres as a function of Ag nanoparticle loading. The spectra obtained from the nanosphere substrates were acquired using 3 second collection time.

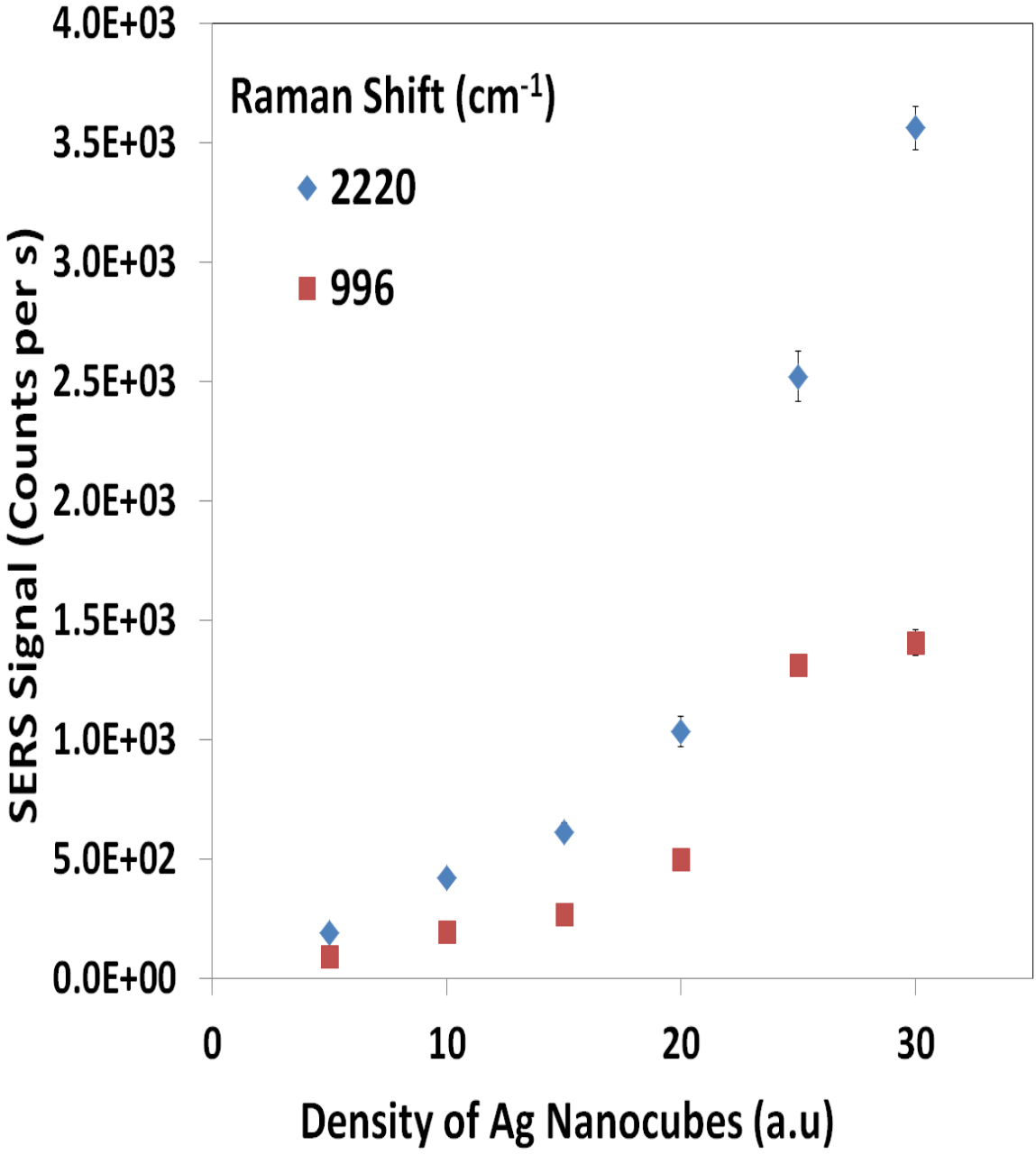

Figure 3.2.b. SERS signal (counts) observed for 2220 cm^{-1} and 996 cm^{-1} vibrational modes of diphenyl acetylene over substrates containing Ag nanocubes as a function of Ag nanoparticle loading. The spectra obtained from the nanocube substrates were acquired using 1 second collection time.

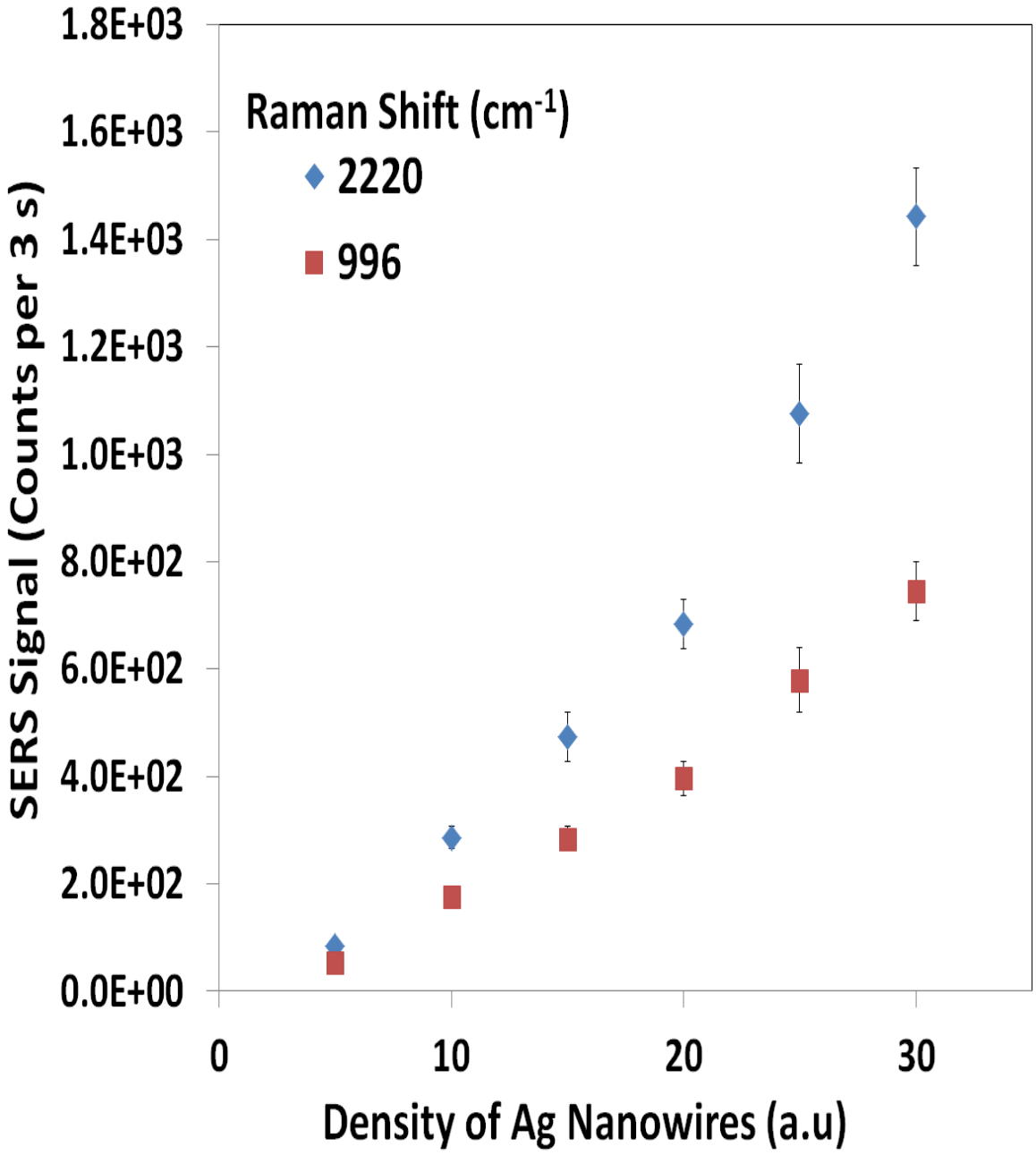

Figure 3.2.c. SERS signal (counts) observed for 2220 cm^{-1} and 996 cm^{-1} vibrational modes of diphenyl acetylene over substrates containing Ag nanowires as a function of Ag nanoparticle loading. The spectra obtained from the nanowire substrates were acquired using 3 second collection time.

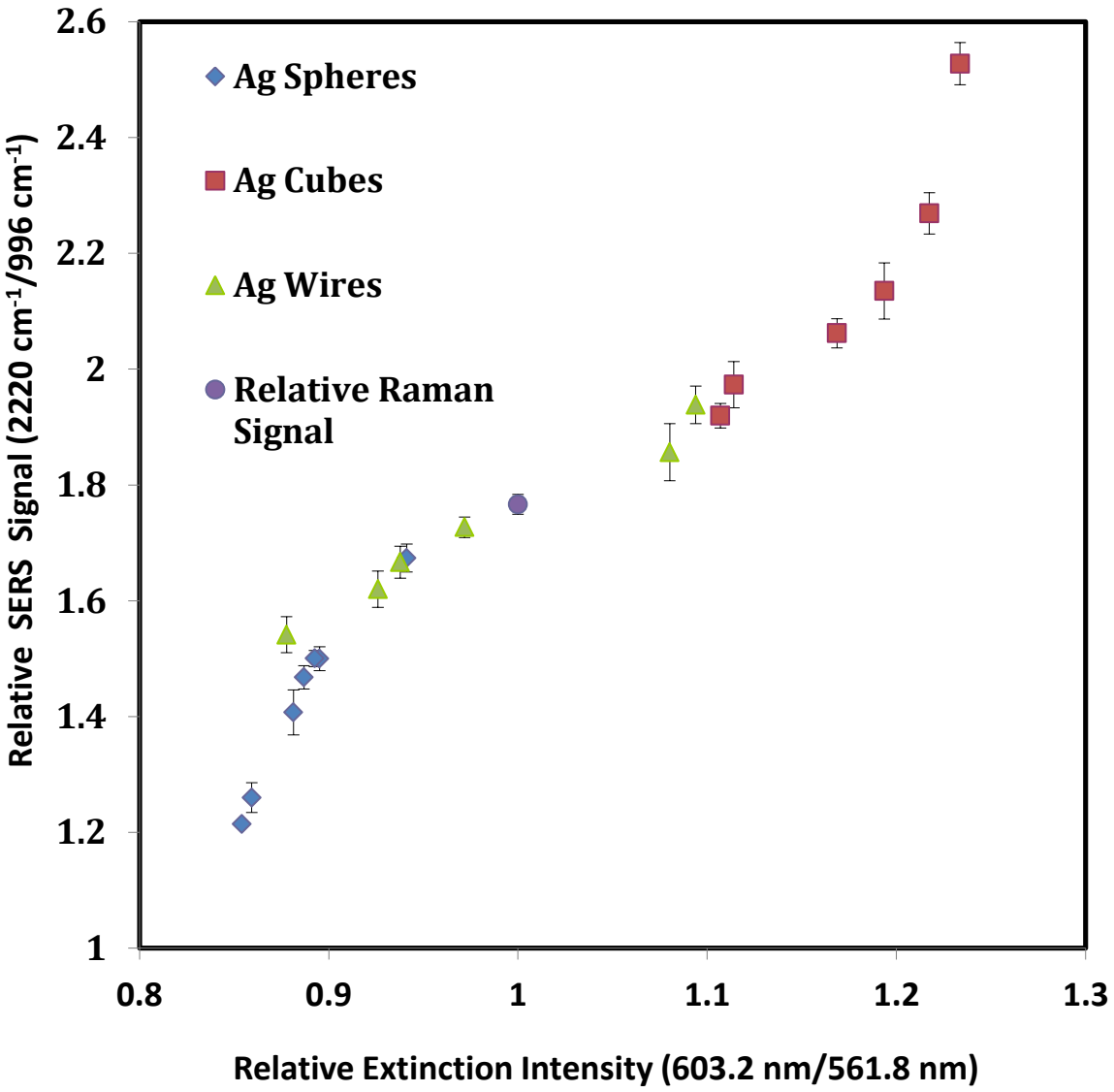

Figure 3.3. Ratio of the measured SERS intensity of 2220 cm^{-1} and 996 cm^{-1} vibrational modes of DPA as a function of the ratio of the substrate extinction intensity at 603.2 nm and 561.8 nm measured from substrates with various Ag nanoparticle shapes at various nanoparticles densities. Intrinsic relative Raman signal of 2220 cm^{-1} and 996 cm^{-1} vibrational modes of diphenyl acetylene observed over the substrate in the absence of silver nanostructure is also included for comparison.

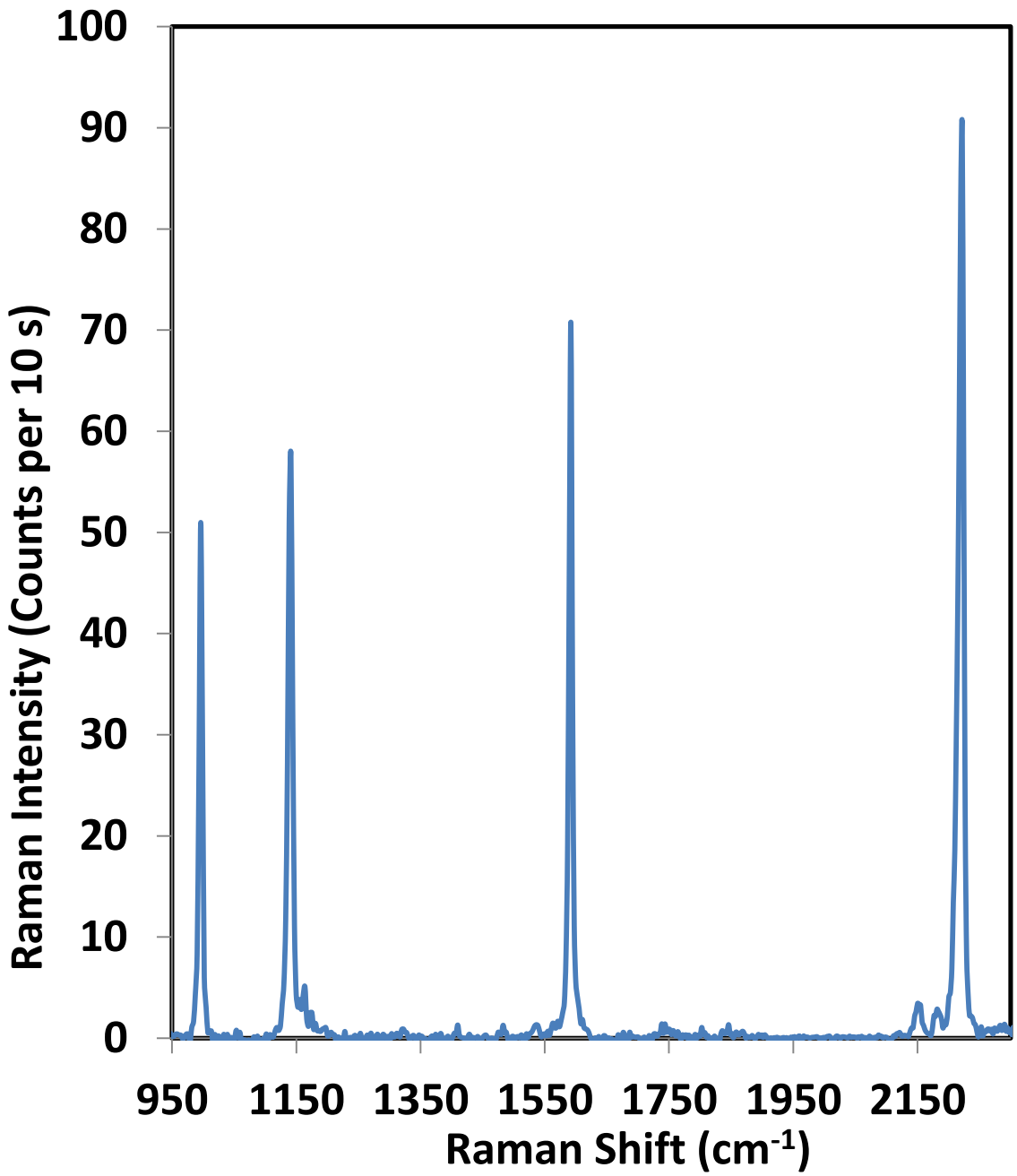

Figure 3.4. Representative Raman spectrum of diphenyl acetylene (0.01 M) measured over the substrate in the absence of silver nanostructures.

To investigate the underlying mechanism that is responsible for the variation in the SERS signals of the - 2220 cm^{-1} and 996 cm^{-1} vibrational bands over different substrates, in Figure 3.3 we plotted the relative SERS signal ($I_{2220cm-1}/I_{996cm-1}$) observed over different substrates versus the relative substrate SPR extinction intensity (the ratio of extinction at the wavelengths of interest, $A_{603.2nm}/A_{561.8nm}$) measured at the same spot (domain) on the substrates.

We note that the intrinsic relative Raman signal value measured without plasmonic nanoparticle substrates from Figure 3.4 was 1.77 ± 0.02 ($I_{2220cm-1}/I_{996cm-1}$ =1.77±0.02). Figure 3.3 shows a positive correlation between the relative SERS signal and relative extinction intensity. This observed positive correlation supports the notion advanced by equations (1) and (2) that the selective scattering enhancement in one Raman band with respect to another is governed by the wavelengths-dependent SPR-mediated enhancements in the emission rates of scattered Raman-shifted photons. Figure 3.3 also shows that the substrates with relative extinction intensity less than 1 ($A_{603.2nm}/A_{561.8nm}<1$) and substrates with relative extinction intensity greater than 1 ($A_{603.2nm}/A_{561.8nm}>1$) preferentially enhance 996 cm^{-1} vibrational mode (i.e., $I_{2220cm-1}/I_{996cm-1}<1.77$) and 2220 cm^{-1} vibrational mode (i.e., $I_{2220cm-1}/I_{996cm-1}>1.77$), respectively. We observe that the highest relative enhancement ($I_{2220cm-1}/I_{996cm-1}$) for the 2220 cm^{-1} band happens over densely packed Ag cubes which are characterized by the highest relative extinction intensity at the wavelength of ~ 603.2 nm. Similarly, the substrate containing densely packed Ag spheres with dominant aggregate peak near 561.8 nm shows selective vibrational band enhancement for the 996 cm^{-1} vibrational mode.

The observed positive correlation between the intensity of scattered Raman-shifted photons of a particular wavelength and the intensity of SPR at the given wavelength suggests that the relative magnitude of far field extinction (measured as extinction spectra due to the excitation of SPR) is a good descriptor of the relative SERS enhancement magnitude. We note that the SERS enhancement inherently depends on the intensity of the electromagnetic fields in the close proximity of the substrate (i.e., the near field properties of the substrate). Since the far field extinction for a given sensor geometry can be easily measured or computed, this positive relationship between the far field extinction and SERS enhancements provides us with a simple qualitative predictive descriptor for the design of optimal SERS platforms that offer molecular sensitivity. It is worth noting that Mie theory for individual spherical particles in the quasi-static limit predicts that the SRES enhancement (g) is proportional to the square of the far field optical cross section (A^2).[19] Our studies indicate that the positive correlation applies even for more complex substrate geometries. We find that in general, the plasmonic sensor platforms that exhibit the highest far field extinction intensity at the wavelength of Raman-shifted photons will selectively enhance the vibrational mode corresponding to the particular wavelength. For example, using a 532 nm photon source, the substrate with high density of Ag nanocubes (~ 90 nm in characteristic length) could be used to selectively detect cyanide pollutants or any other species (or functional groups) with (2100-2200 cm^{-1}) Raman vibrational bands. Similarly, aggregates of Ag nanospheres offer high selectivity for analytes with 900–1000 cm^{-1} vibrational modes.

3.5. Conclusions

In conclusion, we demonstrated the design of plasmonic substrates that selectively enhance specific Raman vibrational bands, thereby offering high molecular selectivity and sensitivity. We showed that when using the 532 nm photon source, the substrates with desired optical properties can be designed by densely packing Ag nanostructure of targeted size and shape. By correlating the optical extinction spectra of substrates and the enhancement factors for different Raman vibrational bands we demonstrate that the observed difference in the enhancement of vibrational modes is due to the difference in the surface plasmon resonance intensity at the Stokes Raman shifted wavelengths. Similar design principles could be used to devise plasmonic platforms for various applications that require selective enhancements in absorption or emission rates, including surface-enhanced fluorescence (SEF) or surface enhanced infra-red spetroscopy.[16,20]

3.6. References

(1) Williams, C. T.; Chan, H. Y. H.; Tolia, A. A.; Weaver, M. J.; Takoudis, C. G. In Situ Real-Time Studies of Heterogeneous Catalytic Mechanisms at Ambient Pressures As Probed by Surface-Enhanced Raman and Mass Spectroscopies. Ind. Eng. Chem. Res. 1998, 37, 2307–2315.

(2) Pettinger, B.; Bao, X.; Wilcock, I.; Muhler, M.; Schlögl, R.; Ertl, G. Thermal Decomposition of Silver Oxide Monitored by Raman Spectroscopy: From AgO Units to Oxygen Atoms Chemisorbed on the Silver Surface. Angewandte Chemie 1994, 33, 85–86.

(3) Camden, J. P.; Dieringer, J. A.; Zhao, J.; Van Duyne, R. P. Controlled Plasmonic Nanostructures for Surface-Enhanced Spectroscopy and Sensing. Acc. Chem. Res. 2008, 41, 1653–1661.

(4) Stiles, P. L.; Dieringer, J. A.; Shah, N. C.; Van Duyne, R. P. Surface-Enhanced Raman Spectroscopy. Annual Review of Analytical Chemistry 2008, 1, 601–626.

(5) Qian, X.-M.; Nie, S. M. Single-molecule and single-nanoparticle SERS: from

fundamental mechanisms to biomedical applications. Chem. Soc. Rev. 2008, 37, 912–920.

(6) Kneipp, K.; Kneipp, H.; Kneipp, J. Surface-Enhanced Raman Scattering in Local Optical Fields of Silver and Gold NanoaggregatesFrom Single-Molecule Raman Spectroscopy to Ultrasensitive Probing in Live Cells. Acc. Chem. Res. 2006, 39, 443–450.

(7) Lu, X.; Rycenga, M.; Skrabalak, S. E.; Wiley, B.; Xia, Y. Chemical Synthesis of Novel Plasmonic Nanoparticles. Annual Review of Physical Chemistry 2009, 60, 167–192.

(8) Ingram, D. B.; Linic, S. Water Splitting on Composite Plasmonic-Metal/Semiconductor Photoelectrodes: Evidence for Selective Plasmon-Induced Formation of Charge Carriers near the Semiconductor Surface. J. Am. Chem. Soc. 2011, 133, 5202–5205.

(9) Ingram, D. B.; Christopher, P.; Bauer, J. L.; Linic, S. Predictive Model for the Design of Plasmonic Metal/Semiconductor Composite Photocatalysts. ACS Catal. 2011, 1, 1441–1447.

(10) Christopher, P.; Ingram, D. B.; Linic, S. Enhancing Photochemical Activity of Semiconductor Nanoparticles with Optically Active Ag Nanostructures: Photochemistry Mediated by Ag Surface Plasmons. J. Phys. Chem. C 2010, 114, 9173–9177.

(11) Christopher, P.; Linic, S. Engineering Selectivity in Heterogeneous Catalysis: Ag Nanowires as Selective Ethylene Epoxidation Catalysts. J. Am. Chem. Soc. 2008, 130, 11264–11265.

(12) Christopher, P.; Linic, S. Shape- and Size-Specific Chemistry of Ag Nanostructures in Catalytic Ethylene Epoxidation. ChemCatChem 2010, 2, 78–83.

(13) Christopher, P.; Xin, H.; Linic, S. Visible-light-enhanced catalytic oxidation reactions on plasmonic silver nanostructures. Nat. Chem. 2011, 3, 467–472.

(14) Yea, K.; Lee, S.; Kyong, J. B.; Choo, J.; Lee, E. K.; Joo, S.-W.; Lee, S. Ultra-sensitive trace analysis of cyanide water pollutant in a PDMS microfluidic channel using surface-enhanced Raman spectroscopy. Analyst 2005, 130, 1009–1011.

(15) Ali, E. M. A.; Edwards, H. G. M.; Hargreaves, M. D.; Scowen, I. J. Detection of explosives on human nail using confocal Raman microscopy. Journal of Raman Spectroscopy 2009, 40, 144–149.

(16) Ru, E. L.; Etchegoin, P. Principles of Surface-Enhanced Raman Spectroscopy: and related plasmonic effects; 1st ed.; Elsevier Science, 2008.

(17) Moskovits, M. Surface-enhanced Raman spectroscopy: a brief retrospective. Journal of Raman Spectroscopy 2005, 36, 485–496.

(18) Brus, L. Noble Metal Nanocrystals: Plasmon Electron Transfer Photochemistry and Single-Molecule Raman Spectroscopy. Acc. Chem. Res. 2008, 41, 1742–1749.

(19) Kreibig, U.; Vollmer, M. Optical Properties of Metal Clusters; 1st ed.; Springer, 1995.

(20) Gray, S. K. Surface Plasmon-Enhanced Spectroscopy and Photochemistry. Plasmonics 2007, 2, 143–146.

(21) Linic, S.; Christopher, P.; Ingram, D. B. Plasmonic-metal nanostructures for efficient conversion of solar to chemical energy. Nat. Mater. 2011, 10, 911–921.

(22) Wiley, B.; Sun, Y.; Xia, Y. Synthesis of Silver Nanostructures with Controlled Shapes and Properties. Acc. Chem. Res. 2007, 40, 1067–1076.

(23) Xia, Y.; Halas, N. J. Shape-Controlled Synthesis and Surface Plasmonic Properties of Metallic Nanostructures. MRS Bulletin 2005, 30, 338–348.

(24) Kelly, K. L.; Coronado, E.; Zhao, L. L.; Schatz, G. C. The Optical Properties of Metal Nanoparticles: The Influence of Size, Shape, and Dielectric Environment. J. Phys. Chem. B 2002, 107, 668–677.

(25) Zhang, W.; Fischer, H.; Schmid, T.; Zenobi, R.; Martin, O. J. F. Mode-Selective Surface-Enhanced Raman Spectroscopy Using Nanofabricated Plasmonic Dipole Antennas. J. Phys. Chem. C 2009, 113, 14672–14675.

(26) Jain, P. K.; Huang, X.; El-Sayed, I. H.; El-Sayed, M. A. Review of Some Interesting Surface Plasmon Resonance-enhanced Properties of Noble Metal Nanoparticles and Their Applications to Biosystems. Plasmonics 2007, 2, 107–118.

(27) Anker, J. N.; Hall, W. P.; Lyandres, O.; Shah, N. C.; Zhao, J.; Van Duyne, R. P. Biosensing with plasmonic nanosensors. Nat Mater 2008, 7, 442–453.

(28) El-Sayed, M. A. Some Interesting Properties of Metals Confined in Time and Nanometer Space of Different Shapes. Acc. Chem. Res. 2001, 34, 257–264.

(29) Zhu, Z.; Zhu, T.; Liu, Z. Raman scattering enhancement contributed from individual gold nanoparticles and interparticle coupling. Nanotechnology 2004, 15, 357.

(30) Lu, Y.; Liu, G. L.; Lee, L. P. High-Density Silver Nanoparticle Film with Temperature-Controllable Interparticle Spacing for a Tunable Surface Enhanced Raman Scattering Substrate. Nano Lett. 2005, 5, 5–9.

(31) Jain, P. K.; Huang, X.; El-Sayed, I. H.; El-Sayed, M. A. Noble Metals on the Nanoscale: Optical and Photothermal Properties and Some Applications in Imaging, Sensing, Biology, and Medicine. Acc. Chem. Res. 2008, 41, 1578–1586.

(32) Link, S.; El-Sayed, M. A. Size and Temperature Dependence of the Plasmon Absorption of Colloidal Gold Nanoparticles. J. Phys. Chem. B 1999, 103, 4212–4217.

(33) Evanoff, D. D.; Chumanov, G. Size-Controlled Synthesis of Nanoparticles. 2. Measurement of Extinction, Scattering, and Absorption Cross Sections. J. Phys. Chem. B 2004, 108, 13957–13962.

(34) Link, S.; El-Sayed, M. A. Spectral Properties and Relaxation Dynamics of Surface Plasmon Electronic Oscillations in Gold and Silver Nanodots and Nanorods. J. Phys. Chem. B 1999, 103, 8410–8426.

(35) Mahmoud, M. A.; Tabor, C. E.; El-Sayed, M. A. Surface-Enhanced Raman Scattering Enhancement by Aggregated Silver Nanocube Monolayers Assembled by the Langmuir–Blodgett Technique at Different Surface Pressures. J. Phys. Chem. C 2009, 113, 5493–5501.

(36) Rycenga, M.; Camargo, P. H. C.; Li, W.; Moran, C. H.; Xia, Y. Understanding the SERS Effects of Single Silver Nanoparticles and Their Dimers, One at a Time. J. Phys. Chem. Lett. 2010, 1, 696–703.

(37) Svedberg, F.; Li, Z.; Xu, H.; Käll, M. Creating Hot Nanoparticle Pairs for Surface-Enhanced Raman Spectroscopy through Optical Manipulation. Nano Lett. 2006, 6, 2639–2641.

(38) Talley, C. E.; Jackson, J. B.; Oubre, C.; Grady, N. K.; Hollars, C. W.; Lane, S. M.; Huser, T. R.; Nordlander, P.; Halas, N. J. Surface-Enhanced Raman Scattering from Individual Au Nanoparticles and Nanoparticle Dimer Substrates. Nano Lett. 2005, 5, 1569–1574.

(39) Budnyk, A. P.; Damin, A.; Agostini, G.; Zecchina, A. Gold Nanoparticle Aggregates Immobilized on High Surface Area Silica Substrate for Efficient and Clean SERS Applications. J. Phys. Chem. C 2010, 114, 3857–3862.

(40) Schwartzberg, A. M.; Grant, C. D.; Wolcott, A.; Talley, C. E.; Huser, T. R.; Bogomolni, R.; Zhang, J. Z. Unique Gold Nanoparticle Aggregates as a Highly Active Surface-Enhanced Raman Scattering Substrate. J. Phys. Chem. B 2004, 108, 19191–19197.

(41) Xu, H.; Bjerneld, E. J.; Käll, M.; Börjesson, L. Spectroscopy of Single Hemoglobin Molecules by Surface Enhanced Raman Scattering. Phys. Rev. Lett. 1999, 83, 4357–4360.

(42) Futamata, M. Single molecule sensitivity in SERS: importance of junction of adjacent Ag nanoparticles. Faraday Discuss. 2006, 132, 45–61.

(43) Futamata, M.; Maruyama, Y.; Ishikawa, M. Critical importance of the junction in touching Ag particles for single molecule sensitivity in SERS. Journal of Molecular Structure 2005, 735–736, 75–84.

(44) Li, W.; Camargo, P. H. C.; Lu, X.; Xia, Y. Dimers of Silver Nanospheres: Facile Synthesis and Their Use as Hot Spots for Surface-Enhanced Raman Scattering. Nano Lett. 2009, 9, 485–490.

(45) Kleinman, S. L.; Bingham, J. M.; Henry, A.-I.; Wustholz, K. L.; Van Duyne, R. P. Structural and optical characterization of single nanoparticles and single molecule SERS. 2010, 77570J–77570J.

(46) Camden, J. P.; Dieringer, J. A.; Wang, Y.; Masiello, D. J.; Marks, L. D.; Schatz, G. C.; Van Duyne, R. P. Probing the Structure of Single-Molecule Surface-Enhanced Raman Scattering Hot Spots. J. Am. Chem. Soc. 2008, 130, 12616–12617.

(47) Kottmann, J.; Martin, O. Plasmon resonant coupling in metallic nanowires. Opt. Express 2001, 8, 655–663.

(48) Romero, I.; Aizpurua, J.; Bryant, G. W.; Garcia De Abajo, F. J. Plasmons in nearly touching metallic nanoparticles: singular response in the limit of touching dimers. Opt. Express 2006, 14, 9988–9999.

(49) Foteinopoulou, S.; Vigneron, J. P.; Vandenbem, C. Optical near-field excitations on plasmonic nanoparticle-based structures. Opt. Express 2007, 15, 4253–4267.

(50) Zuloaga, J.; Prodan, E.; Nordlander, P. Quantum Description of the Plasmon Resonances of a Nanoparticle Dimer. Nano Lett. 2009, 9, 887–891.

(51) Hao, E.; Schatz, G. C. Electromagnetic fields around silver nanoparticles and dimers. The Journal of Chemical Physics 2004, 120, 357–366.

(52) McMahon, J. M.; Henry, A.-I.; Wustholz, K. L.; Natan, M. J.; Freeman, R. G.; Duyne, R. P. V.; Schatz, G. C. Gold nanoparticle dimer plasmonics: finite element method calculations of the electromagnetic enhancement to surface-enhanced Raman spectroscopy. Anal Bioanal Chem 2009, 394, 1819–1825.

(53) Jackson, J. B.; Halas, N. J. Surface-enhanced Raman scattering on tunable plasmonic nanoparticle substrates. PNAS 2004, 101, 17930–17935.

(54) McLellan, J. M.; Siekkinen, A.; Chen, J.; Xia, Y. Comparison of the surface-enhanced Raman scattering on sharp and truncated silver nanocubes. Chemical Physics Letters 2006, 427, 122–126.

CHAPTER 4

Tuning selectivity in propylene epoxidation by plasmon mediated photo-switching of Cu oxidation state

4.1. Summary

Oxidation of functioning copper has restricted its applicability as a catalyst for commercially important epoxidation of propylene to form propylene oxide. In this chapter, we report that steady state selectivity in propylene epoxidation on Cu nanoparticles increases sharply when the catalyst is illuminated with visible light. The selectivity increase is accompanied by light-induced reduction of the surface Cu atoms, which is brought about by photo-excitation of the surface plasmon resonance (SPR) of Cu. We discuss multiple mechanisms by which Cu SPR weakens the Cu-O bonds thereby reducing Cu_2O.

4.2. Introduction

Heterogeneous catalysts evolve under operating conditions to a steady chemical state that can manifest distinct reactivity from the initial, as-prepared material. For instance, ultra-high vacuum (UHV) experiments on well-defined Copper (Cu) single crystal surfaces have shown that metallic Cu exhibits high selectivity to epoxide products in the epoxidation of multiple olefins, including commercially critical

epoxidation of propylene to form propylene oxide ($C_3H_6 + 1/2O_2 \rightarrow C_3H_6O$).[1–4] However, under realistic propylene epoxidation conditions, characterized by equimolar amounts of propylene and oxygen and temperature of ~ 400 - 500 K, Cu is oxidized.[4–6] On the oxidized Cu surface the selectivity to the desired propylene oxide (PO) product is very low.

In this chapter, we demonstrate an approach to manipulate the oxidation state of Cu catalysts under operating propylene epoxidation conditions and thereby change the selectivity of the catalyst to favor PO production. The approach takes advantage of the strong interactions of Cu nanoparticles with visible light manifested in the photo-excitation of the surface plasmon resonance (SPR).[7–9] We find that heterogeneous catalysts containing Cu nanoparticles exhibit a sharp increase in the steady state selectivity to propylene oxide from ~ 20 % to ~ 50 % when illuminated with visible light. This increase in the selectivity is accompanied by light-induced change in the oxidation state of the surface Cu atoms from Cu-oxide (light off) to Cu metal (light on).

4.3. Methods

4.3.1. Preparation of catalyst

Copper nanoparticle catalysts were prepared using (water in oil) micro emulsion synthesis method reported previously.[10] n-heptane (99% purity, Sigma-Aldrich Cat. No. 246654), polyethylene glycol-dodecyl ether (average M_n ~362, Sigma-Aldrich Cat. No. 235989), copper nitrate (99.999%, Sigma-Aldrich Cat. No. 229636) and hydrazine (98% purity, Sigma-Aldrich Cat. No. 215155) were used as

continuous oil phase, surfactant, copper precursor and reducing agent, respectively. Water to surfactant (molar) ratio of 30 and reducing agent to precursor ratio of 10 were used for the synthesis. Briefly, an aqueous solution of copper precursor (0.1 M $Cu(NO_3)_2$) was added to the mixture of n-heptane and surfactant (16.54 wt%) under inert atmosphere (argon). After the mixture was equilibrated, an aqueous solution of reducing agent (1 M hydrazine) was added drop by drop to the mixture and the microemulsion was kept under continuous stirring in inert atmosphere (argon) at room temperature for the complete reduction of copper precursor. A known amount of support material, SiO_2, (Surface area ~80-100 m^2/g, Alfa Aesar, Product No. 42737) was then added under stirring to the microemulsion containing copper nanoparticles to prepare catalyst with final composition of ~2 wt % Cu/SiO_2. Acetone was then added to the mixture under stirring to break the microemulsion and remove the surfactant. The catalyst was further washed with water and ethanol to remove remaining surfactant by centrifugation and dried in argon at room temperature.

4.3.2. Characterization of catalyst

The scanning electron microscope (SEM) images of the copper nanoparticles and the catalyst (~2% Cu/SiO_2) were obtained using an FEI Nova 200 Nanolab and Philips XL30FEG, respectively. Representative scanning electron microscope (SEM) images of the copper nanoparticles and the catalyst (~2% Cu/SiO_2) are shown in Figures 4.1.a and 4.1.b, respectively. SEM images of the copper nanoparticles synthesized showed that the particles are quasi-spherical in shape with average size

of 41 ± 9 nm. UV-Vis extinction spectra of the catalysts were measured using Thermo Scientific Evolution 300 UV-Vis Spectrophotometer with a Harrick Praying Mantis Diffuse Reflection Accessory. Harrick High Temperature Reaction Chamber used to carry out reactions under thermal and photothermal conditions is equipped with silica windows which allow recording of the UV-Vis spectra of the catalyst under in situ conditions. X-ray diffraction (XRD) patterns of the used catalysts were acquired using Rigaku Miniflex DMAX-B rotating anode X-ray diffractometer with Cu-Kα radiation source operated at 30 kV and 15 mA.

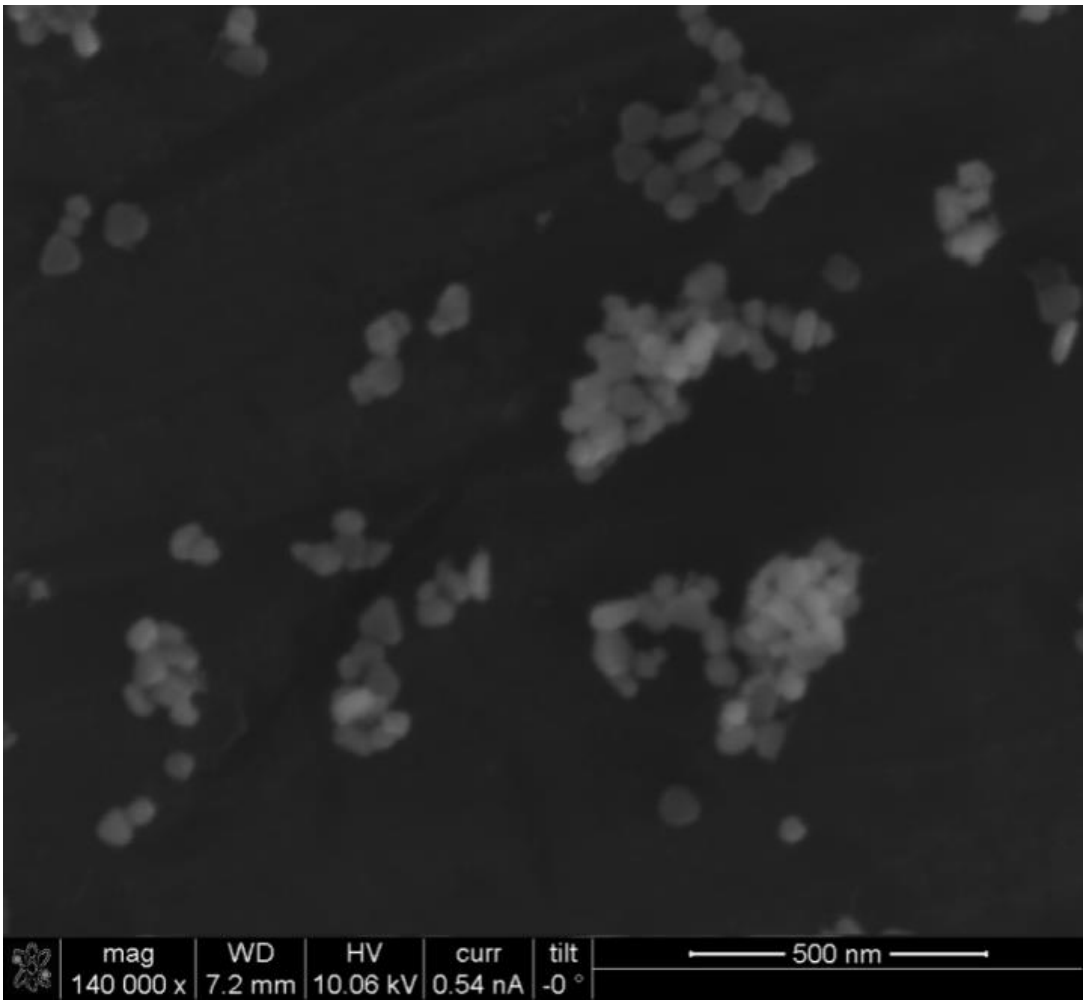

Figure. 4.1.a. SEM image of copper nanoparticles deposited on a silicon wafer.

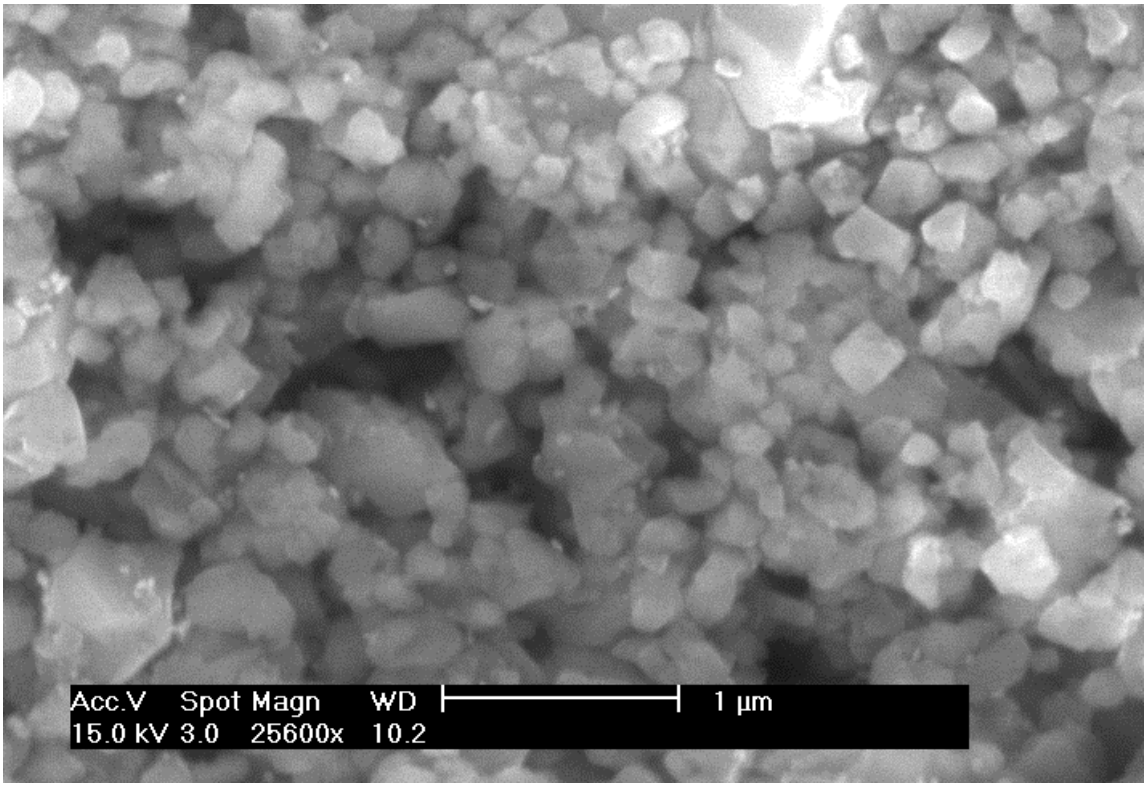

Figure. 4.1.b. SEM image of copper nanoparticles dispersed on SiO_2 support. Smaller particles are Cu nanoparticles.

4.3.3. Reactor studies

The reactions were performed in a vertically oriented packed bed reactor (Harrick High Temperature Reaction Chamber) that allowed both temperature control through electrical heating at the bottom and light illumination through $1cm^2$ silica window at the top of the reactor.[8] The catalyst (packed) bed was prepared by loading 10 mg of inert silica beads (Silica gel, Sigma-Aldrich Cat. No. 214418) to the bottom of the reactor and 12 mg of 2 wt% Cu/SiO_2 catalysts on top of the layers of silica beads. The reactants and products were analyzed online using a gas chromatography (GC, Varian CP 3800) equipped with thermal conductivity and flame ionization detectors, and quadrupole mass spectrometry (MS, Extorr XT200).

For all reactions reported here, the catalysts were first pre-reduced at 523K for 1 hr in 20% hydrogen (remaining helium) at a total flow rate of 100 cm^3/min (sccm). The reactants with a composition of 50% propylene and 50% oxygen at a total flow rate of 100 cm^3/min were then introduced to the catalyst bed at 523K, and left overnight to remove remaining surfactant and to reach steady state. The catalysts were then exposed to the specified reaction temperature (and light intensity). In these tests over the catalysts, at specified temperature (and light intensity), the system was allowed 30 minutes to reach steady state, and the steady state data collected after 30 minutes using GC were used to calculate the rate and product selectivity.

The rate and selectivity results reported here for thermal (light off) and photothermal (light on) conditions were measured in a differential reactor set-up under steady state reaction conditions. Propylene oxide (PO), acrolein (Acr) and carbon dioxide (CO_2) were observed as the principal products. The reaction rates were calculated using the rate of product formation, i.e., the reaction rates of propylene consumption were calculated using the formula, $(r_{PO}+r_{Acr}+r_{CO2}/3)$, where, r_{PO}, r_{Acr} and r_{CO2} denote the measured rate of formation of the products- PO, acrolein and CO_2, respectively. The PO, acrolein and CO_2 selectivity were calculated using the formulae- $r_{PO}/(r_{PO}+r_{Acr}+r_{CO2}/3)$, $r_{Acr}/(r_{PO}+r_{Acr}+r_{CO2}/3)$ and $(r_{CO2}/3)/(r_{PO}+r_{Acr}+r_{CO2}/3)$, respectively. The reaction rate and selectivity data shown in the figures represent the average values of the results obtained from multiple independent experiments as described in the figure captions and the error bars in the data represent the standard deviations.

The light source used for the photothermal studies (light on) was a broadband visible light source with a maximum spectral intensity at ~580 nm as shown in Figure 4.2. The source intensity was calibrated using CCD camera and intensity meter (OAI Instruments). For the wavelength dependent photototthermal experiments, optical filters (Edmund Optics) were used to control the wavelength of light reaching the catalyst from the light source and the intensity of light reaching the catalyst surface was kept constant (~ 550 mW/cm^2) for all experiments by controlling the power to the light source.

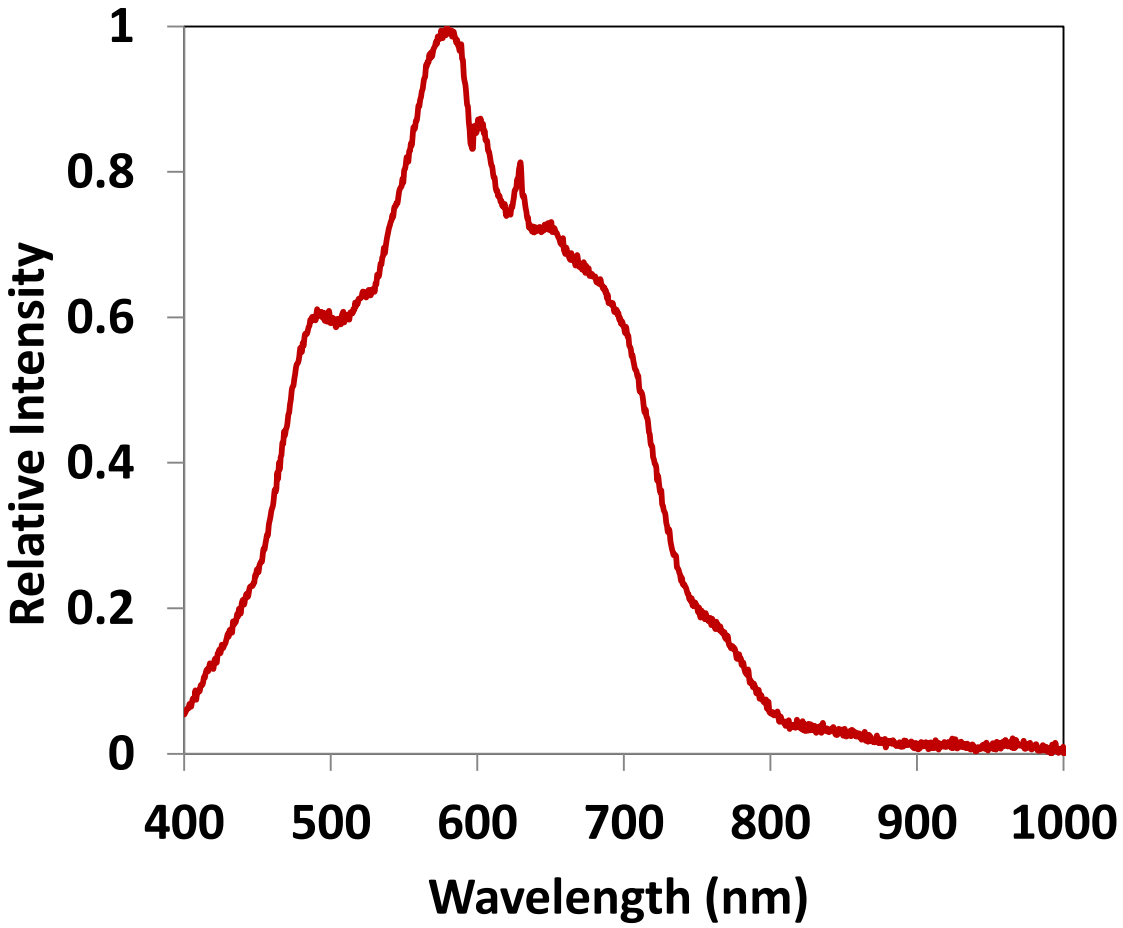

Figure 4.2. Spectrum of the light source used in the photothermal studies.

4.4. Results and discussion

Figure 4.3.a shows steady state PO selectivity and reaction rate measured at 473 K as a function of light intensity. The data show that the PO selectivity is ~ 20 % (with the balance consisting of CO_2 and acrolein, see Figure 4.3.b) for visible light intensity below ~ 550 mW/cm^2 (~ 4 to 5 Suns). The selectivity to PO rapidly increases to ~ 50 % as the light intensity crosses the threshold of ~ 550 mW/cm^2. The data also show that the reaction rate increases for intensities up to 550 mW/cm^2 followed by a sharp decrease at ~ 550 mW/cm^2. We made similar trend in the rate and PO selectivity for the range of operating temperature between 473 and 553 K. The transient kinetic data observed at threshold light intensity, for example, MS signals observed at m/z=44, which is related to the CO_2 formation rate and thus the rate of propylene consumption under photothermal conditions (light on) at 473K is shown in Figure 4.3.c. When the light intensity was increased to threshold intensity of ~550 mW/cm^2 (at ~12 minutes in Figure 4.3.c), huge instantaneous change in the MS signal was observed before reaching the steady state signals (~25 minutes in Figure 4.3.c). This observation indicates the possible surface phase transformation of catalyst surface when the light intensity crosses the threshold intensity.

To demonstrate that the observed increase in PO selectivity shown in Figures 4.3.a and 4.3.b is not a direct consequence of the drop in the reaction rates at 550 mW/cm^2, we compared the PO selectivity for the thermal process (no light illumination) to the selectivity on identical catalysts illuminated with the visible

light at 550 mW/cm^2 at constant reaction rates in Figure 4.4.a (also see Figure 4.4.b and 4.4.c). In these experiments, the rate for the light-off and light-on measurements was kept constant by adjusting the operating temperature. The data show that for all measured rates the steady state PO selectivity and therefore the PO yield is significantly higher for the illuminated catalyst. Essentially, the data in Figure 4.4.a show that the steady state catalytic process undergoes a dramatic change, manifested as a rapid increase in the PO selectivity and a concurrent drop in the steady state reaction rate, as the light intensity threshold of ~ 550 mW/cm^2 is crossed.

As stated above, UHV studies on model systems have shown that the oxidation state of surface Cu atoms affects the selectivity of Cu-based catalysts in epoxidation reactions, with metallic Cu yielding higher epoxide selectivity than the oxidized Cu surface.[1–4] To test whether the light-induced reduction of Cu-oxide to Cu metal might be responsible for the observed increase in the PO selectivity, we characterized the Cu catalysts using in-situ UV-vis extinction spectroscopy. In Figure 4.5.a, we show the extinction spectrum of the catalyst, containing nanoparticles of Cu on SiO_2, reduced in 20% H_2 (balance helium) at a temperature of 523 K and atmospheric pressure. It is well established that the extinction peak at ~ 565 nm is a signature of metallic Cu nanoparticles[11,12] (see Figure 4.5.b). The extinction is due to the excitation of the surface plasmon resonance (SPR) in metallic Cu nanoparticles.

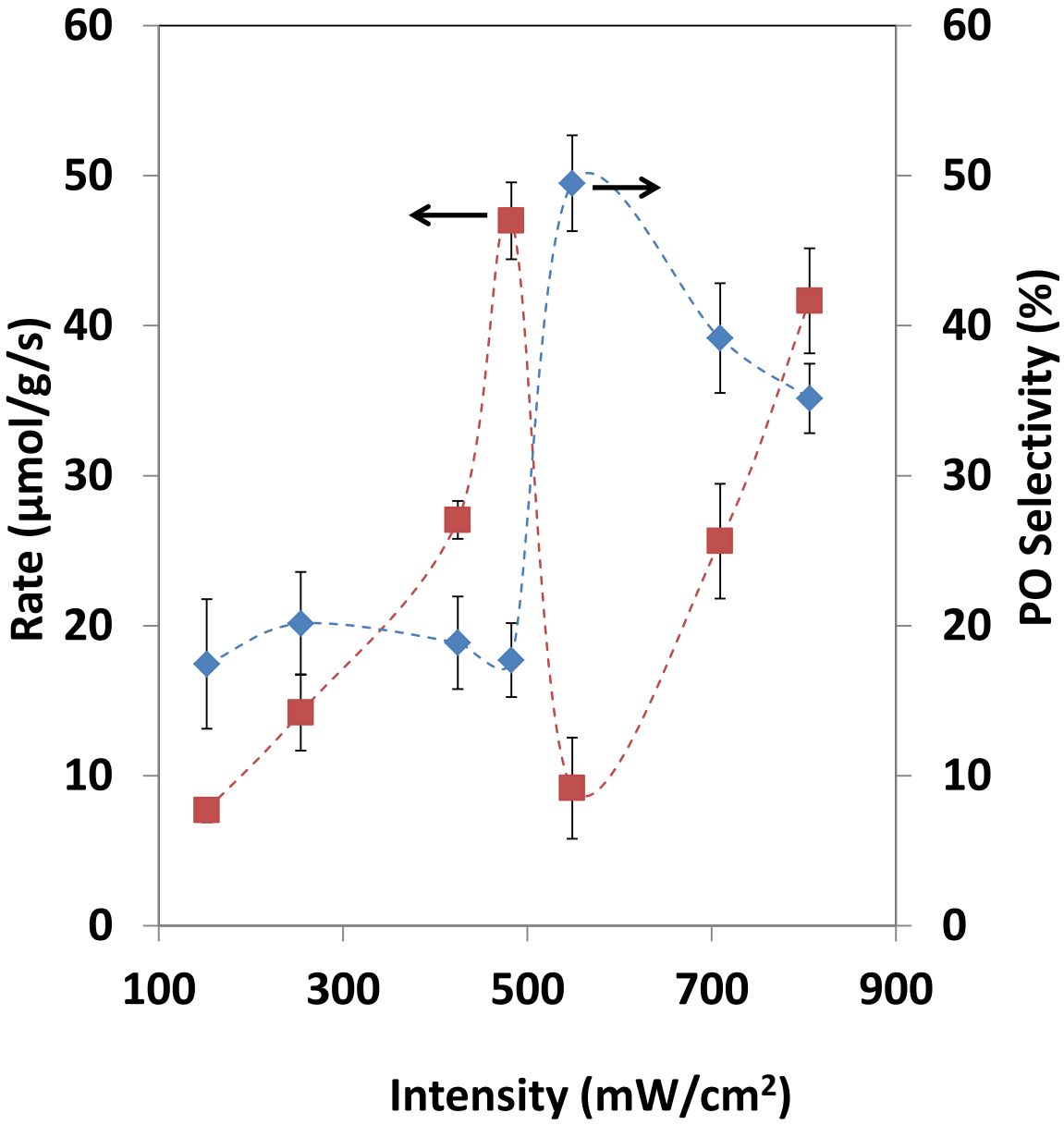

Figure 4.3.a Rate of propylene consumption (left axis, red squares) and the selectivity to PO (right axis, blue diamonds) under photothermal conditions (light on) at 473K as a function of light intensity. The rate and selectivity data shown in figure represent the average values of the data obtained from five independent experiments and the error bars represent the standard deviations.

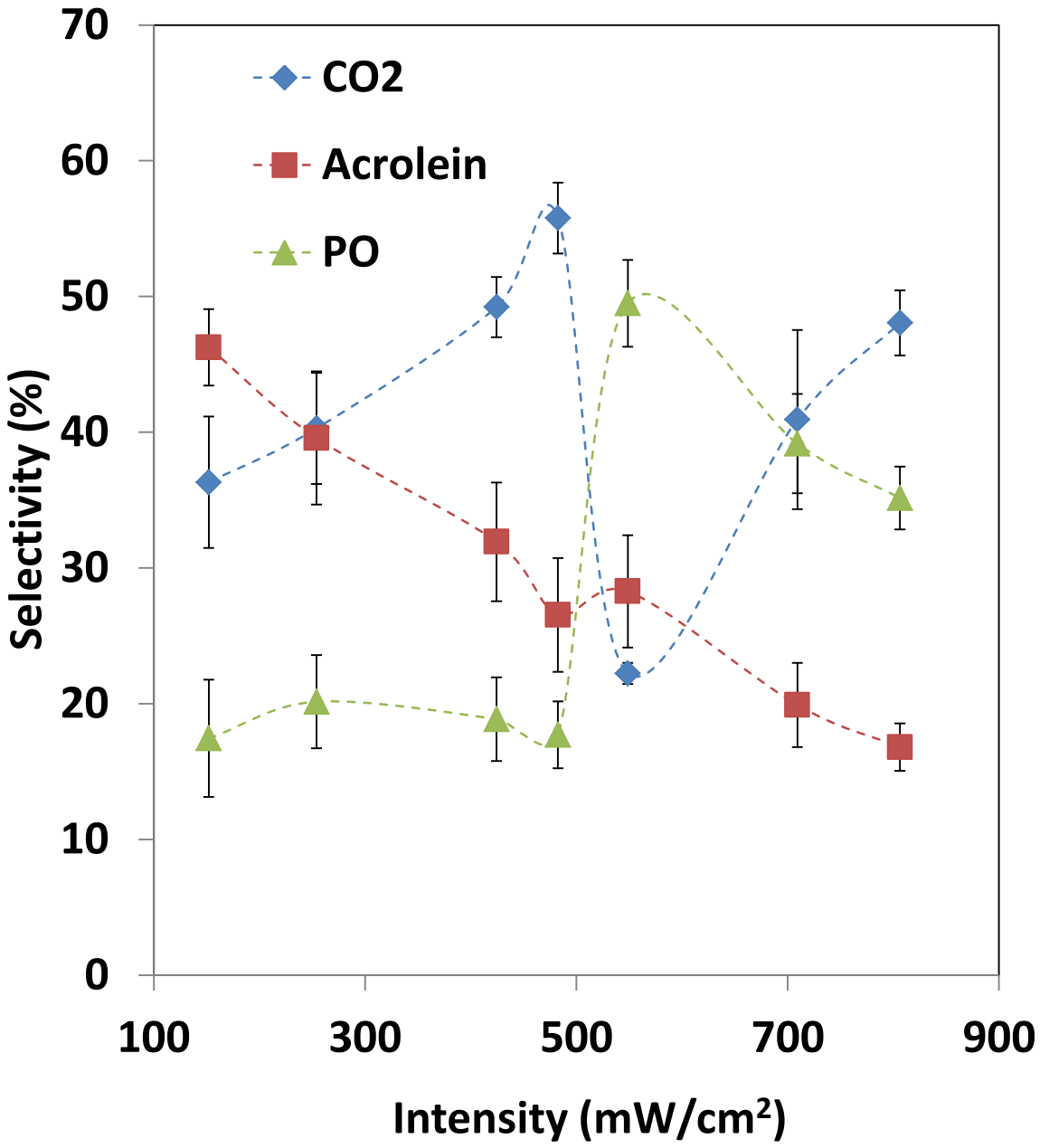

Figure 4.3.b. Selectivity to PO, acrolein and CO_2 under photothermal conditions at 473K as a function of light intensity. The selectivity data shown in the figure represent the average values of the data obtained from five independent experiments and the error bars represent the standard deviations.

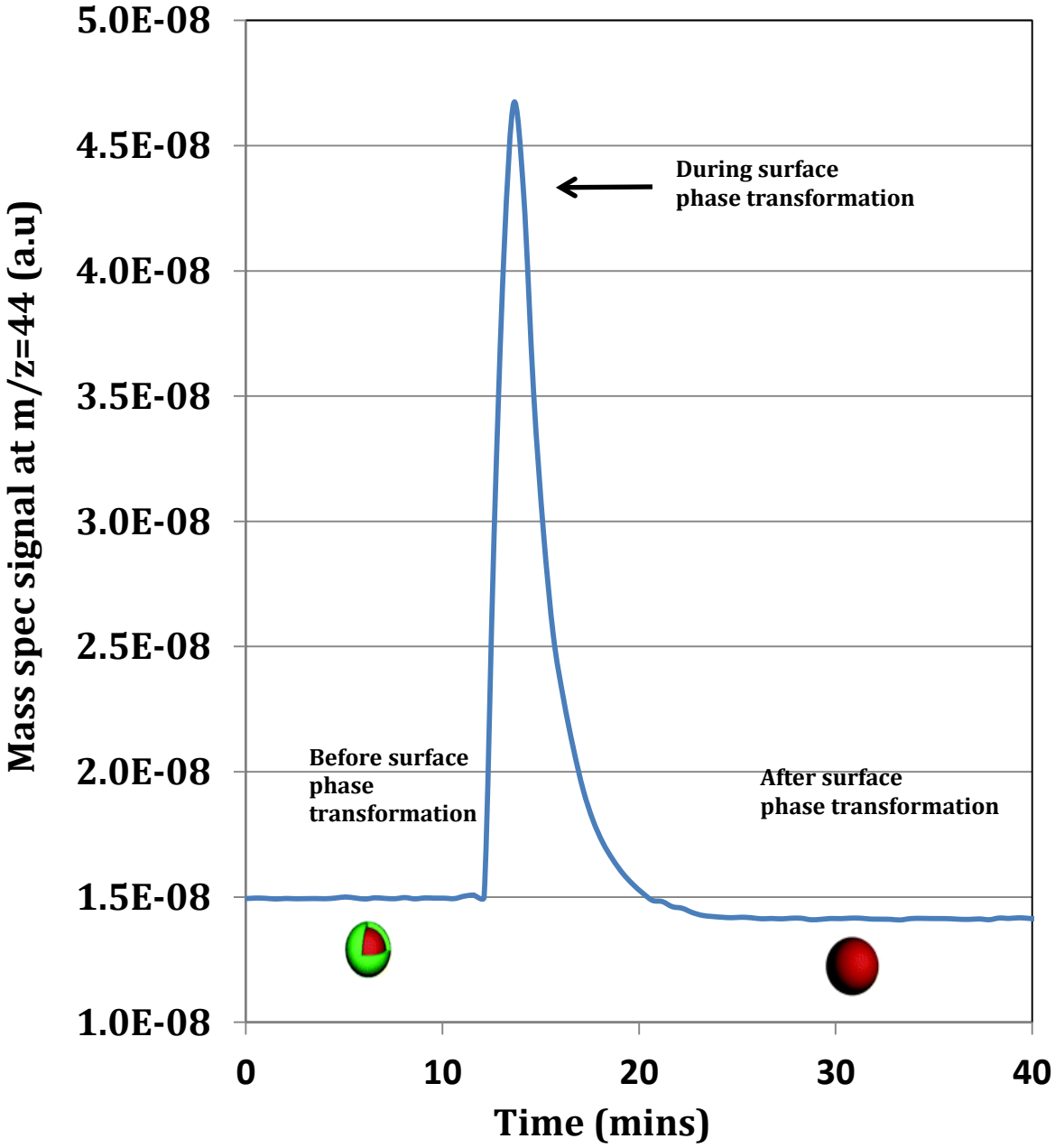

Figure 4.3.c. Transient MS signals observed at m/z=44 as a function of time during propylene epoxidation under photothermal conditions (light on) at 473K. When the light intensity was increased to threshold intensity of ~550 mW/cm^2 (at ~12 minutes in the figure), huge instantaneous change in the MS signal was observed before reaching the steady state signals (~25 minutes in the figure).

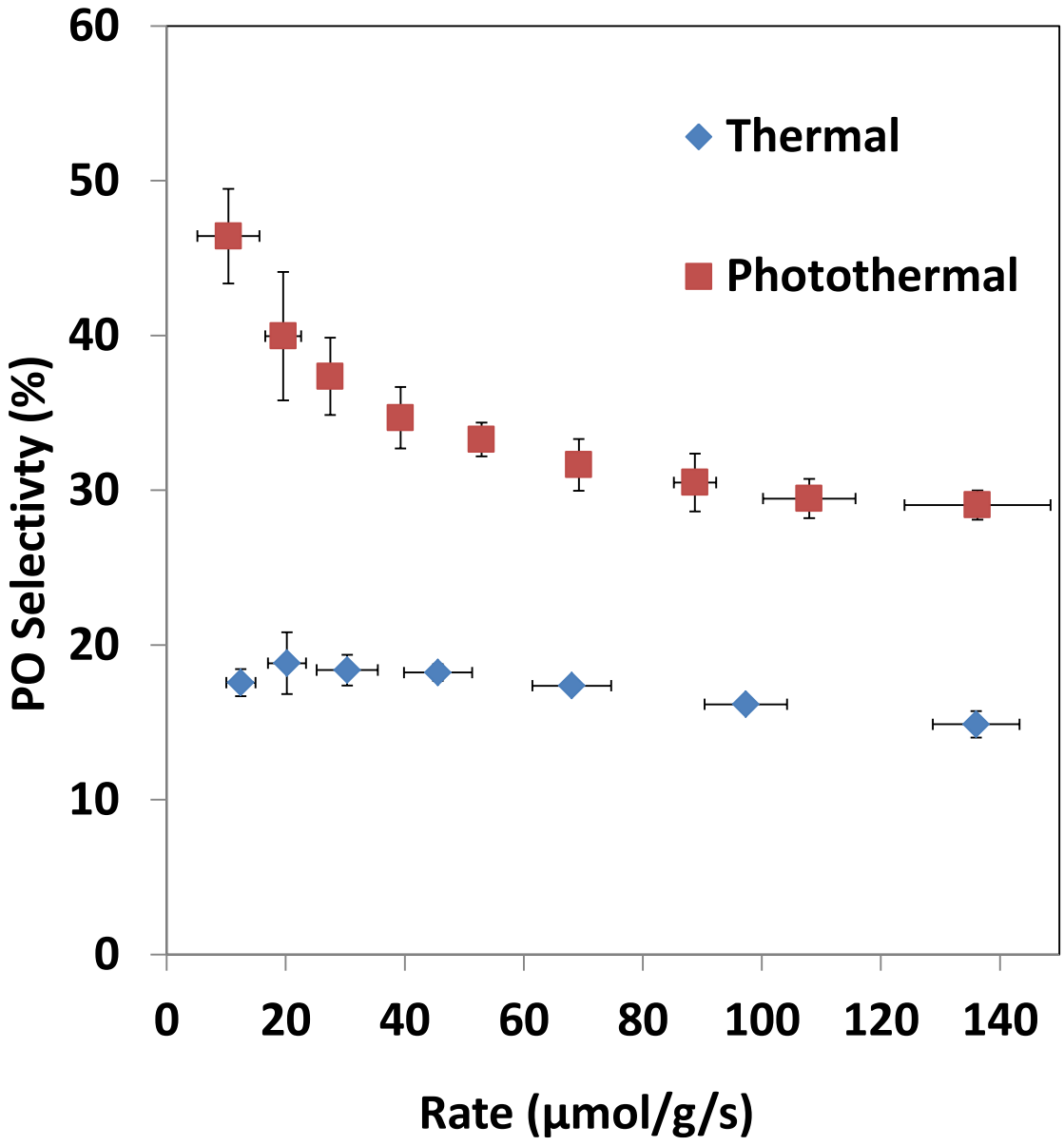

Figure 4.4.a. Selectivity to PO for thermal (light off) and photothermal (light on) processes as a function of the reaction rate. The light intensity used for the photothermal studies was 550 mW/cm^2. The reaction rate and selectivity data shown in the figure represent the average values of the data obtained from three independent experiments and the error bars represent the standard deviations.

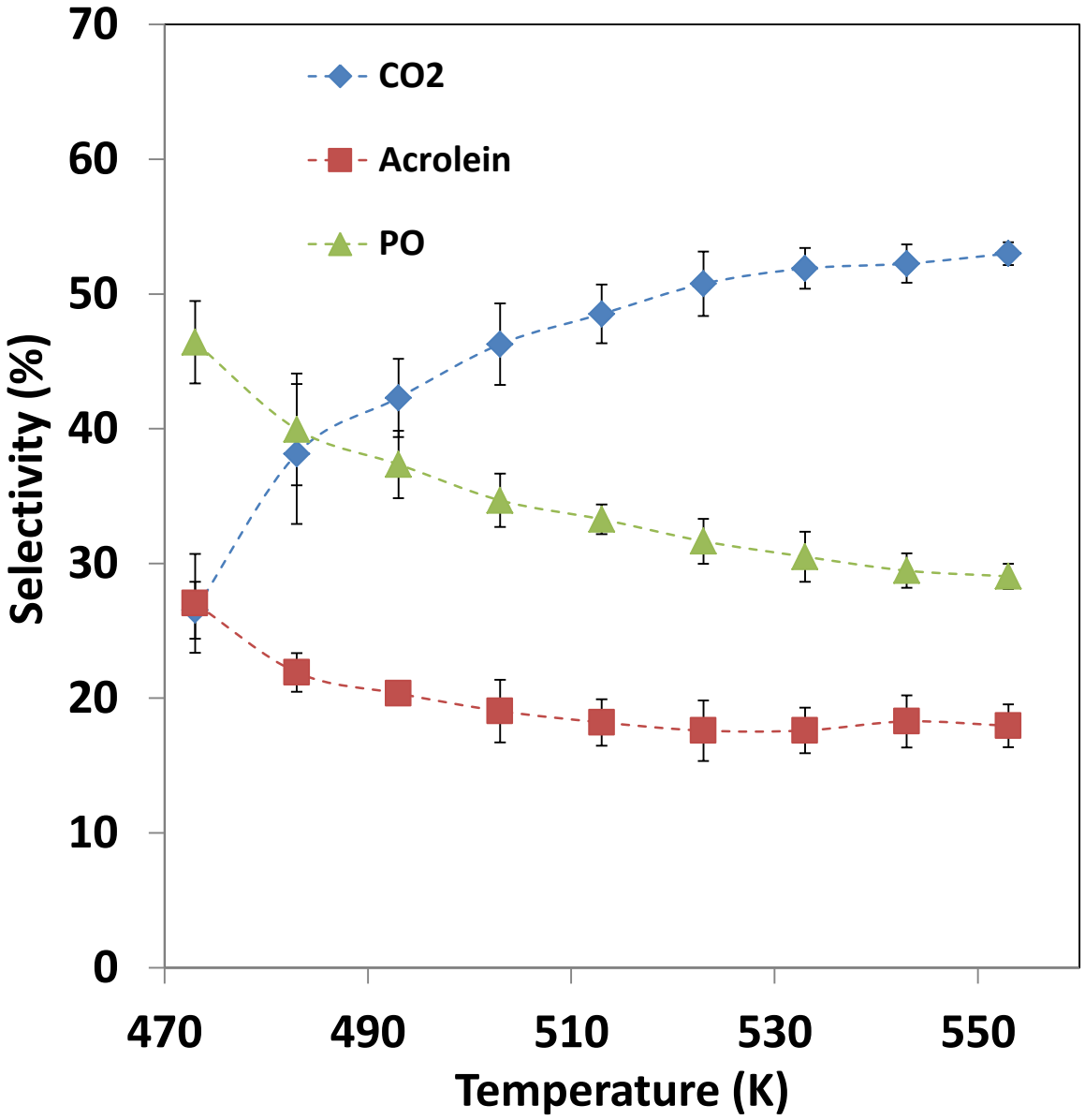

Figure. 4.4.b. Selectivity to PO, acrolein and CO_2 for photothermal (light on) process as a function of temperature. The light intensity used for the photothermal studies was 550 mW/cm^2. The selectivity data shown in the figure represent the average values of the data obtained from three independent experiments and the error bars represent the standard deviations.

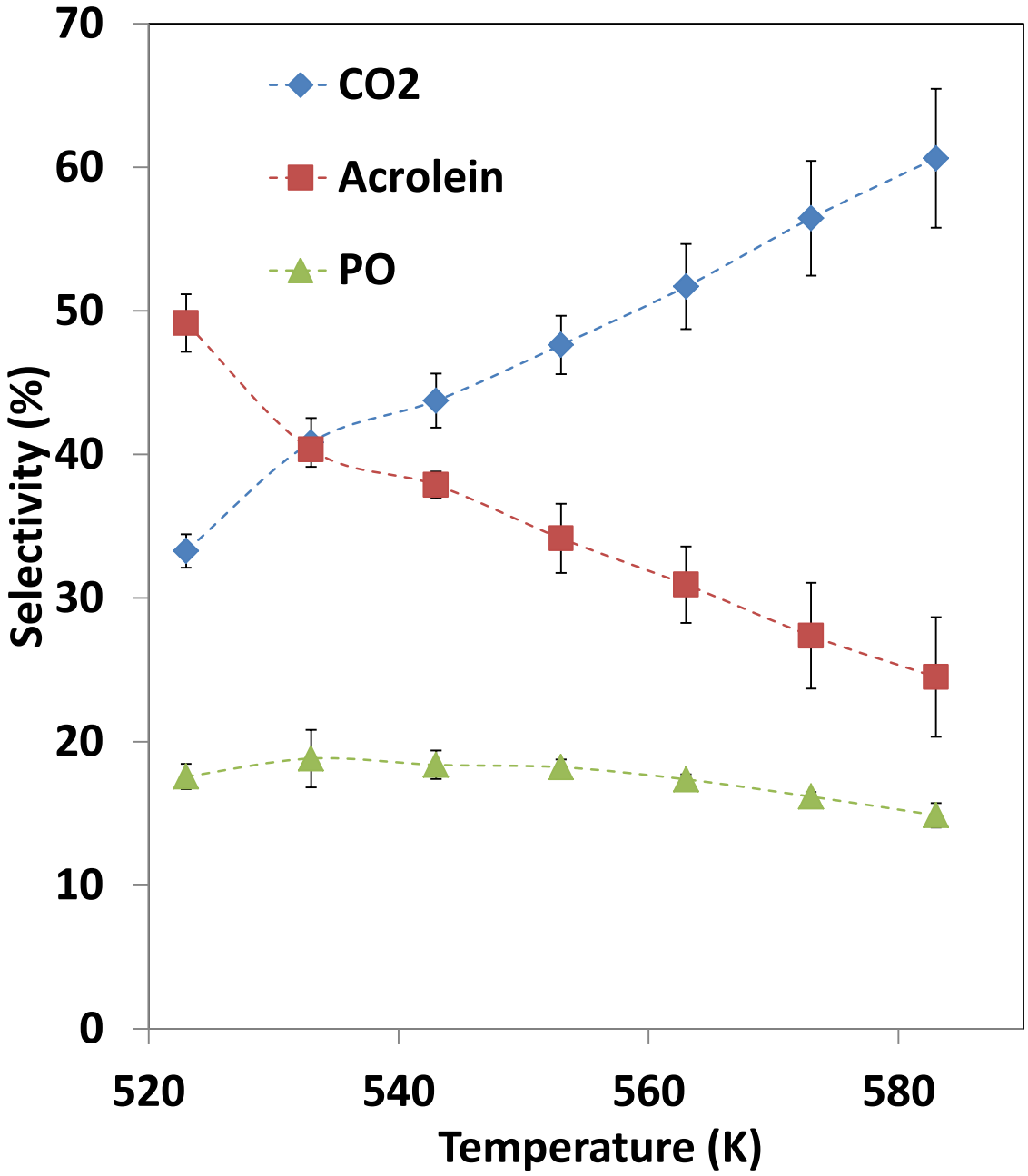

Figure 4.4.c. Selectivity to PO, acrolein and CO_2 under thermal conditions (light off) as a function of temperature. The selectivity data shown in the figure represent the average values of the data obtained from three independent experiments and the error bars represent the standard deviations.

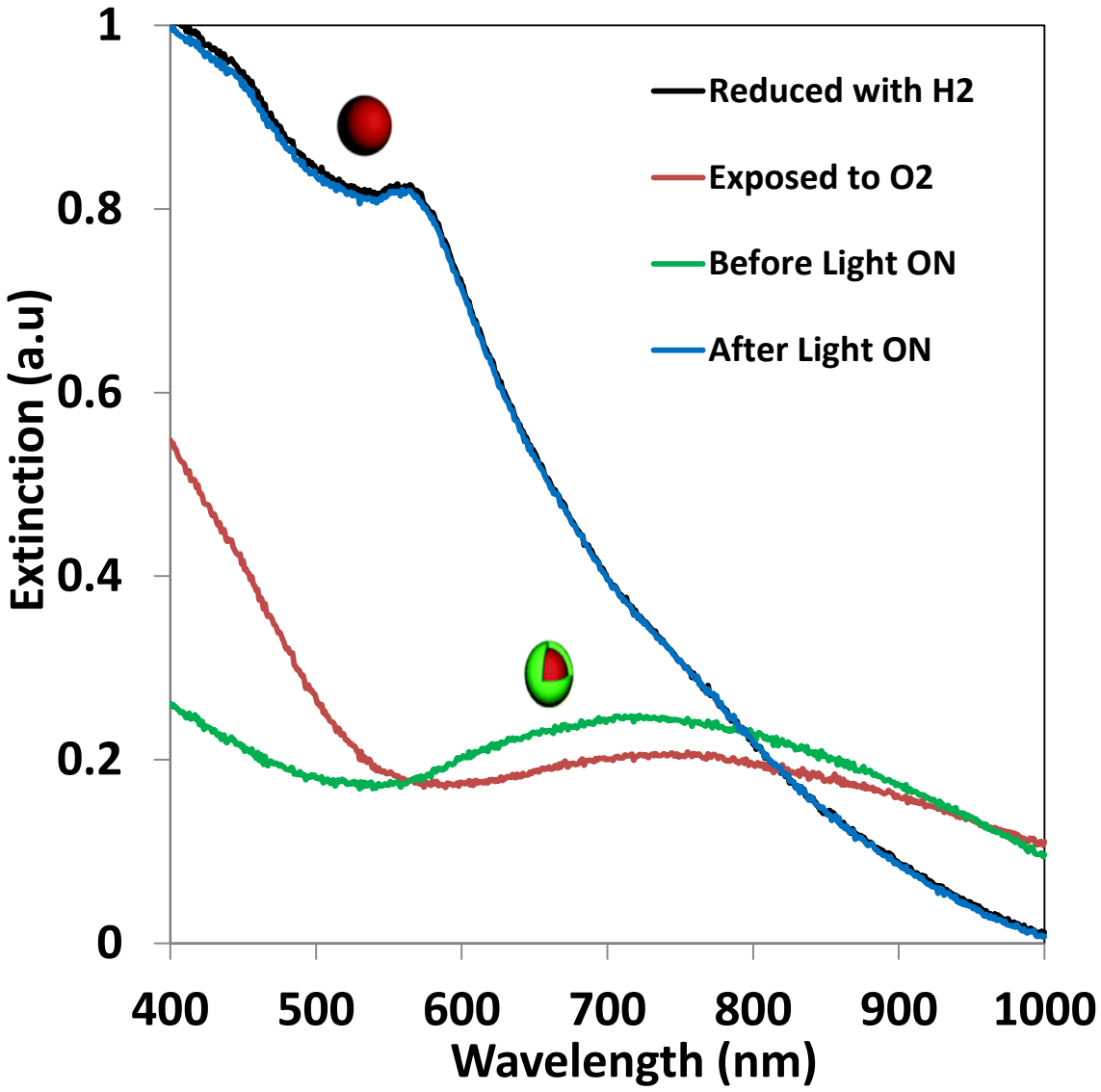

Figure 4.5.a. In situ diffuse reflectance ultraviolet-visible extinction spectra of the catalyst (2%Cu/SiO_2) reduced with hydrogen at 523 K, exposed to oxygen at 473K, under propylene epoxidation conditions without light (before light on) at 473 K, and under propylene epoxidation conditions with light on (after light on) at 473K. The light intensity used for the photothermal studies (after light on) was 550 mW/cm^2. The UV-Vis extinction spectra of the catalyst reduced with hydrogen and exposed to propylene oxidation under photothermal conditions (after light on) almost completely matched each other. To distinguish these two spectra, the extinction spectrum of the catalyst reduced with hydrogen was scaled by 1.01.

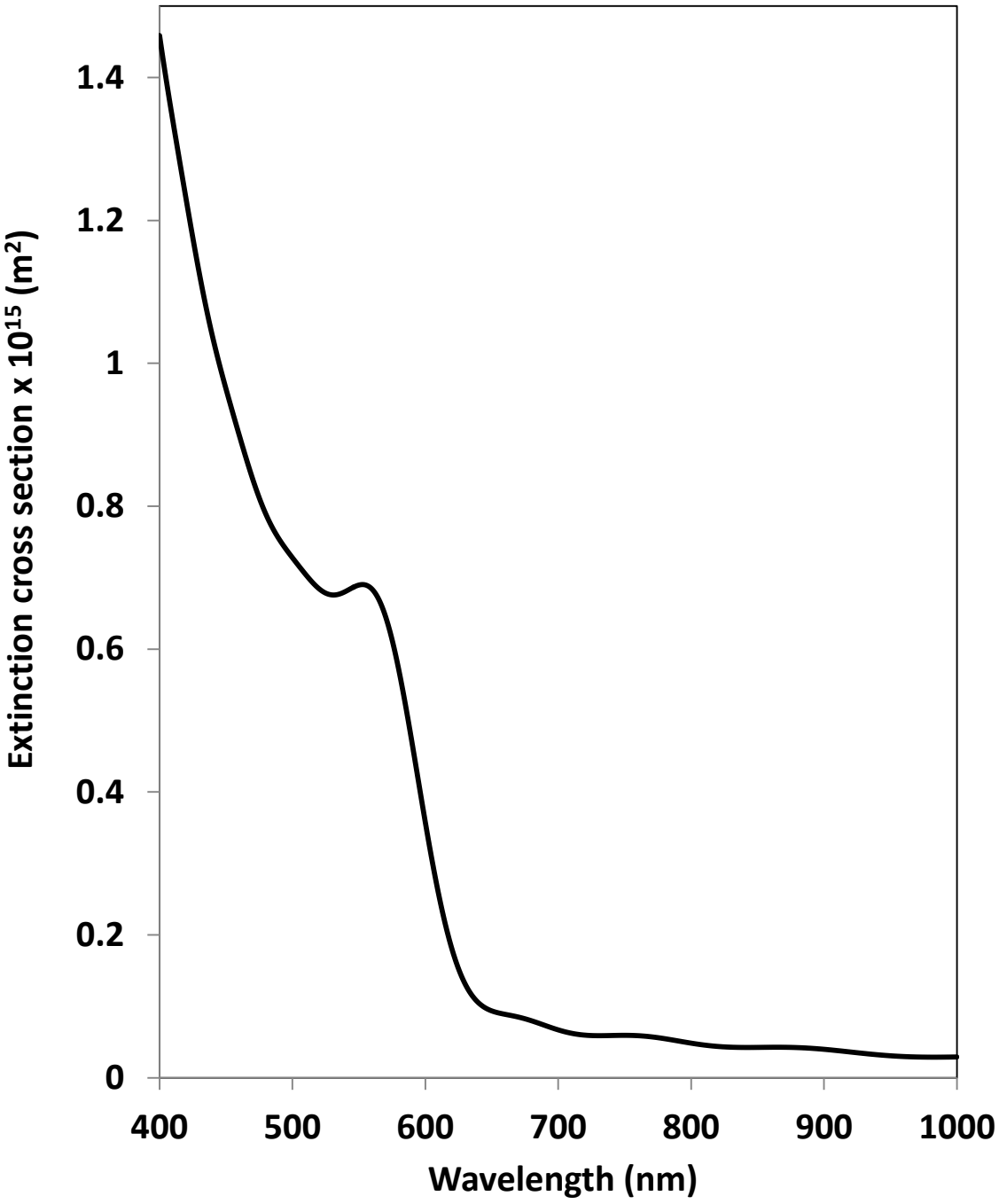

Figure 4.5.b. Extinction spectrum of copper spherical nanoparticle (41 nm) calculated from FDTD simulation.

The data also show that as the metallic Cu nanoparticles are exposed to 20% oxygen in helium at 473 K and atmospheric pressure, the SPR extinction peak is broadened and red shifted while the extinction intensity decreases. These changes in the extinction spectrum upon exposure of Cu nanoparticles to oxygen have been characterized, and it has been shown that they are the result of the formation of a shell of Cu_2O oxide on the metallic Cu core.[11,12] We note that due to the high sensitivity of Cu SPR to the local chemical environment, changes in the oxidation state of even a small fraction of Cu surface atoms are accompanied by significant changes in the extinction spectrum.[13–15] Figure 4.5.a also shows the UV-vis extinction spectrum of the functioning Cu catalyst at steady state conditions. These catalysts were first pre-reduced in H_2 and subsequently exposed to operating propylene epoxidation conditions. The data show that as the reactants, equimolar amounts of propylene and oxygen at atmospheric pressure, are introduced at 473 K, the UV-vis extinction spectrum changes from that associated with the metallic Cu to that of the oxidized Cu shell covering the metallic core. Subsequent illumination of the functioning Cu catalyst with UV-vis light of 550 mW/cm^2 intensity results in a dramatic transformation of the catalyst, manifested as the reduction of the Cu-oxide shell. As shown in Figure 4.3.a, this light-induced change in the chemical state of surface Cu atoms at 550 mW/cm^2 is accompanied by a dramatic increase in the PO selectivity and a drop in the reaction rate. The conclusion of the in-situ UV-vis extinction measurements were further supported by an ex-situ analysis of X-ray diffraction (XRD) patterns of the selective (light at threshold intensity, 550 mW/cm^2, after surface phase transformation) and unselective (light off) catalysts.

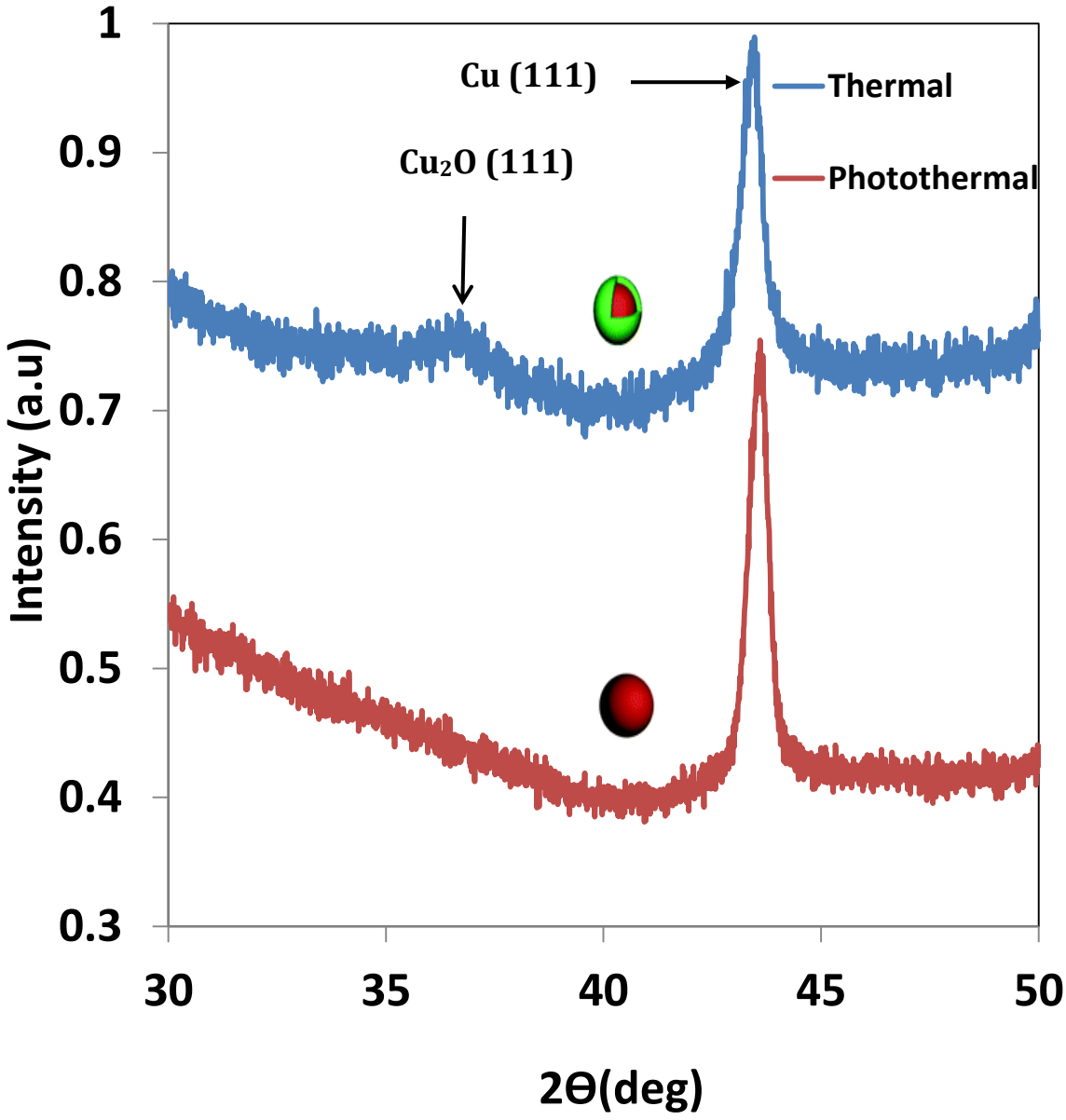

Figure 4.5.c. X-ray diffraction spectra for the catalyst used in thermal (light off) and photothermal (light on) studies. The light intensity used for the photothermal studies was 550 mW/cm^2. The arrows indicate the peak positions of Cu(111) and Cu_2O (111) signals.

Figure 4.5.c shows that the unselective catalysts exhibit diffraction features consistent with the presence of the Cu_2O shells on Cu, whereas the selective catalysts do not exhibit the oxide diffraction features.[11] To further explore the origin of the observed light-induced change in the oxidation state of the Cu catalysts and accompanying changes in the reaction rates and selectivity, we studied the behavior of illuminated, functioning Cu catalysts as a function of the wavelength of incident light. Multiple short and long pass optical filters were used to control the wavelength of light reaching the catalysts from the broadband visible light source. The total intensity of light reaching the catalyst was ~ 550 mW/cm^2 in all experiments and the operating temperature was 473 K. Figure 4.6.a shows that in the presence of 500 nm long pass filters (mainly light with wavelengths longer than 500 nm reaching the catalysts), the above-discussed surface transformation from oxidized Cu to metallic Cu takes place. On the other hand, as shown in Figure 4.6.b, when a 500 nm short pass filter is applied (mainly photons below 500 nm reaching the catalyst) the catalyst is oxidized under the reaction conditions and unperturbed by light. This result suggests a critical role for the Cu SPR in inducing the chemical transformation of Cu and driving the observed light-induced increase in the PO selectivity since photons with the wavelength below 500 nm do not excite the Cu SPR.

We propose that the photo-excitation of Cu SPR, associated with the metallic core of catalytic nanoparticles, serves to enhance the reduction of the Cu_2O shell and maintain the Cu surface in the metallic state under operating conditions.

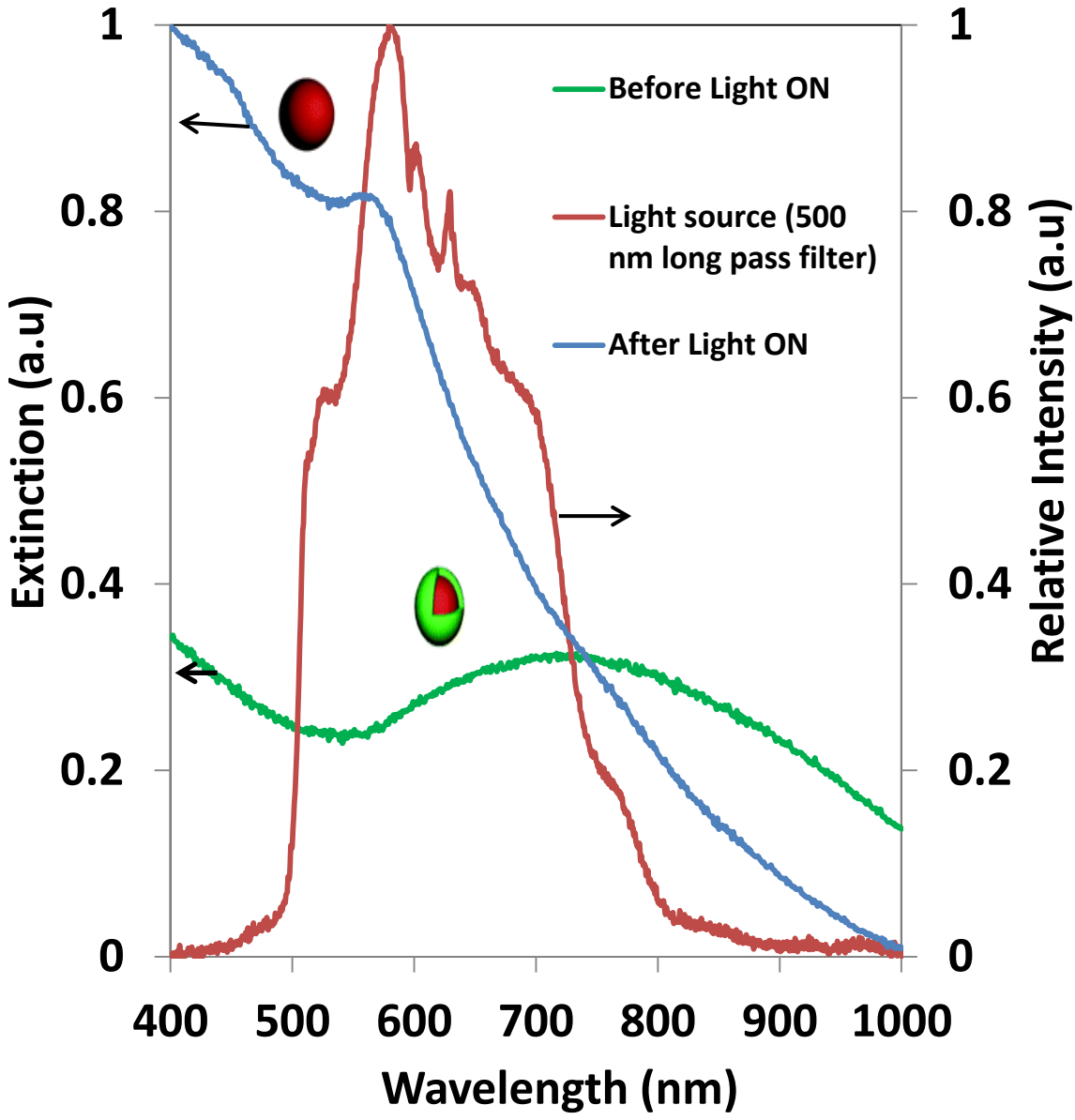

Figure. 4.6.a. Spectra of the light source with 500 nm long pass filter used in the photothermal studies, superimposed with diffuse reflectance ultraviolet-visible extinction spectra of catalyst (2%Cu/SiO_2) measured in-situ at 473K under thermal (before light on) and photothermal (after light on) conditions. The light intensity used for the photothermal studies was 550 mW/cm^2. a.u refers arbitrary unit.

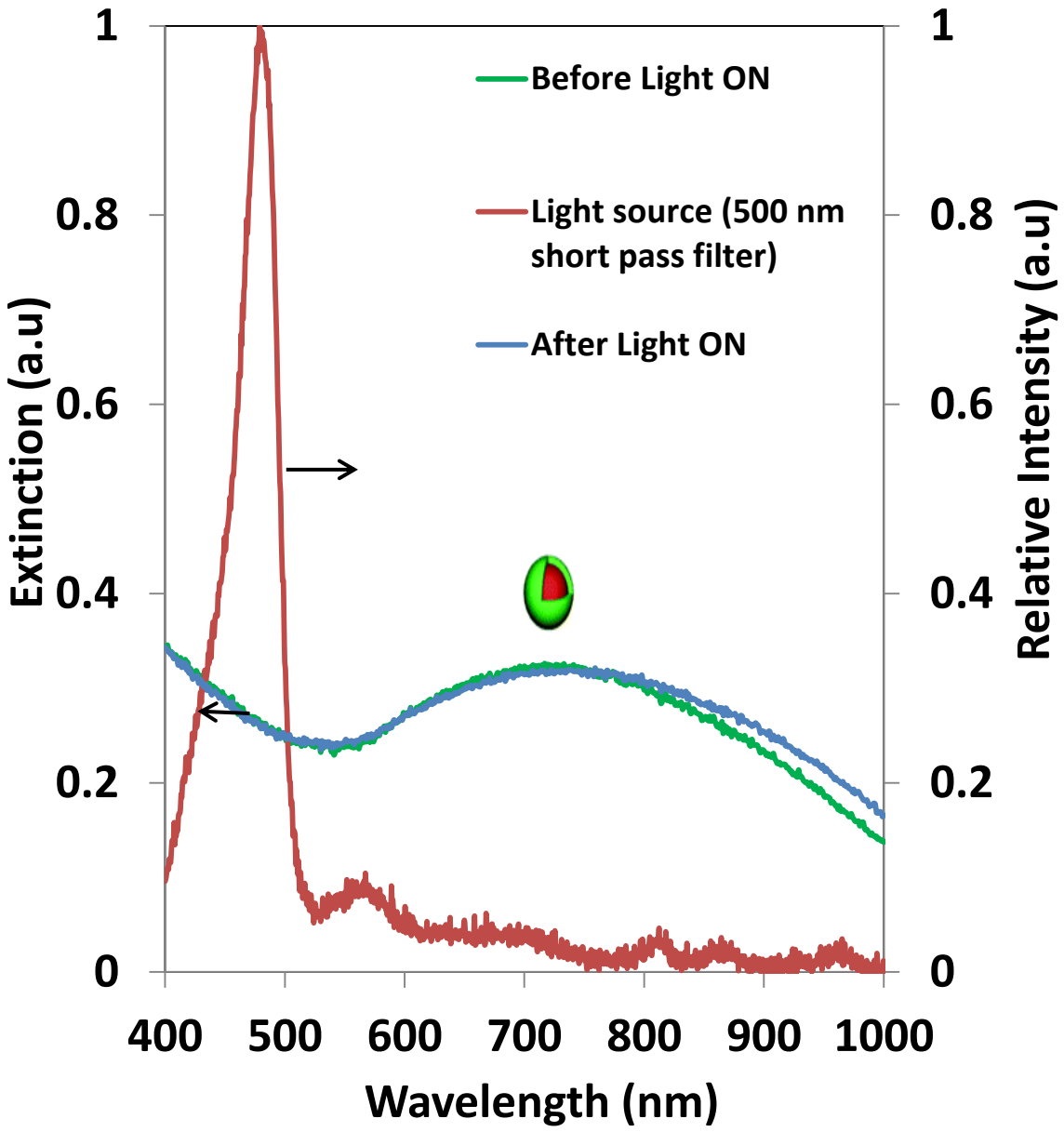

Figure. 4.6.b. Spectra of the light source with 500 nm short pass filter used in the photothermal studies, superimposed with diffuse reflectance ultraviolet-visible extinction spectra of catalyst (2%Cu/SiO_2) measured in-situ at 473K under thermal (before light on) and photothermal (after light on) conditions. The light intensity used for the photothermal studies was 550 mW/cm^2. a.u refers arbitrary unit.

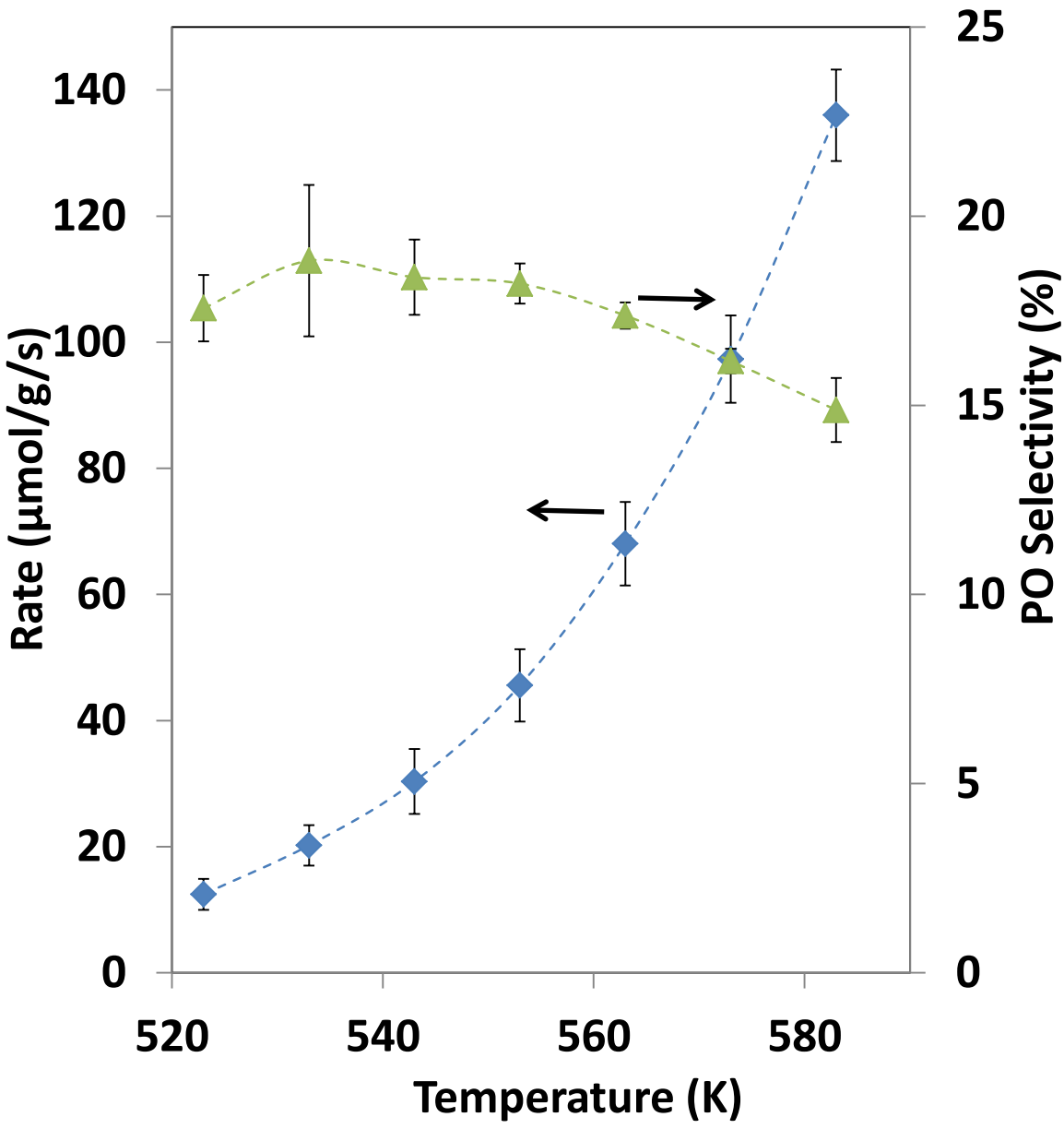

Figure 4.7. Rate of propylene oxidation (left axis, blue diamonds) and selectivity to PO (right axis, green triangles) under thermal conditions (light off) as a function of temperature. The rate and selectivity data shown in the figure represent the average values of the data obtained from three independent experiments and the error bars represent the standard deviations.

Cu_2O is a semiconductor with a band gap of ~ 2.0 eV.[16] There are two mechanisms by which Cu SPR could induce the reduction of Cu_2O. First, radiative energy transfer from the plasmon Cu states to the oxide shell enhances the rate of electron excitation from the valence (bonding orbitals) to conduction band (antibonding orbitals) of the Cu-oxide shell thereby weakening the Cu-O chemical bonds in the oxide. This plasmonic energy transfer from an excited plasmonic metal to a nearby semiconductor is well documented.[7,17–21] It takes place mainly via dipole-dipole interactions of intense SPR-mediated electromagnetic fields around the Cu metallic core with the oxide shell. In this mechanism, the metallic Cu core essentially traps light, locally amplifying its effect on the semiconductor.[7,17–21] Second, direct SPR-mediated transient injection of electrons from the metallic Cu core to the antibonding Cu-O orbitals of the oxide shell would also lead to a more facile reduction of Cu-oxide shell. The process has been shown to be functional in many systems where energetically accessible electronic states (orbitals) interact with metal SPR. The process of electron injection takes place either directly via chemical interface damping (CID)[7–9,22–26] of the metal plasmon states due to their interaction with the antibonding Cu-oxide states, or indirectly through the decay of plasmons into hot electrons[7–9,26–30] via Landau damping and subsequent transfer of the energetic electrons to Cu_2O. The observed broadening of SPR resonance upon the formation of the Cu-oxide shell (see Figure 4.5.a) is a clear indication that the imaginary component of the material dielectric function increases, which is direct evidence for the faster rates of SPR relaxation, most likely due to the direct injection of electrons into the oxide semiconductor.[22–25] Alternatively, the Cu SPR might

conceivably lead to heating of the Cu particles and their thermal reduction.[26] This mechanism is not likely because as shown in Figure 4.7, if we thermally heat the catalyst (light off), the reaction rate steadily increases and the PO selectivity steadily decreases as a function of temperature. This behavior is fundamentally different than the behavior observed in response to light (Figure 4.1.a), where we see sharp drops in the reaction rate and a sharp increase in the selectivity at ~ 550 mW/cm^2.

4.5. Conclusions

The studies discussed herein advance a number of critical concepts. First, though we focused on Cu nanostructures, the discussed mechanisms are universal and similar principles could be used in the design of various metal nano materials with photo-switchable oxidation states. For example, core-shell nanoparticles containing a plasmonic core (i.e., Au, Ag, Cu) and a shell of another metal could lend themselves to similar SPR-mediated photo-induced switching of the oxidation states of surface atoms. Controlling the oxidation state of functioning catalysts is critical for the control of reactant conversion rates and product selectivity. Second, direct epoxidation of propylene without expensive sacrificial agents is one of the most important processes for which no viable heterogeneous catalyst exists. While, the findings reported herein may pave the way towards the discovery of viable heterogeneous propylene epoxidation catalysts, hurdles related to efficient and scalable harvesting of light (including abundant solar light) represent considerable challenge.

4.6. References

(1) Cropley, R. L.; Williams, F. J.; Urquhart, A. J.; Vaughan, O. P. H.; Tikhov, M. S.; Lambert, R. M. Efficient Epoxidation of a Terminal Alkene Containing Allylic Hydrogen Atoms: trans-Methylstyrene on Cu{111}. J. Am. Chem. Soc. 2005, 127, 6069–6076.

(2) Santra, A. K.; Cowell, J. J.; Lambert, R. M. Ultra-selective epoxidation of styrene on pure Cu{111} and the effects of Cs promotion. Catal. Lett. 2000, 67, 87–91.

(3) Cowell, J. J.; Santra, A. K.; Lambert, R. M. Ultraselective Epoxidation of Butadiene on Cu{111} and the Effects of Cs Promotion. J. Am. Chem. Soc. 2000, 122, 2381–2382.

(4) Lambert, R. M.; Williams, F. J.; Cropley, R. L.; Palermo, A. Heterogeneous alkene epoxidation: past, present and future. J. Mol. Catal. A: Chem. 2005, 228, 27–33.

(5) Torres, D.; Lopez, N.; Illas, F.; Lambert, R. M. Low-Basicity Oxygen Atoms: A Key in the Search for Propylene Epoxidation Catalysts. Angew. Chem. Int. Ed. 2007, 46, 2055–2058.

(6) Monnier, J. R.; Hartley, G. W. Comparison of Cu and Ag Catalysts for Epoxidation of Higher Olefins. J. Catal. 2001, 203, 253–256.

(7) Linic, S.; Christopher, P.; Ingram, D. B. Plasmonic-metal nanostructures for efficient conversion of solar to chemical energy. Nat. Mater. 2011, 10, 911–921.

(8) Christopher, P.; Xin, H.; Linic, S. Visible-light-enhanced catalytic oxidation reactions on plasmonic silver nanostructures. Nat. Chem. 2011, 3, 467–472.

(9) Christopher, P.; Xin, H.; Marimuthu, A.; Linic, S. Singular characteristics and unique chemical bond activation mechanisms of photocatalytic reactions on plasmonic nanostructures. Nat. Mater. 2012, 11, 1044-1050.

(10) Vaughan, O. P. H.; Kyriakou, G.; Macleod, N.; Tikhov, M.; Lambert, R. M. Copper as a selective catalyst for the epoxidation of propene. J. Catal. 2005, 236, 401–404.

(11) Rice, K. P.; Walker, E. J.; Stoykovich, M. P.; Saunders, A. E. Solvent-Dependent Surface Plasmon Response and Oxidation of Copper Nanocrystals. J. Phys. Chem. C 2011, 115, 1793–1799.

(12) Chan, G. H.; Zhao, J.; Hicks, E. M.; Schatz, G. C.; Van Duyne, R. P. Plasmonic Properties of Copper Nanoparticles Fabricated by Nanosphere Lithography. Nano Lett. 2007, 7, 1947–1952.

(13) Larsson, E. M.; Langhammer, C.; Zorić, I.; Kasemo, B. Nanoplasmonic Probes of Catalytic Reactions. Science 2009, 326, 1091–1094.

(14) Seo, D.; Park, G.; Song, H. Plasmonic Monitoring of Catalytic Hydrogen Generation by a Single Nanoparticle Probe. J. Am. Chem. Soc. 2012, 134, 1221–1227.

(15) Novo, C.; Funston, A. M.; Mulvaney, P. Direct observation of chemical reactions on single gold nanocrystals using surface plasmon spectroscopy. Nat. Nanotechnol. 2008, 3, 598–602.

(16) Hara, M.; Kondo, T.; Komoda, M.; Ikeda, S.; Kondo, J. N.; Domen, K.; Hara, M.; Shinohara, K.; Tanaka, A. Cu_2O as a photocatalyst for overall water splitting under visible light irradiation. Chem. Commun. 1998, 357–358.

(17) Cushing, S. K.; Li, J.; Meng, F.; Senty, T. R.; Suri, S.; Zhi, M.; Li, M.; Bristow, A. D.; Wu, N. Photocatalytic Activity Enhanced by Plasmonic Resonant Energy Transfer from Metal to Semiconductor. J. Am. Chem. Soc. 2012.

(18) Christopher, P.; Ingram, D. B.; Linic, S. Enhancing Photochemical Activity of Semiconductor Nanoparticles with Optically Active Ag Nanostructures: Photochemistry Mediated by Ag Surface Plasmons. J. Phys. Chem. C 2010, 114, 9173–9177.

(19) Ingram, D. B.; Linic, S. Water Splitting on Composite Plasmonic-Metal/Semiconductor Photoelectrodes: Evidence for Selective Plasmon-Induced Formation of Charge Carriers near the Semiconductor Surface. J. Am. Chem. Soc. 2011, 133, 5202–5205.

(20) Ingram, D. B.; Christopher, P.; Bauer, J. L.; Linic, S. Predictive Model for the Design of Plasmonic Metal/Semiconductor Composite Photocatalysts. ACS Catal. 2011, 1, 1441–1447.

(21) Awazu, K.; Fujimaki, M.; Rockstuhl, C.; Tominaga, J.; Murakami, H.; Ohki, Y.; Yoshida, N.; Watanabe, T. A Plasmonic Photocatalyst Consisting of Silver Nanoparticles Embedded in Titanium Dioxide. J. Am. Chem. Soc. 2008, 130, 1676–1680.

(22) Kreibig, U.; Vollmer, M. Optical Properties of Metal Clusters; 1st ed.; Springer, 1995.

(23) Persson, B. N. J. Polarizability of small spherical metal particles: influence of the matrix environment. Surf. Sci. 1993, 281, 153–162.

(24) Kreibig, U. Interface-induced dephasing of Mie plasmon polaritons. Appl. Phys. B 2008, 93, 79–89.

(25) Hövel, H.; Fritz, S.; Hilger, A.; Kreibig, U.; Vollmer, M. Width of cluster plasmon resonances: Bulk dielectric functions and chemical interface damping. Phys. Rev. B: Condens. Matter 1993, 48, 18178–18188.

(26) Watanabe, K.; Menzel, D.; Nilius, N.; Freund, H.-J. Photochemistry on Metal Nanoparticles. Chem. Rev. 2006, 106, 4301–4320.

(27) Brus, L. Noble Metal Nanocrystals: Plasmon Electron Transfer Photochemistry and Single-Molecule Raman Spectroscopy. Acc. Chem. Res. 2008, 41, 1742–1749.

(28) Michaels, A. M.; Jiang; Brus, L. Ag Nanocrystal Junctions as the Site for Surface-Enhanced Raman Scattering of Single Rhodamine 6G Molecules. J. Phys. Chem. B 2000, 104, 11965–11971.

(29) Furube, A.; Du, L.; Hara, K.; Katoh, R.; Tachiya, M. Ultrafast Plasmon-Induced Electron Transfer from Gold Nanodots into TiO_2 Nanoparticles. J. Am. Chem. Soc. 2007, 129, 14852–14853.

(30) Tian, Y.; Tatsuma, T. Plasmon-induced photoelectrochemistry at metal nanoparticles supported on nanoporous TiO_2. Chem. Commun. 2004, 1810.

CHAPTER 5

Effect of sulfuration on the performance of Ag cube catalysts for the epoxidation of ethylene

5.1. Summary

Achieving high selectivity towards the desired product is important in heterogeneous catalysis to design environmentally friendly and energy efficient processes. In this chapter, we show that the catalysts containing sulfurized Ag cubes treated with low concentration polysulfide (Na_2S_x) solution exhibit better performance in terms of catalytic activity and selectivity towards the desired product compared to pure Ag cube catalysts during the ethylene oxidation reaction. We demonstrate that the removal of polymeric capping agent (polyvinylpyrrolidone, PVP) from the surface of Ag cubes is critical and the PVP removal by the polysulfide solution is mainly responsible for the improved performance observed with this sulfurized Ag cubes catalyst.

5.2. Introduction

Developing energy efficient and environmentally friendly chemical transformation processes is important for combating dwindling natural resources and growing environmental concerns.[1–4] Ethylene oxide (EO) is an extremely

valuable commodity chemical that is commercially produced from the epoxidation of ethylene using oxygen as an oxidizing agent over α-Al_2O_3 supported silver-based catalysts.[3] The quasi-spherical silver particles supported on α-Al_2O_3, synthesized using standard incipient wetness methods, achieve ethylene selectivity to EO of ~45%.[3] Approximately 55% of the ethylene undergoes combustion to form undesired byproducts, carbon dioxide (CO_2) and water (H_2O), over this monometallic silver catalyst. The production of these byproducts is highly exothermic and the heat released during the combustion of ethylene impacts process operability.[3] The combined issues of heat management and CO_2 emissions, along with the need to efficiently use the ethylene feedstock, have motivated continuing research efforts aimed at improving the performance of silver-based catalysts and developing novel materials with improved EO selectivity.[3] As a result of sustained research over the years, it has been shown that the silver catalysts promoted with cesium and chlorine in the form of 1,2-dichloroethane, which is added continuously to the reactor as co-feed, exhibit ethylene selectivity to EO over ~80%.[3]

Recently another strategy based on well-defined silver (Ag) nanostructures has been reported in the literature to achieve high ethylene selectivity to EO (e.g., ~80% over Ag nanocube catalysts) without using any sacrificial agents or co-feed.[5–7] The studies of shape-dependent catalytic performance of Ag nanostructures have shown higher EO selectivity with catalysts containing Ag nanocubes, dominated by Ag (100) surface facets, compared to conventional Ag catalysts containing quasi-spherical particles, dominated by Ag (111) surface facets.[6] It has been shown from

density functional theory calculations that Ag (100) surface facet is inherently more selective towards EO than Ag (111) surface facet.[5] For a given Ag particle shape, higher EO selectivity have been reported over larger particles.[6] It has been proposed that the under-coordinated surface sites (corners and edges of the particle) of Ag nanocatalysts activate unselective pathway, combustion of ethylene to CO_2 and H_2O, during the ethylene oxidation.[6] Thus, the higher selectivity of larger Ag nanoparticles compared to smaller sized particles are attributed to lower concentration of under-coordinated Ag surface sites in larger particles.[6]

Although the catalysts containing Ag cubes dominated by (100) facets have shown high selectivity towards the desired product in ethylene epoxidation, the long-term stability of the catalyst under reaction condition still remains a critical challenge. This problem is due to the presence of sharp corners on the surface of Ag cubes, thus rendering them thermodynamically unstable.[8] Under reaction conditions Ag cubes are expected to evolve into the lowest energy structures, which are Ag spheres dominated by (111) facets.[8] It has been reported that EO selectivity of Ag cube catalysts exhibit a drop of 2 to 3% over a reaction time of 48 hours as the morphology of cubes changes to expose the less selective (111) facets.[6] Recently Xia and coworkers have demonstrated a strategy to preserve the shape of Ag nanostructures through selective sulfuration of the sharp corners using polysulfide solution (Na_2S_x).[8] They have reported that Ag triangular nanoplates and nanocubes undergo change to their morphology by rounding their sharp corners into circular discs and spheres, respectively, when they are aged in water at 100^0C for 12 hrs.[8] Furthermore, they have demonstrated that these Ag nanostructures, with their

sharp corners selectively sulfurized into Ag_2S, retain their shape under the same aging conditions.[8]

The objectives of our work in this chapter are to (i) selectively sulfurize the corner sites of silver cubes using polysulfide solution, and (ii) compare the performance of these sulfurized silver cubes with pure silver cube catalysts for the ethylene epoxidation reaction. Our hypothesis is that selective poisoning of the unselective corner sites of silver cubes with sulfur could result in higher EO selectivity and relatively better catalyst stability compared to pure cubes.

5.3. Methods

5.3.1. Preparation of catalyst

Silver (Ag) nanocubes were prepared using solution based modified-polyol process reported previously.[6,9–12] Silver nitrate, $AgNO_3$ (99%, Sigma), ethylene glycol (E.G, 99%, J.T. Baker), PVP (55,000 MW, Sigma) and HCl (30mM) were used as a precursor, reducing agent and solvent, capping agent, and etching agent, respectively. For a typical synthesis in solution, 5ml of E.G in 20 ml glass vial, which was submerged in heating oil bath on a stirring hot plate, was heated to 140-145 ^{0}C for 1 hour. After 1 hour, 100 μL of 30 mM HCl solution was added, and was allowed for 10 minutes for complete mixing. 3 ml each of 0.1M $AgNO_3$ and 0.15M of PVP were injected simultaneously into the reaction mixture using a two-channel syringe pump at a constant flow rate of 0.75 ml/min. Throughout the process, except in final growth step, the cap of the vial was loosely placed to allow air into the reaction mixture. The reaction mixture was allowed for 14-16 hours for the nucleation step.

The reaction mixture was then allowed for 1-2 hours for the final growth step. The as-synthesized nanoparticles were split equally into two samples. One sample was washed by centrifugation in acetone for three times and then in a mixture of acetone and water (2/3 ratio by volume) for two times, and were labeled as Ag cubes. Another sample was washed by centrifugation in acetone for three times, redispersed in water, then treated with polysulfide (Na_2S_x) solution for sulfuration, and washed by centrifugation in a mixture of acetone and water (2/3 ratio by volume) for two times and were labeled as sulfurized Ag cubes. The resulting nanoparticles (Ag cubes and sulfurized Ag cubes) were then sonicated and redispersed in ethanol. A known amount of support material, α-Al_2O_3, was added to the silver nanoparticles (Ag cubes or sulfurized Ag cubes) dispersed in ethanol to prepare catalyst with final composition of ~20 wt % Ag/α-Al_2O_3. The mixture was sonicated for 1 hour, dried in an oven at ~70^0C for 14 hours, and used as catalyst.

5.3.2. Sulfuration of Ag cubes

The Ag cubes were sulfurized using the procedure reported in the literature previously.[8,13,14] For a sulfuration reaction, polysulfide (Na_2S_x) solution was used as a source of sulfur. The polysulfide solution was prepared by reacting 11.7 ml of aqueous solution of 50 mM sodium sulfide (Na_2S) with 32 mg of sulfur powder at 80^0C in an oven for ~14 hours. The resulting polysulfide solution was diluted ten times with distilled water and used for sulfuration. In a typical sulfuration reaction, a known volume of polysulfide (Na_2S_x) solution was added to 30 ml of Ag cubes dispersed in water and allowed to react for 15 minutes at room temperature under

magnetic stirring. The sulfurized Ag cubes were washed by centrifugation in a mixture of acetone and water (2/3 ratio by volume) for two times, then sonicated and redispersed in ethanol for the catalyst preparation.

5.3.3. Reactor studies

The reactions were performed in a vertically oriented packed bed reactor (Harrick High Temperature Reaction Chamber) that allowed temperature control through electrical heating.[15,16] The catalyst (packed) bed was prepared by loading 10 mg of inert silica beads (Silica gel, Sigma-Aldrich Cat. No. 214418) to the bottom of the reactor and 25 mg of 20 wt% Ag/α-Al_2O_3 catalysts on top of the layers of silica beads. The catalysts were pretreated at 270^0C for 5 hours in 25% oxygen (remaining nitrogen) at a total flow rate of 80 cm^3/min (sccm) to remove polymeric capping agents (PVP) through their combustion. The reactants with a composition of 20% ethylene and 20% oxygen (remaining nitrogen) at a total flow rate of 100 cm^3/min were then introduced to the catalyst bed at 270^0C, and left overnight to remove remaining PVP, and to reach steady state. The catalysts were then exposed to the specified reaction temperature (220^0C or 230^0C). The reactants and products were analyzed online using a gas chromatography (Varian CP 3800) equipped with thermal conductivity and flame ionization detectors. The rate and selectivity results reported here were measured in a differential reactor set-up in the regime limited by the reaction kinetics. Ethylene oxide (EO) and carbon dioxide (CO_2) were observed as the principal products. The reaction rates were calculated using the rate of product formation, i.e., the reaction rates of ethylene consumption were

calculated using the formula, (r_{EO}+r_{CO2}/2), where, r_{EO} and r_{CO2} denote the measured rate of the products- EO and CO_2, respectively. The EO selectivity was calculated using the formulae, r_{EO}/(r_{EO} +r_{CO2}/2).

5.3.4. Characterization of Ag cubes and sulfurized Ag cubes

UV-Vis extinction spectra of Ag cubes and sulfurized Ag cubes were measured using Thermo Scientific Evolution 300 UV-Vis Spectrophotometer. The scanning electron microscope (SEM) image was obtained using an FEI Nova 200 Nanolab. X-ray photoelectron spectroscopy (XPS) spectra of Ag cubes and sulfurized Ag cubes were acquired using Kratos Axis Ultra XPS system with 150 W monochromatic Al source.

5.4. Results and discussion

To monitor the extent of sulfuration on Ag cubes for different concentrations of polysulfide solutions, we used ultraviolet-visible (UV-vis) extinction spectroscopy. Because of the high sensitivity of surface plasmon resonance (SPR) to the local chemical environment, sulfuration of Ag surface atoms can be monitored by changes in the UV-vis extinction spectrum.[17–19] In Figure 5.1, we show the UV-vis extinction spectra of aqueous suspensions of Ag cubes and sulfurized Ag cubes treated with different amounts of polysulfide solutions. It is worth mentioning here that, for a given polysulfide solution concentration, the sulfuration reaction was completed within 15 minutes as monitored by change in shape of the extinction spectrum. The extinction spectra of sulfurized Ag cubes shown in Figure 5.1 were thus measured 15 minutes after the addition of polysulfide solution.

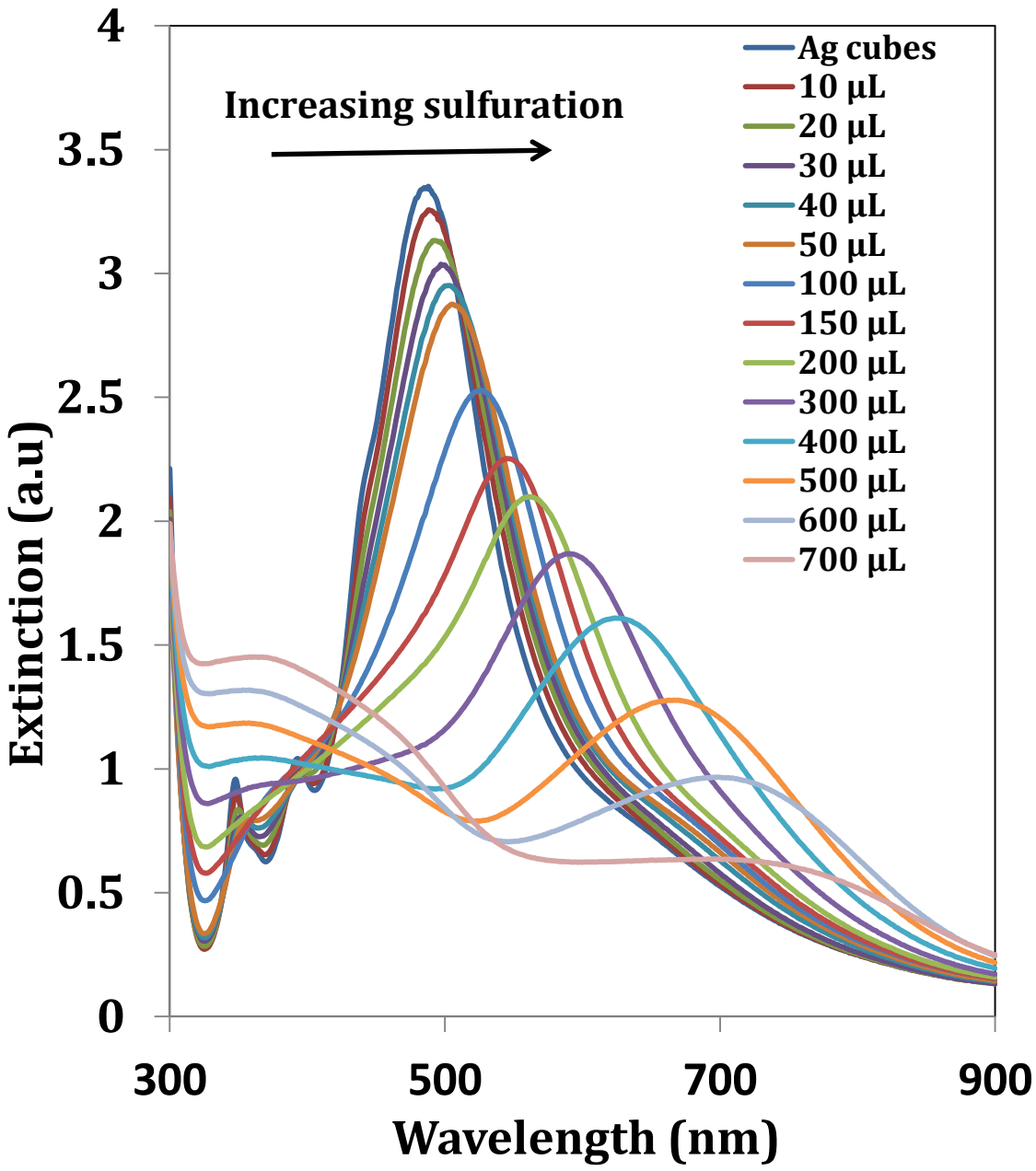

Figure 5.1.a. UV-vis extinction spectra of pure cubes and sulfurized cubes treated with different amounts of polysulfide solution. Figure legends show the amount (volume, µL) of polysulfide solution (Na_2S_x) used for sulfuration.

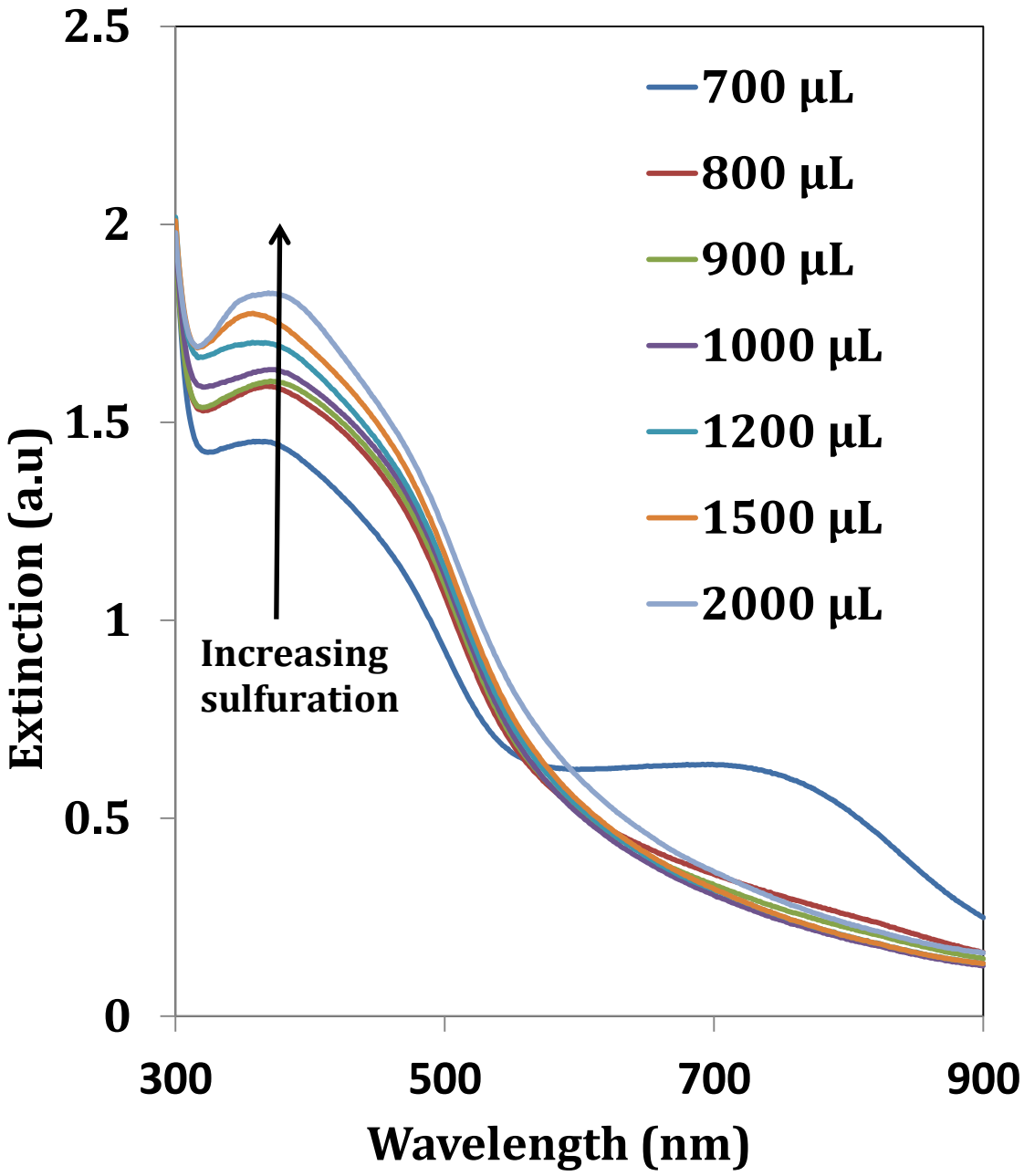

Figure 5.1.b. UV-vis extinction spectra of sulfurized cubes treated with different amounts of polysulfide solution. Figure legends show the amount (volume, µL) of polysulfide solution (Na_2S_x) used for sulfuration.

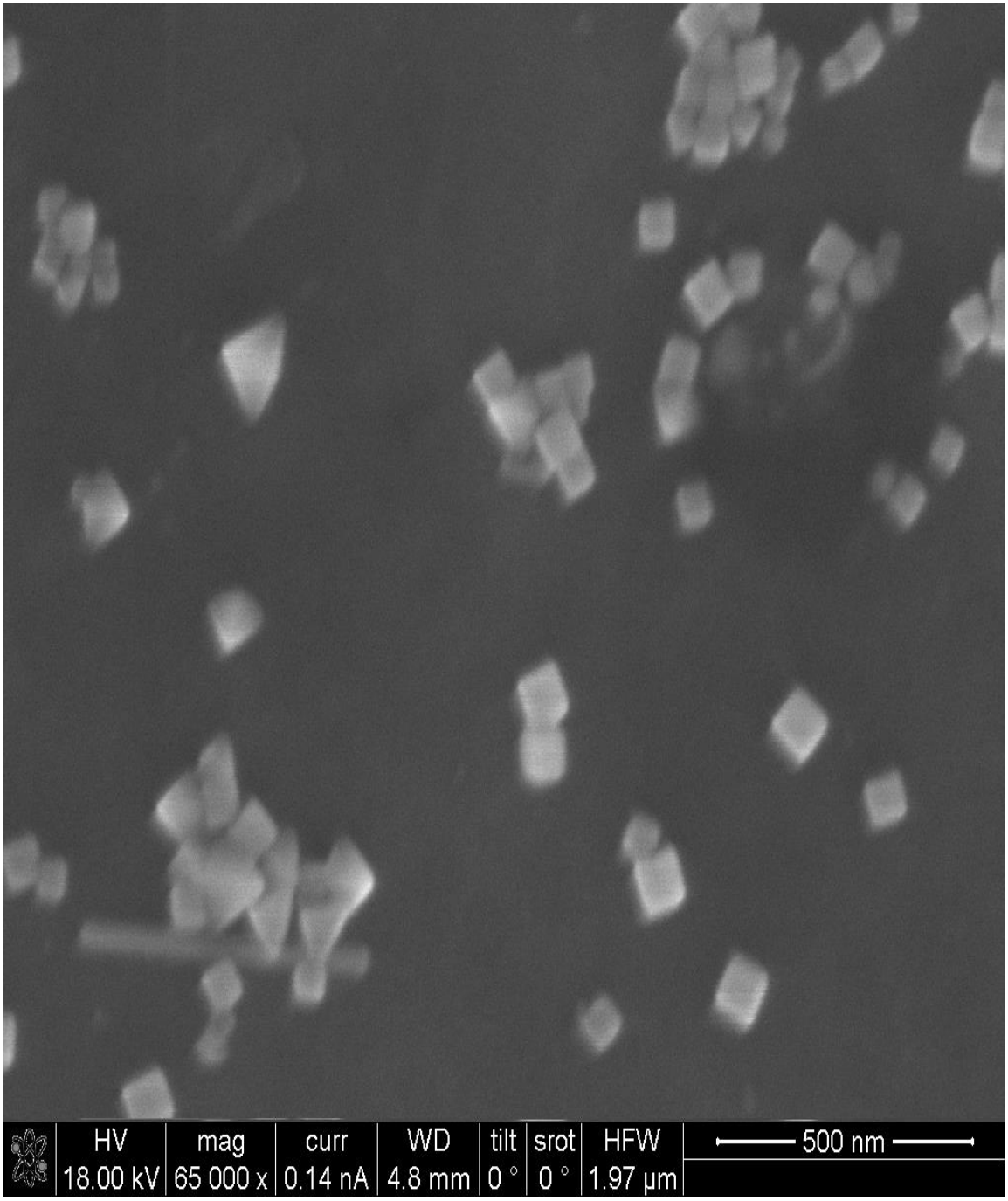

Figure 5.2. Representative SEM image of Ag cubes.

Representative SEM image of the Ag cubes is shown in Figure 5.2. The measured extinction spectrum of Ag cubes shows a major dipole SPR peak near 450 nm with higher order (quadrupole and octopole) SPR peaks at lower wavelength.[9] Figure 5.1 shows that with increasing amount of polysulfide solution, the SP peak position red shifts, and the plasmon intensity diminishes, and eventually disappears for the higher concentration of polysulfide solution with the simultaneous increase in the extinction at lower wavelength.

It has been shown from electron microscopy images and UV-vis extinction spectra that the sulfuration reaction starts at the corner sites with Ag atoms at the corner sites only being converted into Ag_2S, pushes toward the center with further sulfuration, and then the entire segments of Ag cubes are completely transformed into Ag_2S at the end of complete sulfuration reaction.[8] The decrease in plasmon intensity with increase in the extent of sulfuration is due to the expected decrease in size of Ag domain in the cube during the sulfuration. The shift in the SPR peak is expected when there is a change in the dielectric properties of the local environment around the metal nanoparticles.[17–20] The origin of the initial red shift observed for the Ag cubes treated with lower concentration of polysulfide solution (10 μL) could be due to the higher value (6.0) of dielectric constant of semiconducting Ag_2S, expected to form at the sharp corners, compared to the dielectric constant of the medium (water, 1.33).[21] The observed continuous red shift with further sulfuration is due to the increase in the thickness of Ag_2S shell around the Ag domain in the cube. As the sulfuration continue further with higher concentration of polysulfide solution (2000 μL), Ag nanocubes completely sulfurize

into Ag_2S that results in the eventual disappearance of SPR peak in the extinction spectrum with simultaneous appearance of feature (i.e., increase in the absorption at lower wavelength) corresponding to the band gap of Ag_2S semiconductor.

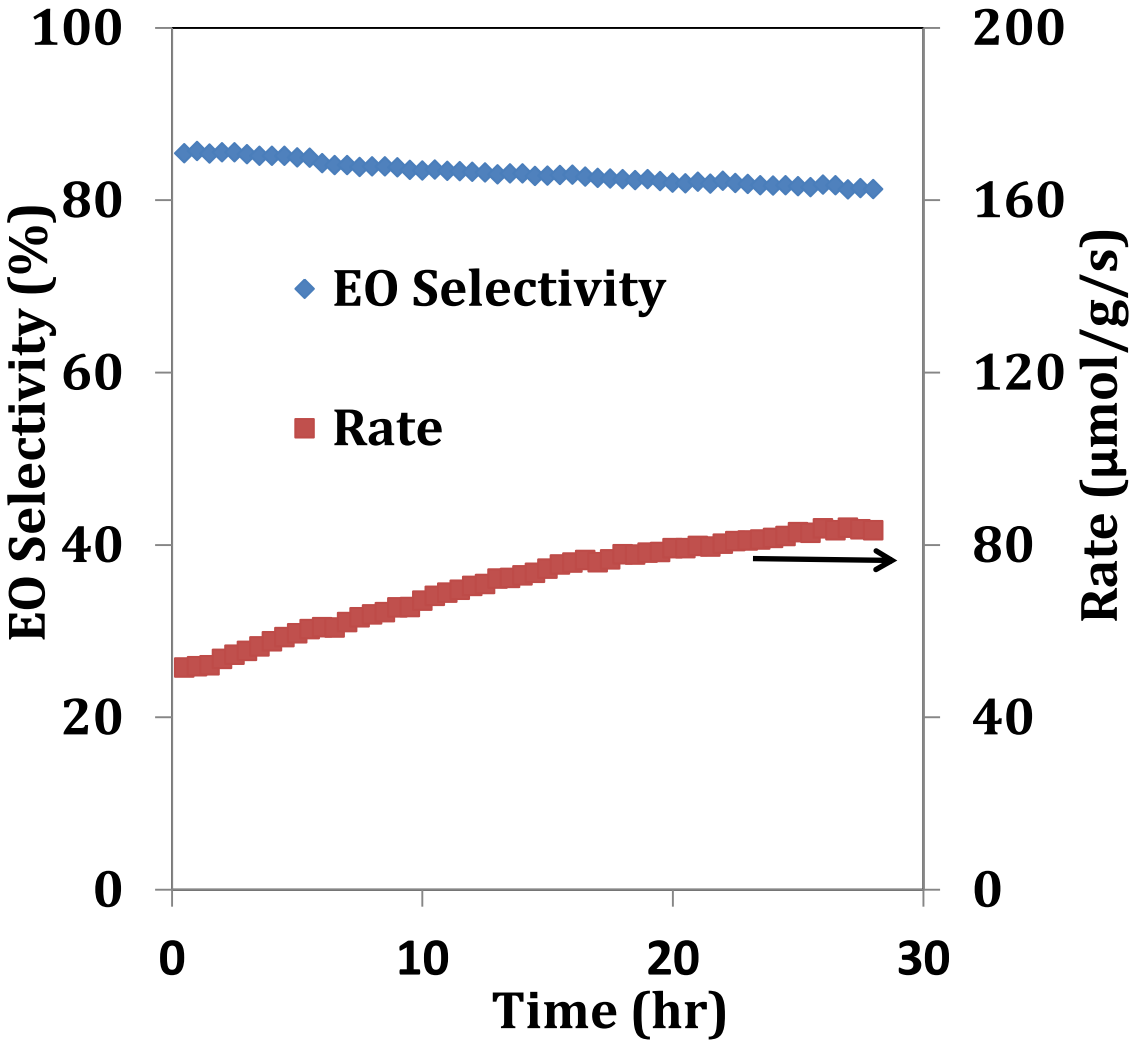

Figure 5.3.a. Selectivity to EO (left axis, blue diamonds) and rate of ethylene oxidation (right axis, red squares) observed from α-Al_2O_3 supported Ag cubes at 220^0C as a function of reaction time.

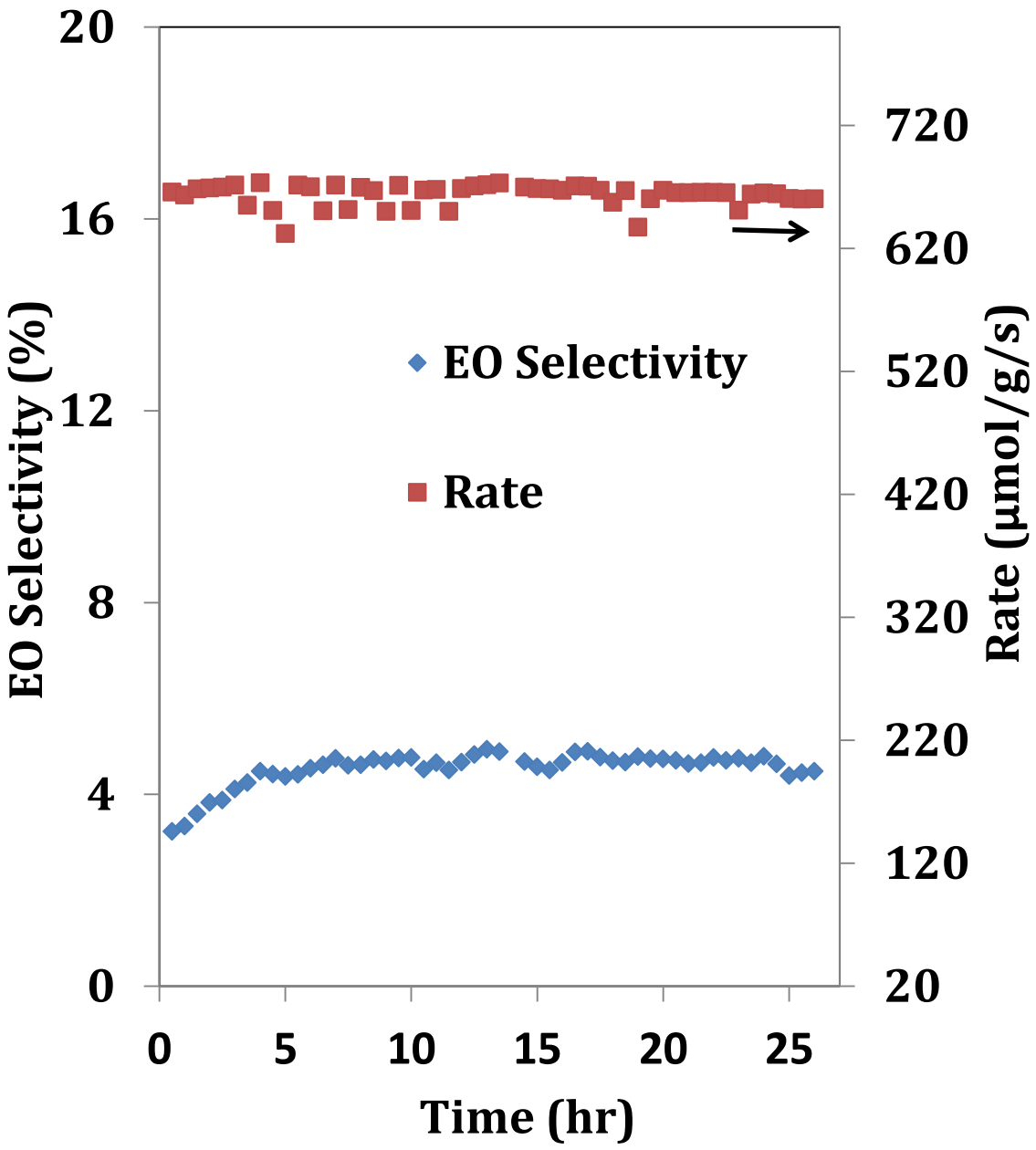

Figure 5.3.b. Selectivity to EO (left axis, blue diamonds) and rate of ethylene oxidation (right axis, red squares) observed from α-Al_2O_3 supported sulfurized Ag cubes treated with high concentration (2000 µL) of polysulfide solution at 220^0C as a function of reaction time.

To investigate the impact of sulfuration on EO selectivity and the stability of the catalyst, we first carried out the ethylene oxidation reactions over the catalysts prepared from a) Ag cubes, and b) sulfurized Ag cubes treated with high concentration (2000 μL) of polysulfide solution. Figures 5.3.a and 5.3.b show the rate of reaction and EO selectivity as function of reaction time observed at 220^0C from catalysts containing Ag cubes and sulfurized Ag cubes, respectively. The data from this batch of Ag cube catalysts show that EO selectivity- measured as the rate of generation of EO divided by the rate of generation of all products- is ~85% with the balance consisting of CO_2. This Ag cube catalysts show a drop in EO selectivity of ~3% during the reaction time of 29 hours. The data also show that the reaction rate, measured as the rate of ethylene consumption, increases slowly with reaction time. This combined trend of decrease in EO selectivity and increase in reaction rate with reaction time indicates that the Ag cubes in this catalyst undergo change in the morphology towards thermodynamically stable quasi-spherical shape. The same batch of silver cubes treated with high concentration (2000 μL) of polysulfide solution showed poor EO selectivity of ~5% as can be seen from Figure 5.3.b. It is important to note that these sulfurized Ag cubes showed ~8 times higher reaction rate with stable activity (i.e., relatively better stability) compared to pure Ag cube catalysts. It can be seen from the UV-vis extinction spectrum in Figure 5.1 that Ag cubes treated with 2000 μL of polysulfide solution are basically Ag_2S particles. A priori, we expected that Ag_2S would be inactive for the ethylene oxidation reaction and hypothesized that selective sulfuration of unselective Ag atoms at the corner sites into Ag_2S would result in higher EO selectivity with lower overall reaction rate.

Unexpectedly, the Ag_2S particles showed higher reaction rate with poor EO selectivity. In other words, Ag_2S showed high activity and mainly catalyzed the combustion of ethylene into undesired products, CO_2 and H_2O, during the ethylene oxidation reaction.

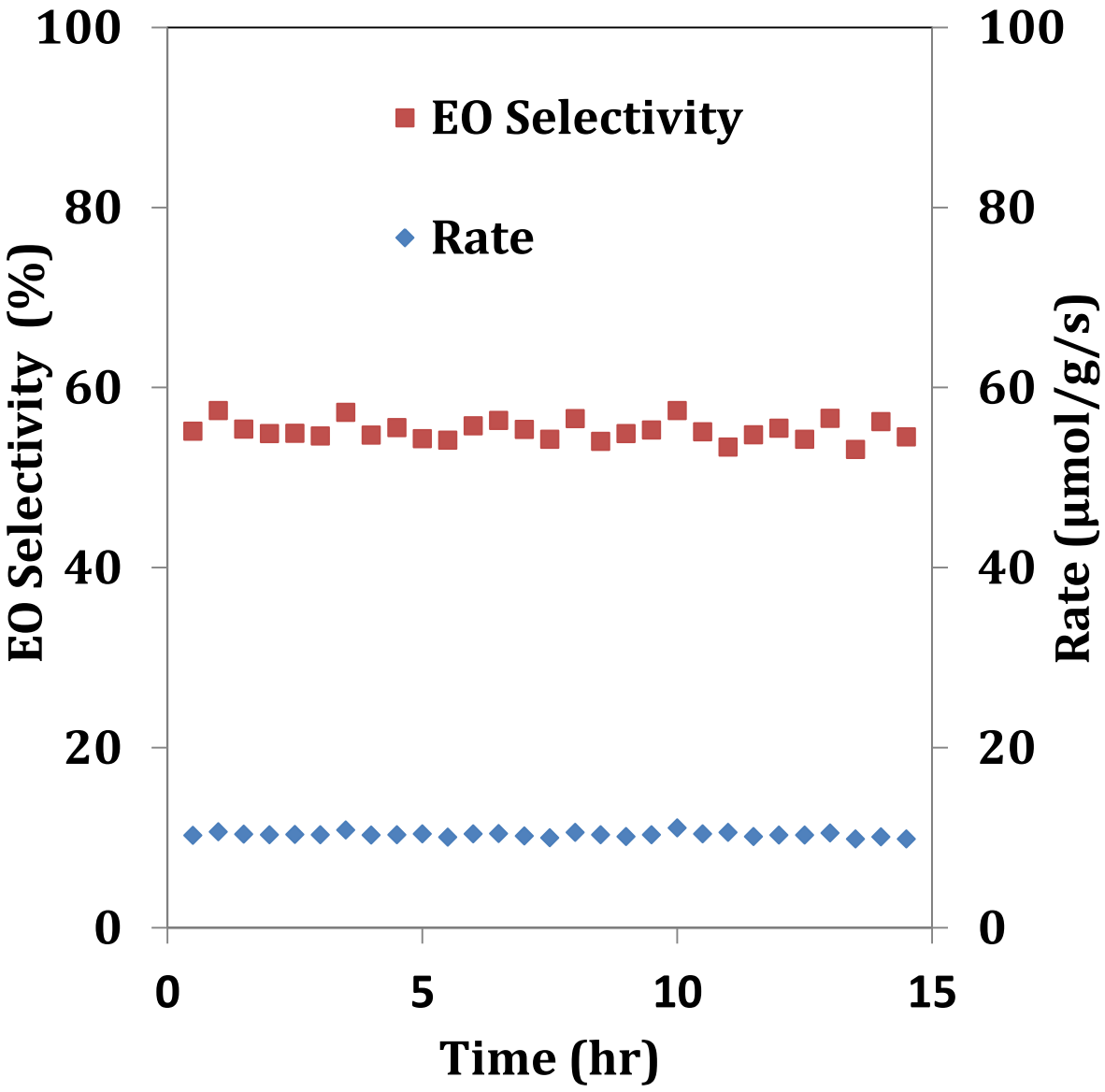

Figure 5.4.a. Selectivity to EO (left axis, red squares) and rate of ethylene oxidation (right axis, blue diamonds) observed from α-Al_2O_3 supported Ag cubes at 230^0C as a function of reaction time.

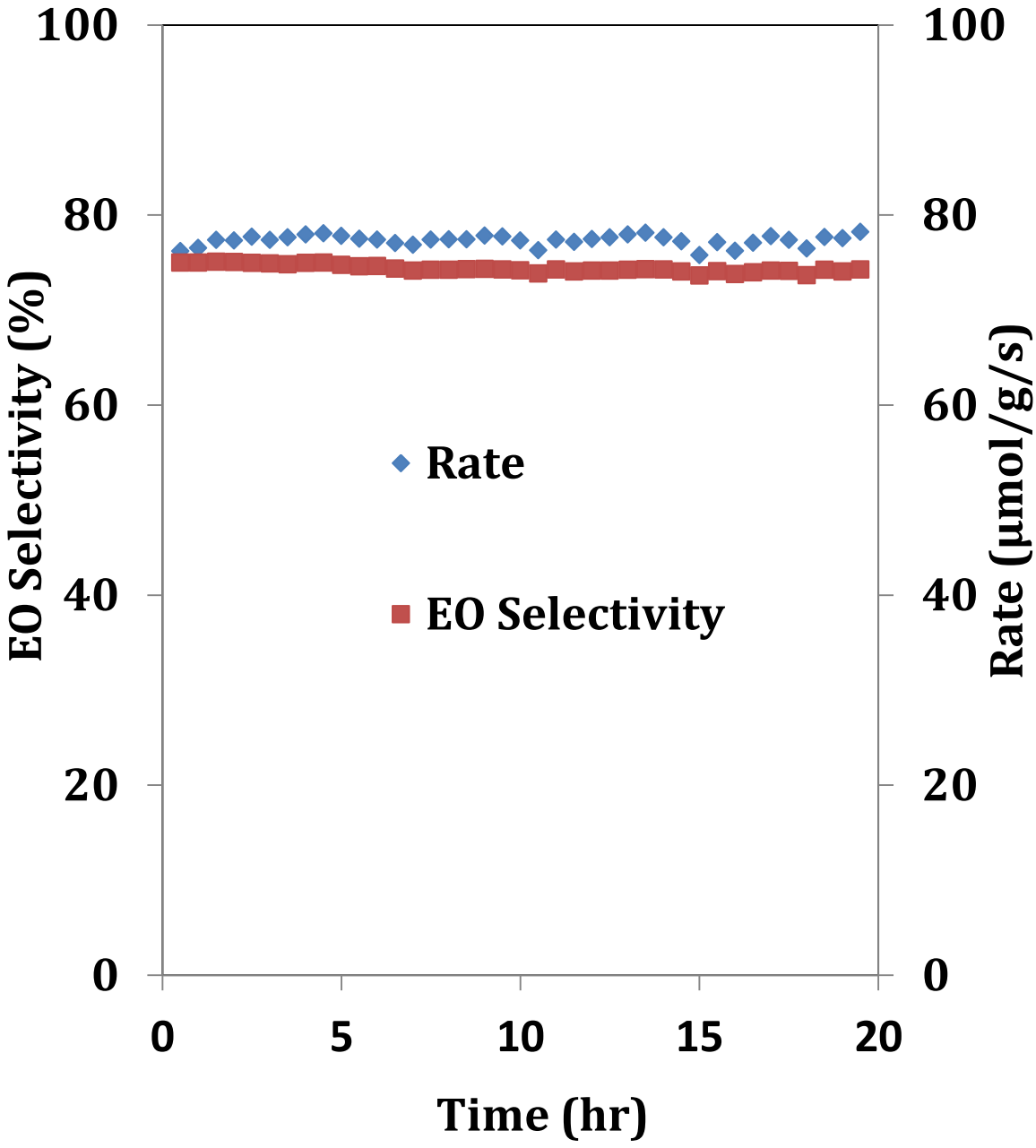

Figure 5.4.b. Selectivity to EO (left axis, red squares) and rate of ethylene oxidation (right axis, blue diamonds) observed from α-Al_2O_3 supported sulfurized Ag cubes treated with low concentration (10 µL) of polysulfide solution at 230^{0}C as a function of reaction time.

To investigate the impact of selective sulfuration of Ag cubes with low concentration of polysulfide solution on EO selectivity and the stability of the catalyst, we carried out the ethylene oxidation reactions over another set of catalysts containing a) Ag cubes, and b) sulfurized Ag cubes treated with 10 μL of polysulfide solution. In Figures 5.4.a and 5.4.b, we show the rate of reaction and EO selectivity as a function of reaction time observed at 230^0C from the catalysts containing Ag cubes and sulfurized Ag cubes, respectively. The data from this batch of Ag cube catalysts showed EO selectivity of ~57% with stable reaction rate during the reaction time of 14 hours. Intriguingly, sulfurized Ag cube catalysts treated with low concentration of polysulfide solution showed ~15% higher EO selectivity (a total of ~72% EO selectivity) and ~6 times higher reaction rate compared to pure Ag cubes catalyst. If one considers the selective sulfuration of corner Ag sites into Ag_2S, these Ag_2S sites should cause a lower EO selectivity with higher overall reaction rate, as observed with the sulfurized catalyst in Figure 5.3.b. On the other hand if one expects Ag_2S formed at the corner sites to be inactive for ethylene oxidation reaction, the catalyst should cause high EO selectivity with lower reaction rate, as we originally hypothesized. Instead, the catalyst containing Ag cubes treated with low concentration (10 μL) of polysulfide solution showed higher EO selectivity as well as higher reaction rate compared to Ag cube catalysts. As can be seen from Figure 5.4.b, this sulfurized Ag cube catalysts also showed stable reaction rate and EO selectivity during the reaction time of 19 hours.

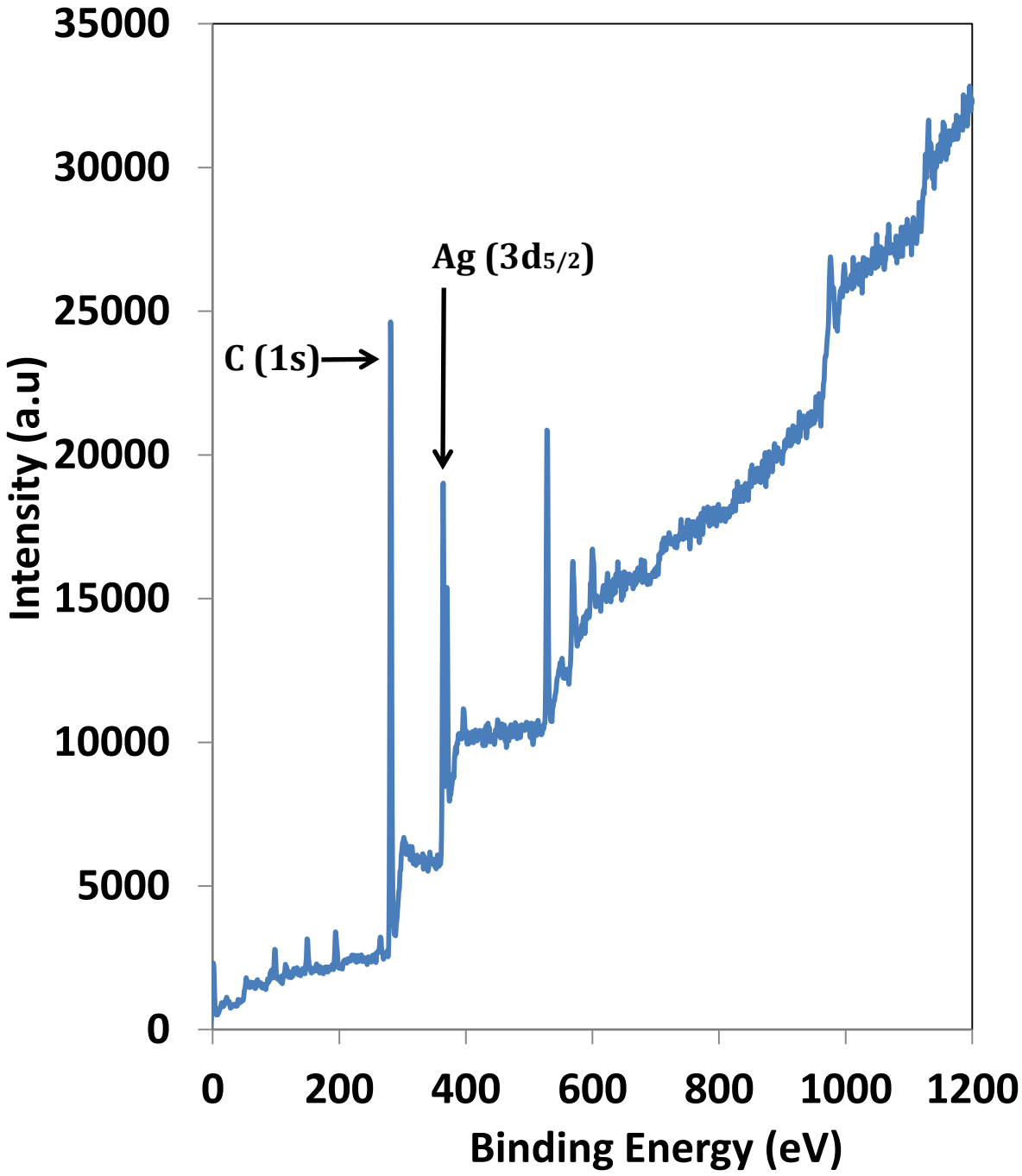

Figure 5.5.a. X-ray photoelectron spectrum of Ag cubes.

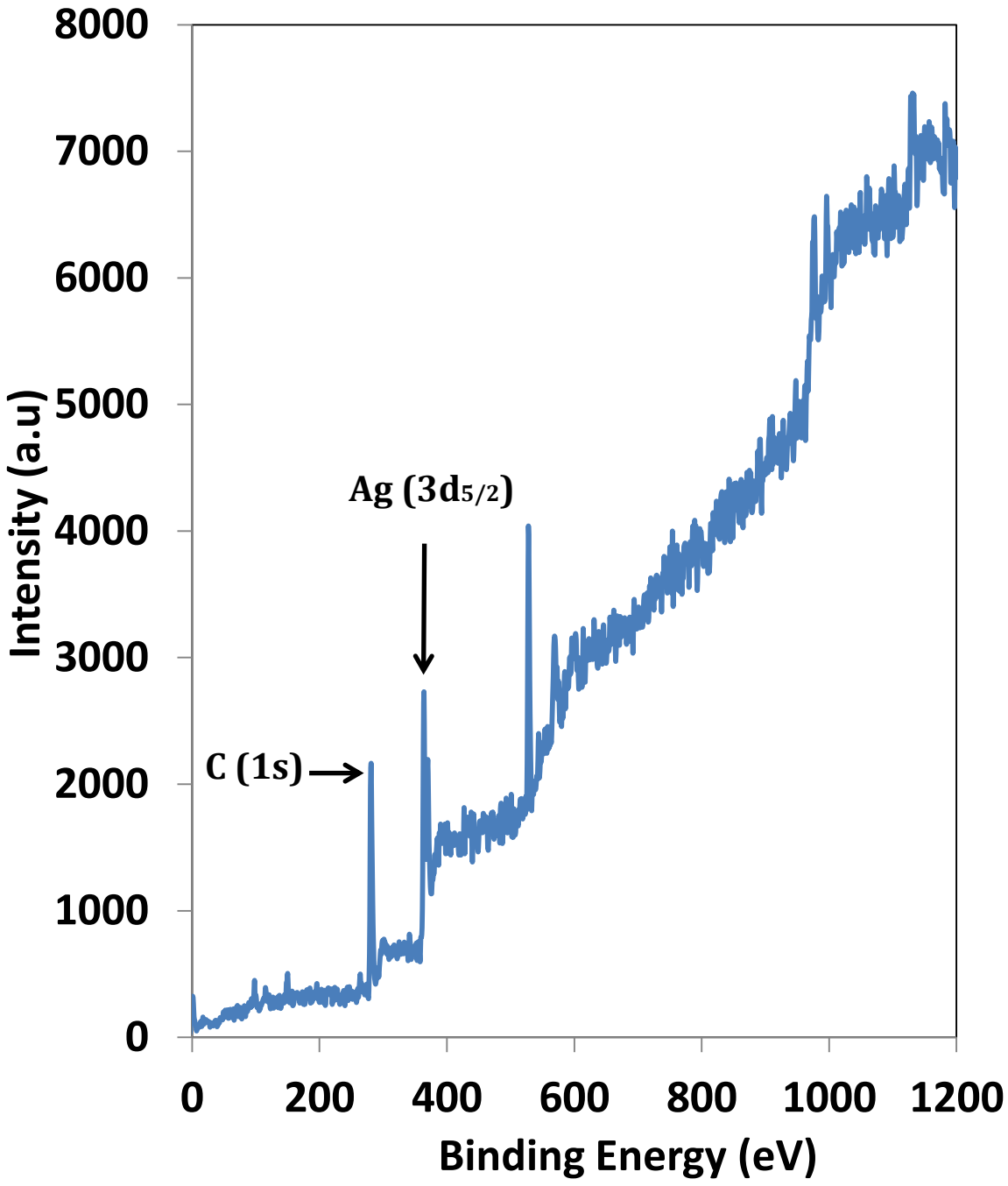

Figure 5.5.b. X-ray photoelectron spectrum of sulfurized Ag cubes treated with low concentration (10 µL) of polysulfide solution.

To explore the origin of difference in activity and EO selectivity observed from the above mentioned α-Al_2O_3 supported Ag catalysts containing Ag cubes and sulfurized Ag cubes treated with low concentration of polysulfide solution, we characterized Ag cubes and sulfurized Ag cubes with X-ray photoelectron spectroscopy (XPS). In Figures 5.5.a and 5.5.b, we show the XPS spectra of Ag cubes and sulfurized Ag cubes treated with 10 μL of polysulfide solution deposited on glass wafers, respectively. It can be seen from Figure 5.5.b that there is no sulfur signal observed at 164.05 eV (i.e., sulfur 2p peak)[22] from the XPS spectra of these sulfurized Ag cubes. This observation indicates that the fraction of Ag sites sulfurized into Ag_2S in Ag cubes treated with 10 μL of polysulfide solution might be too small to be detected in XPS for the acquisition conditions used in our measurement. Figures 5.5.a and 5.5.b also show that the ratio of carbon (284.6 eV, 1s)[22] to silver (367.9 eV, 3d5/2)[22] signal is lower in sulfurized Ag cubes compared to Ag cubes. The major source of carbon impurity observed from these samples is the polymeric capping agent, polyvinylpyrrolidone (PVP), used during the synthesis of Ag cubes. The Ag cubes and sulfurized Ag cubes used for the measurement of XPS spectra were washed to remove PVP by centrifugation with water and acetone for equal number of times. Given the similar procedures followed to remove PVP, the relatively less carbon signal observed from sulfurized Ag cubes indicates that, during sulfuration process, the polysulfide solution assists in the chemical removal of the remaining PVP from the surface. This additional PVP removal results in lesser PVP covered on the surface of sulfurized Ag cubes compared to Ag cubes.

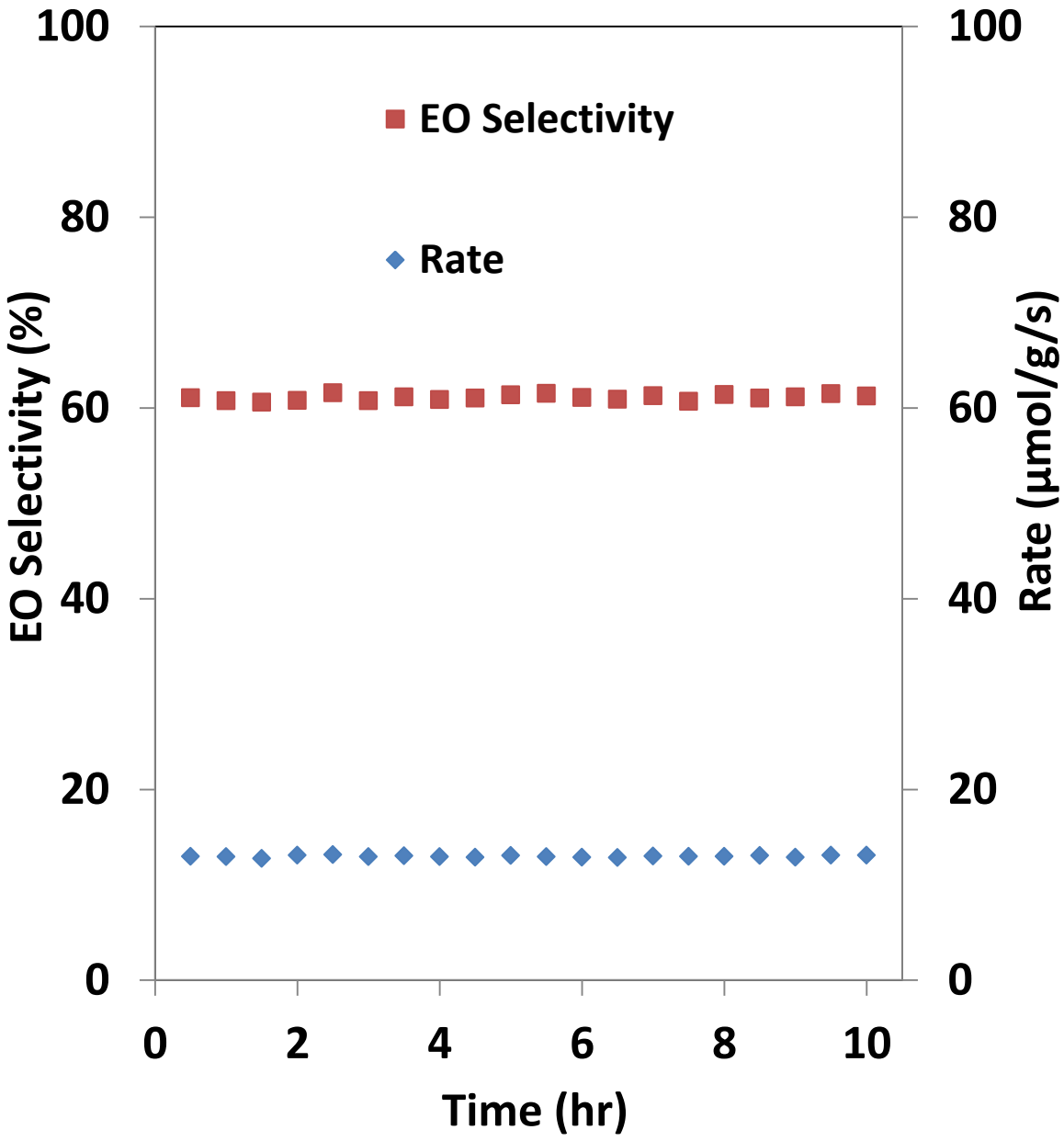

Figure 5.6.a. Selectivity to EO (left axis, red squares) and rate of ethylene oxidation (right axis, blue diamonds) observed from α-Al_2O_3 supported Ag cubes at 230^{0}C as a function of reaction time after pretreatment at 270^{0}C in 25% oxygen (remaining nitrogen).

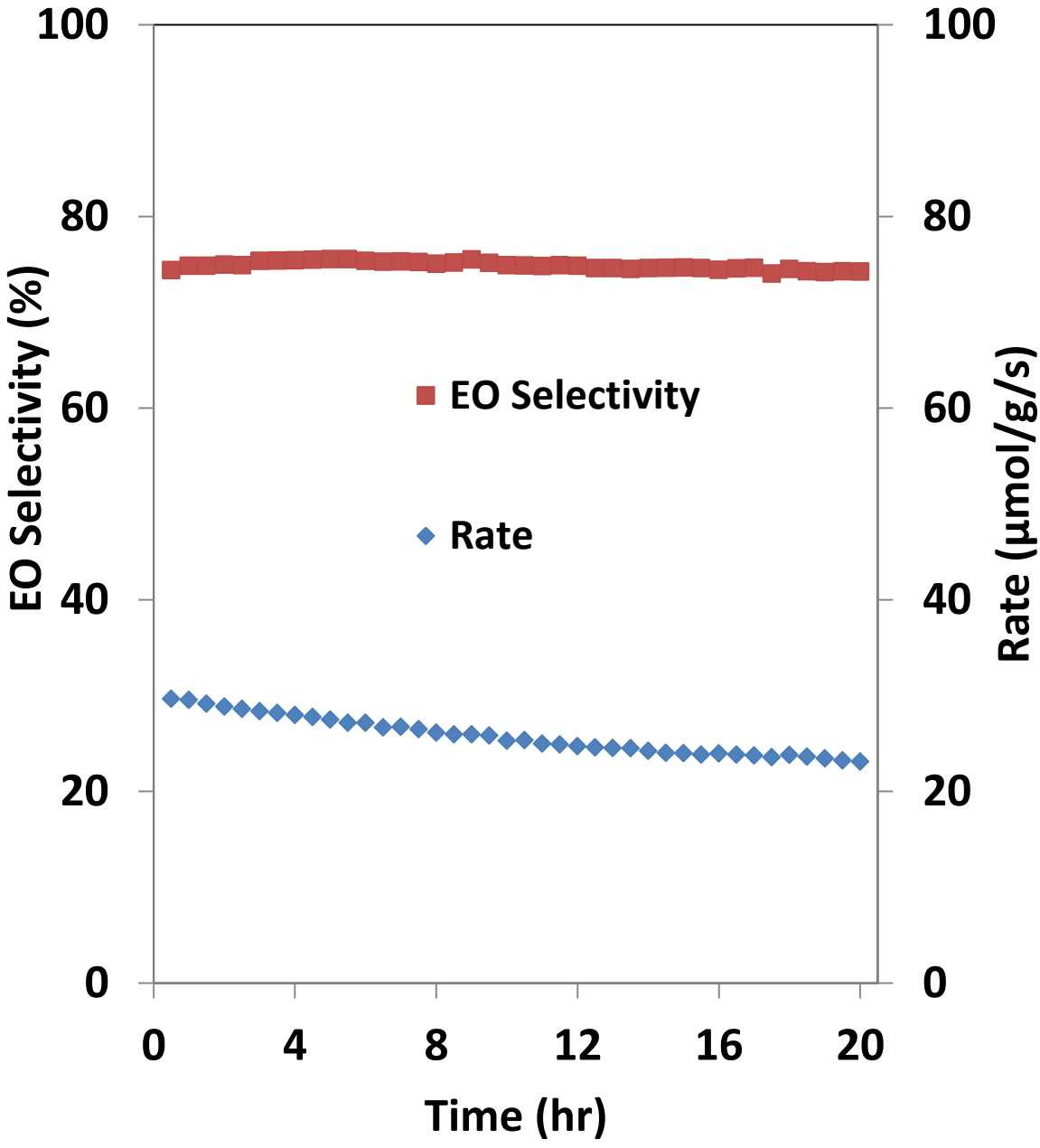

Figure 5.6.b. Selectivity to EO (left axis, red squares) and rate of ethylene oxidation (right axis, blue diamonds) observed from α-Al_2O_3 supported Ag cubes at 230^{0}C as a function of reaction time after exposure to 400^{0}C in 25% oxygen (remaining nitrogen).

As mentioned in the experimental methods section and in the above paragraph, we followed similar washing and pretreatment procedures to remove PVP from the surface of Ag cubes and sulfurized Ag cubes before the ethylene oxidation reaction. To test whether the higher surface sites exposure resulted from the additional PVP removal by the polysulfide solution might be responsible for the higher reaction rate and higher EO selectivity observed with sulfurized Ag cubes, we carried out the ethylene oxidation reaction over another batch of Ag cubes catalyst by following different pretreatment conditions to remove PVP. For this study, firstly, we pretreated the Ag cubes catalyst as usual at 270^0C for 5 hours in 25% oxygen (remaining nitrogen) to remove PVP before starting the ethylene oxidation reaction. In Figure 5.6.a, we show the rate of reaction and EO selectivity as a function of reaction time observed at 230^0C from this Ag cube catalysts. It can be seen from the figure that the catalyst shows EO selectivity of ~60% with stable reaction rate during the reaction time of 10 hours. After this 10 hours of ethylene oxidation reaction, the reaction was stopped, the catalyst was exposed to higher temperature (400 ^{0}C) in 25% oxygen (remaining nitrogen) for 1 hour to remove any remaining PVP, then cooled back to 230^0C, and the ethylene oxidation reaction was again continued at the same temperature (230^0C). Figure 5.6.b shows the rate of reaction and EO selectivity as function of reaction time observed from the same Ag cube catalysts after exposure to 400^0C. The data show that the catalyst after exposure to 400^0C exhibit ~13% higher EO selectivity (a total of ~73% EO selectivity) and ~2.5 times higher reaction rate compared to the same catalyst pretreated only at 270^0C. These changes in the reaction rate and EO selectivity upon exposure of the catalyst

to higher temperature (400^0C) in oxygen atmosphere indicate that the changes are most likely the result of additional PVP removal from the surface of Ag cubes and the subsequent exposure of more clean surface Ag sites. This trend of higher reaction rate with higher EO selectivity observed upon removal of additional PVP from the surface of Ag cubes also indicates that the higher reaction rate and EO selectivity observed with Ag cubes treated with low concentration (10 μL) of polysulfide solution compared to Ag cubes pretreated only at 270^0C (see Figures 5.4.a and 5.4.b) could be mainly due the removal of additional PVP by the polysulfide solution during sulfuration.

It is important to mention here that the Ag cube catalysts exposed to higher temperature (400^0C) to remove PVP show decrease in activity with time during the subsequent ethylene oxidation reaction at 230^0C as can be seen from Figure 5.6.b, and exhibit ~20% loss in activity during the reaction time of 20 hours with not much change in the EO selectivity. These results indicate that the decrease in catalytic activity is most likely a result of sintering of catalyst particles due to their prior exposure to very high temperature (400^0C). However, the Ag cube catalysts sulfurized with low concentration polysulfide solution (10μL), in which the polysulfide solution assisted the removal of PVP chemically at room temperature, exhibit relatively stable activity (see Figure 5.4.b).

5.5. Conclusions

We showed that high EO selectivity with relatively stable catalytic activity can be achieved from Ag cubes by treating them with low concentration of polysulfide

(Na_2S_x) solution. We demonstrated that the high EO selectivity and stable catalytic activity observed from this catalyst is mainly due to the removal of capping agent (PVP) chemically by the polysulfide solution from the surface of Ag cubes during sulfuration at room temperature. It is important to mention here that the metal nanostructures of controlled shapes are generally synthesized in solution by adding a polymeric capping agent, typically PVP, which directs the growth of metal seed particles into nanoparticles of a particular shape.[9–11] After the nanoparticles of targeted shape are formed, PVP is removed from the surface of these nanoparticles usually by washing with solvents such as acetone and water. The remaining PVP from the surface of nanoparticles are removed by exposing to high temperature in oxygen atmosphere. As a consequence of their exposure to high temperature, these well-defined metal nanostructures may lose their originally designed catalytic properties due to sintering or change in morphology. The method demonstrated in this chapter could be used to remove PVP chemically at room temperature using low concentration of polysulfide solution and thereby preserve the originally designed catalytic properties of nanoparticles of controlled shapes.

5.6. References

(1) Weissermel, K.; Arpe, H.-J. Industrial organic chemistry; VCH, 1993.

(2) Horváth, I. T. Encyclopedia of catalysis; Wiley-Interscience, 2003.

(3) Handbook of Heterogeneous Catalysis, 8 Volumes; Ertl, G.; Knözinger, H.; Schüth, F.; Weitkamp, J., Eds.; 2nd ed.; Wiley-VCH, 2008.

(4) Model Systems in Catalysis: Single Crystals to Supported Enzyme Mimics; Rioux, R., Ed.; 1st ed.; Springer, 2009.

(5) Christopher, P.; Linic, S. Engineering Selectivity in Heterogeneous Catalysis: Ag Nanowires as Selective Ethylene Epoxidation Catalysts. J. Am. Chem. Soc. 2008, 130,

11264–11265.

(6) Christopher, P.; Linic, S. Shape- and Size-Specific Chemistry of Ag Nanostructures in Catalytic Ethylene Epoxidation. ChemCatChem 2010, 2, 78–83.

(7) Linic, S.; Christopher, P. Overcoming Limitation in the Design of Selective Solid Catalysts by Manipulating Shape and Size of Catalytic Particles: Epoxidation Reactions on Silver. ChemCatChem 2010, 2, 1061–1063.

(8) Zeng, J.; Tao, J.; Su, D.; Zhu, Y.; Qin, D.; Xia, Y. Selective Sulfuration at the Corner Sites of a Silver Nanocrystal and Its Use in Stabilization of the Shape. Nano Lett. 2011, 11, 3010–3015.

(9) Lu, X.; Rycenga, M.; Skrabalak, S. E.; Wiley, B.; Xia, Y. Chemical Synthesis of Novel Plasmonic Nanoparticles. Annual Review of Physical Chemistry 2009, 60, 167–192.

(10) Sun, Y.; Xia, Y. Shape-Controlled Synthesis of Gold and Silver Nanoparticles. Science 2002, 298, 2176–2179.

(11) Xia, Y.; Xiong, Y.; Lim, B.; Skrabalak, S. E. Shape-Controlled Synthesis of Metal Nanocrystals: Simple Chemistry Meets Complex Physics? Angewandte Chemie International Edition 2009, 48, 60–103.

(12) Ingram, D. B.; Linic, S. Water Splitting on Composite Plasmonic-Metal/Semiconductor Photoelectrodes: Evidence for Selective Plasmon-Induced Formation of Charge Carriers near the Semiconductor Surface. J. Am. Chem. Soc. 2011, 133, 5202–5205.

(13) Liu, B.; Ma, Z. Synthesis of Ag_2S-Ag Nanoprisms and Their Use as DNA Hybridization Probes. Small 2011, 7, 1587–1592.

(14) Oei, D.-G. Sodium-sulfur system. II. Polysulfides of sodium. Inorg. Chem. 1973, 12, 438–441.

(15) Christopher, P.; Xin, H.; Linic, S. Visible-light-enhanced catalytic oxidation reactions on plasmonic silver nanostructures. Nat. Chem. 2011, 3, 467–472.

(16) Christopher, P.; Xin, H.; Marimuthu, A.; Linic, S. Singular characteristics and unique chemical bond activation mechanisms of photocatalytic reactions on plasmonic nanostructures. Nat Mater 2012, 11, 1044–1050.

(17) Larsson, E. M.; Langhammer, C.; Zorić, I.; Kasemo, B. Nanoplasmonic Probes of Catalytic Reactions. Science 2009, 326, 1091–1094.

(18) Seo, D.; Park, G.; Song, H. Plasmonic Monitoring of Catalytic Hydrogen Generation by a Single Nanoparticle Probe. J. Am. Chem. Soc. 2012, 134, 1221–1227.

(19) Novo, C.; Funston, A. M.; Mulvaney, P. Direct observation of chemical reactions on single gold nanocrystals using surface plasmon spectroscopy. Nat. Nanotechnol. 2008, 3,

598–602.

(20) Rice, K. P.; Walker, E. J.; Stoykovich, M. P.; Saunders, A. E. Solvent-Dependent Surface Plasmon Response and Oxidation of Copper Nanocrystals. J. Phys. Chem. C 2011, 115, 1793–1799.

(21) Chang, S.; Li, Q.; Xiao, X.; Wong, K. Y.; Chen, T. Enhancement of low energy sunlight harvesting in dye-sensitized solar cells using plasmonic gold nanorods. Energy & Environmental Science 2012, 5, 9444.

(22) Wagner, C. D. Handbook of x-ray photoelectron spectroscopy: a reference book of standard data for use in x-ray photoelectron spectroscopy; Physical Electronics Division, Perkin-Elmer Corp., 1979.

CHAPTER 6

General conclusions and future outlook

6.1. General Conclusions

In this thesis, we have demonstrated that the surface plasmon mediated electromagnetic near field effect can be utilized to achieve selective amplification of the scattered light signal from the targeted vibrational bands in a molecule by controlling the shape of the plasmonic metal nanostructures. As a possible application, the substrate that demonstrated selective vibrational band enhancement in this study could be used in selective molecular species detection from a mixture of molecular species. We have also demonstrated an approach to change the oxidation state of heterogeneous catalyst under reaction conditions and thereby change the selectivity of the catalyst to favor the formation of the desired product. The approach takes advantage of the strong interactions of plasmonic metal nanoparticle catalyst with visible light manifested in the photo-excitation of the surface plasmon resonance. We have also shown that the catalysts containing metal nanostructures of controlled shapes treated with polysulfide solution exhibit relatively stable catalytic activity and high selectivity towards the desired product. We have demonstrated that the removal of polymeric capping agent (polyvinylpyrrolidone, PVP) from the surface of metal nanostructures of controlled

shapes is critical and the PVP removal by the polysulfide solution is mainly responsible for the improved performance observed with sulfurized Ag cubes. In this chapter, we discuss possible future projects based on the conclusions drawn from this thesis.

6.2. Future outlook

6.2.1. Plasmonic metal nanostructures as platform for controlling and enhancing light-matter interactions

In chapter 3. we have demonstrated that the selective enhancement observed for the vibrational bands is due to the selective Raman scattering enhancement of the particular band by the nanoparticles. The plasmon-enhanced selective Raman scattering shown in chapter 3 gives a new insight to control and enhance photon processes using size and shape controlled synthesis of plasmonic nanoparticles. For example, the scattering events of the two vibrational bands - 2219.6 and 996.2 cm^{-1} happen at the ratio of 1.77 in Raman scattering of DPA as demonstrated in chapter 2. Using tunable silver nanoparticle substrates, we have manipulated this ratio (to 1.2 or 2.54) by selectively enhancing Raman (Stokes) scattering of particular vibrational band in surface-enhanced Raman scattering of diphenylacetylene, and the absolute signal observed for these vibrational bands over silver nanostructures in SERS are 3 to 4 orders of magnitude higher compared to the Raman signal (in the absence of silver nanostructure). Thus, herein, we demonstrate that tunable silver nanoparticle substrates, prepared through size and shape controlled synthesis, can be used to manipulate and enhance light-matter interactions through controlling

and enhancing the photon processes. The method – plasmon enhanced selective Raman scattering enhancement utilized in the current study has important consequences in other photon mediated processes.[1,2] Controlling and enhancing light-matter interactions is important in a wide range of other applications, including spectroscopic techniques,[1,2] photocatalytic reactions,[2–8] and photovoltaics.[9,10] For example, spectroscopic techniques involve identification (characterization) of substance based on light-matter interactions, i.e., absorbed, emitted or scattered light signal. Photocatalytic reactions use the light energy (example, solar radiation) for the enhanced reaction rate that is based on absorption of photons by reactant molecules and/or photocatalyst. Solar cell involves conversion of light energy into electrical energy based on the absorption of photons by photovoltaic materials. In all these applications, the performance of the devices depends on light-matter interaction. To improve (and tune if needed) the performance of these devices, controlling, manipulating and enhancing light-matter interaction are important through controlling/manipulating and enhancing the respective photon processes (absorption, emission, scattering etc.). In chapter 3, we have demonstrated how well defined-metal nanostructure can be used to control and enhance light-matter (analyte) interactions. We have shown how Raman scattered signals from different vibrational bands of a molecule can be manipulated and enhanced by controlling the size and shape of the metal nanostructure. The approach demonstrated in this study shows that plasmonic metal nanostructures can be used as platform for many applications, including chemical characterization, photocatalytic reactions, and photovoltaics.

6.2.2. Surface plasmon mediated photo-switching of oxidation states of catalyst

In chapter 4, we have demonstrated an approach to manipulate the oxidation state of plasmonic copper (Cu) nanoparticle catalysts under operating propylene epoxidation conditions. Controlling the oxidation state of functioning catalysts is critical in catalysis for the control of reactant conversion rates and product selectivity. The mechanisms discussed in chapter 4 are universal and similar principles could be used in the design of various metal nanomaterials with photo-switchable oxidation states. For example, core-shell nanoparticles containing a plasmonic core (i.e., Au, Ag, Cu) and a shell of another metal could lend themselves to similar SPR-mediated photo-switching of the oxidation states of surface atoms.

6.2.3. Core-shell, $Cu@Cu_2O$, for efficient visible light enhanced water splitting and degradation of pollutants

In photocatalysis using semiconductors such as TiO_2 and Cu_2O, the photocatalytic activity depends on the ability of the catalyst (semiconductor) to create electron–hole pairs.[3] These excited species are then used to drive chemical reactions. Recent experimental studies have demonstrated that photocatalytic activity of semiconductor nanoparticles can be enhanced when they are combined with plasmonic metal nanostructures.[3,11–14] Enhanced photo-degradations of methylene blue have been reported with composite materials composed of silver nanostructures and TiO_2 nanoparticles compared to pure TiO_2 (see Figure 6.1).[14]

These enhanced photocatalytic activities of the composite materials (Ag/TiO_2) have been attributed to the increased absorption of incident photons by TiO_2 due to the SP mediated electromagnetic near field effect of Ag nanostructure, i.e., through resonant radiative energy transfer from Ag nanostructure to TiO_2, leading to the creation of more number of electron-hole pairs in TiO_2 in presence of Ag nanostructure compared to the TiO_2-only samples.[3,13,14]

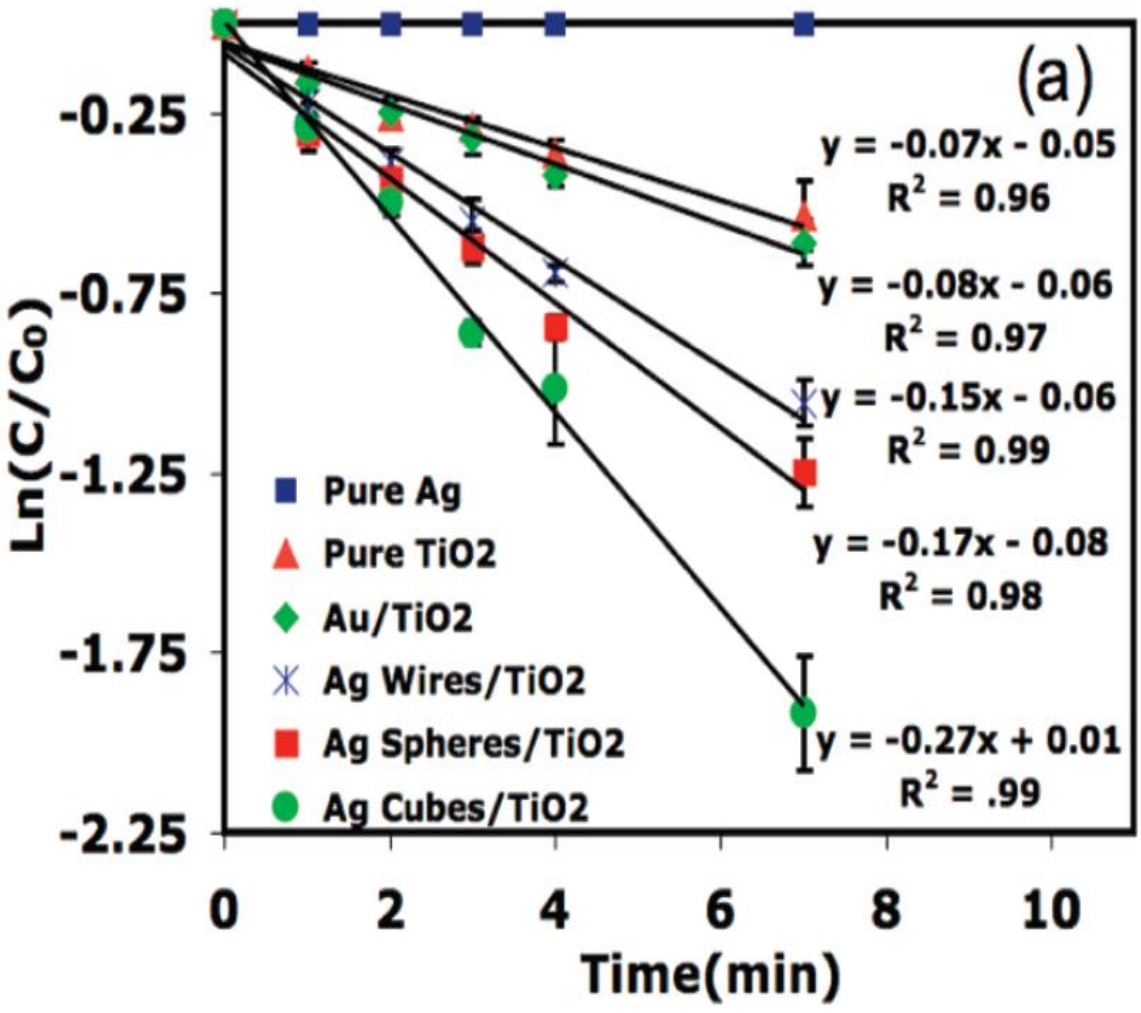

Figure 6.1. Kinetic data of the decomposition of methylene blue dye over pure Ag cubes, pure TiO_2, 15 weight % of composite of Au/TiO_2, and 15 weight % composites of Ag/TiO_2 containing Ag wires, Ag spheres and Ag cubes. Taken from Christopher et al.[14]

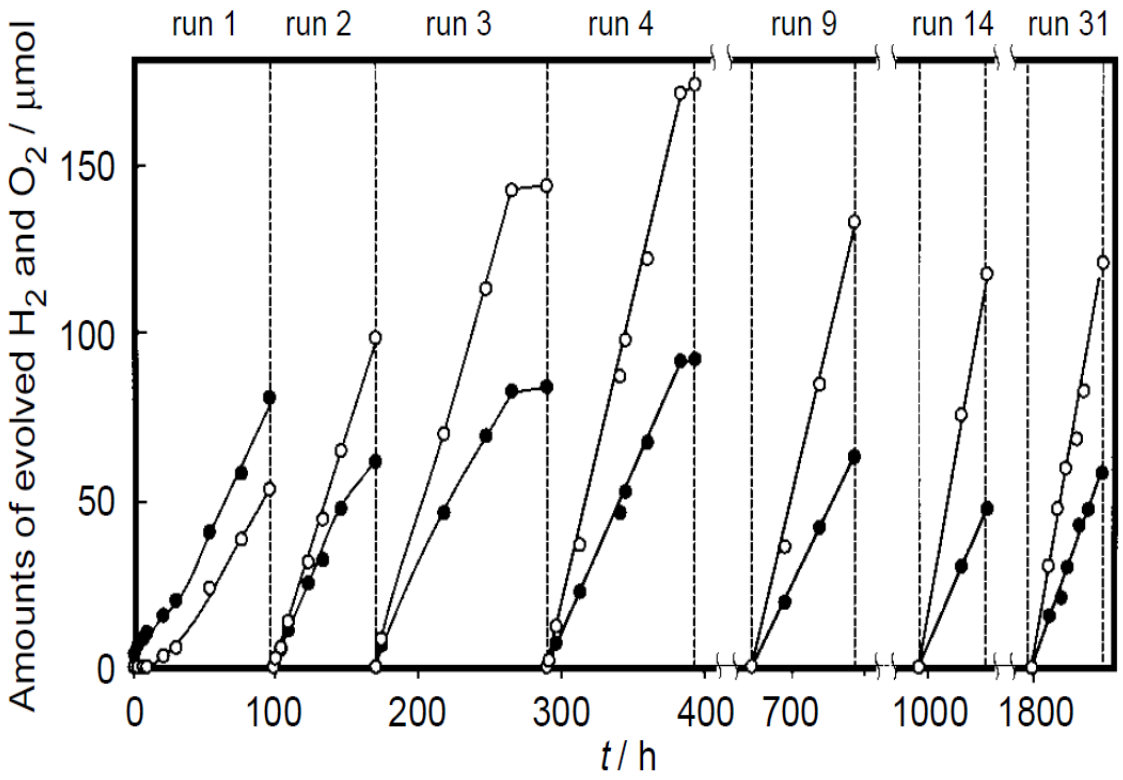

Figure 6.2. Amounts of hydrogen (H_2, open circles) and oxygen (O_2, closed circles) evolved as a function of irradiation time during visible light (wavelength≥460 nm) mediated photo-catalytic water splitting over Cu_2O catalyst. Taken from Hara et al.[15]

In chapter 4, we have demonstrated that Cu_2O shell is stable on the surface of Cu nanoparticle at low visible light intensity (<550 mW/cm^2). Cu_2O is a semiconductor with a band gap of ~ 2.0 eV.[15] It has been demonstrated that Cu_2O can act as a photocatalyst for overall water splitting under visible light irradiation (see Figure 6.2).[15] In Cu@Cu_2O, plasmonic Cu - semiconductor Cu_2O nanostructure, the radiative energy transfer from the plasmon Cu states to the Cu_2O oxide shell can enhance the rate of charge carrier (e^-/h^+) formation in Cu_2O shell, and core-shell Cu@Cu_2O nanostructure could show higher photocatalytic activity for overall water splitting and degradation of organic pollutants under low intensity visible light irradiation (<550 mW/cm^2) compared to pure Cu_2O photocatalyst. This plasmonic energy

transfer from a photo-excited plasmonic metal nanoparticle to a nearby semiconductor is well documented.[3,12–14,16,17] It can take place mainly via dipole-dipole interactions of intense SPR-mediated electromagnetic field effect around the Cu metallic core with the Cu_2O shell. In this mechanism, the metallic Cu core essentially traps light, locally amplifying its effect on the semiconductor. [3,12–14,16,17]

6.2.4. Sulfuration using polysulfide solution for the removal of capping agent from surface of metal nanostructures with controlled shapes

The metal nanostructures of controlled shapes are generally synthesized in solution by adding a polymeric capping agent, typically PVP, which directs the growth of metal seed particles into nanoparticles of a particular shape.[18–20] After the nanoparticles of targeted shapes are formed, PVP is removed from the surface of these nanoparticles usually by washing with solvents such as acetone and water. When these metal nanostructures of controlled shape are used for catalytic applications, the remaining PVP from the surface of nanostructures are removed by exposing to high temperature in oxygen atmosphere. As a consequence of their exposure to high temperature, these well-defined metal nanostructures may lose it originally designed catalytic properties due to sintering or change in morphology. The method demonstrated in chapter 5 could be used to remove PVP chemically at room temperature using low concentration of polysulfide solution and thereby preserve the originally designed catalytic properties of nanoparticles of controlled shapes.

6.3. References

(1) Ru, E. L.; Etchegoin, P. Principles of Surface-Enhanced Raman Spectroscopy: and related plasmonic effects; 1st ed.; Elsevier Science, 2008.

(2) Gray, S. K. Surface Plasmon-Enhanced Spectroscopy and Photochemistry. Plasmonics 2007, 2, 143–146.

(3) Linic, S.; Christopher, P.; Ingram, D. B. Plasmonic-metal nanostructures for efficient conversion of solar to chemical energy. Nat. Mater. 2011, 10, 911–921.

(4) Watanabe, K.; Menzel, D.; Nilius, N.; Freund, H.-J. Photochemistry on Metal Nanoparticles. Chem. Rev. 2006, 106, 4301–4320.

(5) Zhou, X.-L.; Zhu, X.-Y.; White, J. M. Photochemistry at adsorbate/metal interfaces. Surface Science Reports 1991, 13, 73–220.

(6) Al-Shamery, K. Photochemistry at nanoparticulate surfaces. Journal of Physics Condensed Matter 2006, 18, 1581.

(7) Brus, L. Noble Metal Nanocrystals: Plasmon Electron Transfer Photochemistry and Single-Molecule Raman Spectroscopy. Acc. Chem. Res. 2008, 41, 1742–1749.

(8) Zimmermann, F. M.; Ho, W. State resolved studies of photochemical dynamics at surfaces. Surface Science Reports 1995, 22, 127–247.

(9) Schuller, J. A.; Barnard, E. S.; Cai, W.; Jun, Y. C.; White, J. S.; Brongersma, M. L. Plasmonics for extreme light concentration and manipulation. Nat Mater 2010, 9, 193–204.

(10) Atwater, H. A.; Polman, A. Plasmonics for improved photovoltaic devices. Nat Mater 2010, 9, 205–213.

(11) Awazu, K.; Fujimaki, M.; Rockstuhl, C.; Tominaga, J.; Murakami, H.; Ohki, Y.; Yoshida, N.; Watanabe, T. A plasmonic photocatalyst consisting of silver nanoparticles embedded in titanium dioxide. J. Am. Chem. Soc. 2008, 130, 1676–1680.

(12) Ingram, D. B.; Linic, S. Water Splitting on Composite Plasmonic-Metal/Semiconductor Photoelectrodes: Evidence for Selective Plasmon-Induced Formation of Charge Carriers near the Semiconductor Surface. J. Am. Chem. Soc. 2011, 133, 5202–5205.

(13) Ingram, D. B.; Christopher, P.; Bauer, J. L.; Linic, S. Predictive Model for the Design of Plasmonic Metal/Semiconductor Composite Photocatalysts. ACS Catal. 2011, 1, 1441–1447.

(14) Christopher, P.; Ingram, D. B.; Linic, S. Enhancing Photochemical Activity of Semiconductor Nanoparticles with Optically Active Ag Nanostructures: Photochemistry Mediated by Ag Surface Plasmons. J. Phys. Chem. C 2010, 114,

9173–9177.

(15) Hara, M.; Kondo, T.; Komoda, M.; Ikeda, S.; Kondo, J. N.; Domen, K.; Hara, M.; Shinohara, K.; Tanaka, A. Cu_2O as a photocatalyst for overall water splitting under visible light irradiation. Chem. Commun. 1998, 357–358.

(16) Cushing, S. K.; Li, J.; Meng, F.; Senty, T. R.; Suri, S.; Zhi, M.; Li, M.; Bristow, A. D.; Wu, N. Photocatalytic Activity Enhanced by Plasmonic Resonant Energy Transfer from Metal to Semiconductor. J. Am. Chem. Soc. 2012.

(17) Awazu, K.; Fujimaki, M.; Rockstuhl, C.; Tominaga, J.; Murakami, H.; Ohki, Y.; Yoshida, N.; Watanabe, T. A Plasmonic Photocatalyst Consisting of Silver Nanoparticles Embedded in Titanium Dioxide. J. Am. Chem. Soc. 2008, 130, 1676–1680.

(18) Lu, X.; Rycenga, M.; Skrabalak, S. E.; Wiley, B.; Xia, Y. Chemical Synthesis of Novel Plasmonic Nanoparticles. Annual Review of Physical Chemistry 2009, 60, 167–192.

(19) Xia, Y.; Xiong, Y.; Lim, B.; Skrabalak, S. E. Shape-Controlled Synthesis of Metal Nanocrystals: Simple Chemistry Meets Complex Physics? Angewandte Chemie International Edition 2009, 48, 60–103.

(20) Sun, Y.; Xia, Y. Shape-Controlled Synthesis of Gold and Silver Nanoparticles. Science 2002, 298, 2176–2179.